Fall 2019

# Enhanced Sensing Performance of Novel Nanostructured ZnO Gas Sensors in Ethanol Vapor Concentration Detection Applications

Pengtao Lin
*Old Dominion University*, linpt1016@gmail.com

# ENHANCED SENSING PERFORMANCE OF NOVEL NANOSTRUCTURED ZnO GAS SENSORS IN ETHANOL VAPOR CONCENTRATION DETECTION APPLICATIONS

by

Pengtao Lin
B.S. July 2009, University of Jinan, Shandong, China
M.S. December 2013, Gannon University, Pennsylvania, USA

A Dissertation Submitted to the Faculty of
Old Dominion University in Partial Fulfillment of the
Requirements for the Degree of

DOCTOR OF PHILOSOPHY

DEPARTMENT OF ELECTRICAL AND COMPUTER ENGINEERING

OLD DOMINION UNIVERSITY
December 2019

Approved by:

Helmut Baumgart (Director)

Qiliang Li (Member)

Gon Namkoong (Member)

Christopher Bailey (Member)

## ABSTRACT

ENHANCED SENSING PERFORMANCE OF NOVEL NANOSTRUCTURED ZnO GAS SENSORS IN ETHANOL VAPOR CONCENTRATION DETECTION APPLICATIONS

Pengtao Lin
Old Dominion University, 2019
Director: Helmut Baumgart

Sensors are devices which have been commonly used to measure the functional dependence and the variability of physical parameters like temperature, pressure, pH, voltage, current, concentration, and others. Among the numerous kinds of sensors in different areas, gas sensors have been widely used and investigated for gas monitoring. Gas sensors are of crucial importance for the detection of hazardous atmospheres, because toxic gases are frequently odorless, colorless, invisible, rapidly evaporating, and flammable, and would otherwise go unnoticed. Gas sensors have been used in a variety of applications among others for the detection of specific gas species and the detection of gas concentrations.

Compared to other materials systems used in gas sensor applications, Metal Oxide Semiconductor (MOS) sensors have attracted much attention for gas detection due to their low cost, simple design and ease of production, short response time, wide detection range, and resistance to harsh working environments. Among various semiconductor materials used in MOS gas sensors, ZnO is a well-known semiconducting metal oxide material used in gas sensor applications due to its good electrical property, wide band gap of 3.37 eV, ~60 meV exciton binding energy, low cost, and high mechanical stability. ZnO has been applied for MOS gas sensor applications due to its high electrochemical stability, non-toxicity, ease of doping, and low cost. In general, gas sensors based on ZnO tend to exhibit exceptional performance for ethanol detection with respect to high sensitivity, short response time, and fast recovery time.

In this dissertation, the sensing performance of novel innovative ZnO nanostructure gas sensor designs to ethanol vapor concentration detection were investigated and analyzed in terms of their sensing response, their response time, and recovery time. Currently, the shortcomings of state-of-the-art thin film ZnO gas sensors are lack of sufficient sensitivity, long response times, and long recovery times relying only on one reactive surface. My research is addressing these shortcomings by designing, fabricating and testing novel innovative 3-dimensional nanoscale ZnO sensor device architectures with increased surface-to-volume ratio using an integrated process approach combining hydrothermal growth of nanorods with Atomic Layer Deposition (ALD) wrap-around coatings. First and foremost, Aluminum doped ZnO (AZO) thin films were introduced to enhance the sensing performance of ZnO nanorod gas sensors by providing additional oxygen vacancies and extra electrons for the redox reactions using ALD technology. A roughly 100% improvement was achieved on the sensing response of ZnO nanorod gas sensors equipped with ALD AZO 3-D wrap-around coatings compared to conventional ZnO nanorod gas sensors. Secondly, the other key approach in this dissertation was to conceive a unique novel sensor architecture design to further improve the sensing performance of ZnO nanostructure gas sensors with an innovative increase of the surface-to-volume ratio. These novel nested ZnO nanorod/nanotube gas sensors exhibited a large improvement in their sensing response due to the increased surface-to-volume ratio with two additional reaction surfaces and extra reaction sites. The sensing response of ZnO gas sensors was improved up to a maximum of 150% with the novel nested coaxial nanorod/nanotube architecture compared to the sensing response of conventional ZnO nanorod gas sensors. The third approach was to investigate the sensing performance of ZnO nanotube sensors synthesized within porous templates by utilizing ALD and $Al_2O_3$ sacrificial layers. The sensing performance of these ZnO nanotube gas sensors was enhanced with increased

surface-to-volume ratio by adding additional coaxial ZnO nanotubes. The enhancement can be further improved by adding additional coaxial ZnO nanotubes layers which provide each 2 additional reaction surfaces. Furthermore, ALD AZO coatings were introduced to further enhance the sensing performance of ZnO nanotube gas sensors synthesized in porous templates. With the combined benefits from approaches 1 and 2, the maximum gained enhancement reached up to 136% for the template replication case. The first two approaches established a bottom-up technology, which is subject to high variability from batch to batch hydrothermal growth. In contrast, nested ZnO nanotubes synthesized within porous templates enables a true top-down technology by using mask and photolithography patterning techniques from microelectronics to guarantee the reproducibility, which would render it ready for commercialization and to be transferred for industrial applications.

This dissertation is dedicated to my parents, Zhibin Lin and Yuhua Lin, and to my sister, Fanglei Lin, and to my niece, Kate Morozov, and to my nephew, Daniel Morozov.

## ACKNOWLEDGMENTS

First and foremost, I would like to express my sincere gratitude to my academic adviser, Dr. Helmut Baumgart, for his continuous support and patient guidance during my Ph.D studies and dissertation research. I am grateful for having the opportunity to be a graduate student in his research group. I appreciate his direction and help on my dissertation.

I would like to thank the members of my Ph. D committee: Dr. Gon Namkoong, Dr. Qiliang Li, and Dr. Christopher Bailey, for their suggestions and help on my research and dissertation.

I would like to thank Dr. Kai Zhang for his guidance and assistance in my Ph. D research. I am grateful for his selfless sharing of his most valuable knowledge and experiences for my research.

I would like to thank Amy Wilkerson and Olga Trofimova from College of William Mary for help with the semiconductor characterization equipment (FE-SEM).

I would like to thank Dr. Wei Cao and my graduate student colleagues, Xin Chen, Abdullah Al Mamun, and Nizam Sayeed, for their help and assistance during my research at the Applied Research Center.

I would like to express my deep gratitude to my parents and my sister for their love, support and encouragement throughout my education.

# TABLE OF CONTENTS

Page

# LIST OF TABLES

## LIST OF FIGURES

Figure Page

# CHAPTER 1

# INTRODUCTION

## 1.1 Introduction to Gas Sensors

A sensor is usually known as a converter which can measure physical signals and convert these signals into readable electronic signals by instruments. A sensor can also be considered as a device that is sensitive to the change of the physical phenomenon and convert this to an electrical or optical signal. For example, a Resistance Temperature Detector (RTD) is sensitive to the temperature as shown Figure 1. When the temperature changes, the voltage output signal of the RTD in the designed circuit will be changed correspondingly. Such resistance changes could be indicated by a multimeter and can be used for many other application purposes. The sensitivity of a sensor varies based on device design and due to the requirements of the instrumentation and application. For example, in some application areas like concentration, a sensor is required with high sensitivity for the physical quantity to be measured. For target species measurements, the sensor is only required to recognize the target species.

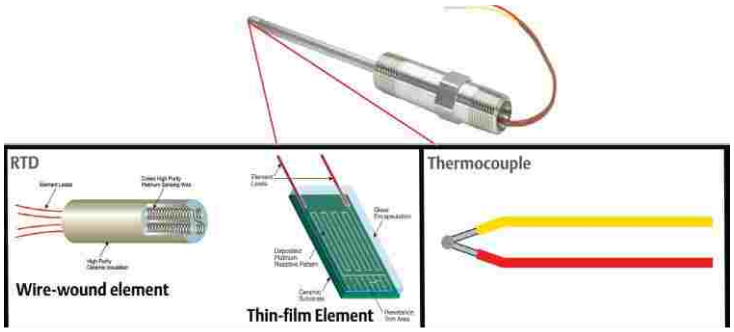


Figure 1. Schematic illustrating the working parts inside of a Resistance Temperature Detector (RTD) and the operating principle [1].

A fundamental definition of a gas sensor describes it as a device which is used to detect gas molecules, which will cause a change on the sensor, like a resistance change, and convert that change on the gas sensor into an electrical signal, which will then be corresponding to the concentration of the detected gas. Many industries and laboratories have to rely on high sensitivity gas sensors for monitoring of gas concentration or gas leaks. Therefore, as an important sensing technique, gas sensors have been investigated for gas detection, especially for hazardous gas leak monitoring. For people who work under hazardous environments, gas sensors take on a crucial role for toxic gas detection and working environment monitoring. For example, coal mines are one of the most dangerous working areas having low oxygen levels and being filled with flammable and hazardous gases [2]. The clean rooms of the microelectronics industry employ extremely toxic gases for semiconductor doping like arsine and phosphene, which need to be strictly monitored.

### 1.1.1 Applications of Gas Sensors

Many kinds of gas sensors have been developed in different areas due to the significant role of gas sensing technology. From the detection function aspect, gas sensors can be divided into two groups: 1) single gas detection (like $O_2$, methane, carbon monoxide, et al.) and 2) general vapors and odors detection and environmental monitoring [3]. Table I shows the applications of these two kinds of gas sensors.

TABLE I

Typical Applications of the two most prevalent types of gas sensors [3].

| Application Area | Applications | Gas Sensor |
|---|---|---|
| Automobile | • Car Ventilation Control<br>• Gasoline Vapor Detection<br>• Alcohol Breath Tests | Single Gas Sensor |
| Safety | • Fire Detection<br>• Leak Detection<br>• Toxic/Flammable Gas Detectors | |
| Indoor Air Quality | • Air Purifiers<br>• Ventilation Control<br>• Cooking Control | |
| Environmental Monitoring | • Weather Stations<br>• Pollution Monitoring | |
| Food | • Food Quality Control<br>• Process Control<br>• Packaging Quality Control | Volatile Organic Compounds Gas Sensor |
| Industrial Production | • Fermentation Control<br>• Process Control | |
| Medicine | • Breath Analysis<br>• Disease Detection | |

Gas sensors can be found in the detection and monitoring of vehicle exhaust gases from combustion engines manufactured by the automotive industry [4]. In the medical field, gas sensors have been applied for human olfactory system simulation [4]. The quality of indoor air has attracted a lot of attention from researchers working on healthy living projects for humans.

Therefore, gas sensors take on an important role in the indoor detection of oxygen and carbon monoxide [4]. During recent decades global warming became a serious problem and a high-profile topic for mankind and the global environment on the planet. While the underlying root causes include many complex factors, greenhouse gases and waste gases have been identified as one of the contributing factors for global warming and the study of the greenhouse gases became a top subject for global researchers. In the effort to monitor pollution and greenhouse gases in the environment, gas sensors take on a key role as detector devices for environmental studies [4].

### 1.1.2 Classification of Gas Sensor

Exposure to the target gas will typically cause a physical change in gas sensors. This physical change can then be converted into a readable signal, like an electrical signal, an optical signal, or a temperature reading. According to such a classification scheme, gas sensors can be distinguished into several different kinds based on the requirements of detection application and detecting condition as shown in Table II.

Compared to optical gas sensors, which are based on optical processes, solid state gas sensors are based on chemical reaction principles, which means the detected gas has to undergo a reversible interaction with the surface of the gas sensor [3]. Such a reaction of the gas to be detected with the sensor generally induces either a change of the electrical or thermal conductivity, or of the optical parameters, or of the mass, or of the temperature, or of the work function (like capacitance) [3]. However, each type of gas sensor has its own advantages and disadvantages, which implies different gas sensors are used with optimal effect in various very specific corresponding applications and working conditions.

TABLE II

Review of various gas sensors types and corresponding physical changes induced [3].

| # | Type of Gas Sensors | Physical Change |
|---|---|---|
| 1 | Optical Gas Sensors: Fiber Optics, Thin Films | Optical Parameters: Surface Plasmon Resonance (SPR), Reflection, Interferometry, Absorption, Fluorescence, Refractive Index |
| 2 | Field Effect Gas Sensors: Diodes, Transistors, Capacitors | Work Function (Electrical Polarization) |
| 3 | Piezoelectric Sensors: Quartz Crystal Microbalances, Surface Acoustic Wave, Microcantilevers | Mass |
| 4 | Electrochemical Gas Sensors: Potentiometric, Amperometric | Electromotive Force or Electrical Current |
| 5 | Catalytic Gas Sensors: Seebeck Effect, Pellistors, Semistors | Heat or Temperature |
| 6 | Metal Oxide Semiconductor (MOS) Gas Sensors | Electrical Conductivity |

*Optical Gas Sensors (Infrared Gas Sensors)*

Infrared gas sensors are based on the principle of energy changes after infrared light passes through a specific gas in transmission [5]. Different gases cause different characteristic absorptions of infrared radiation at corresponding wavelengths. Gases that can be detected by infrared gas sensors include carbon dioxide, carbon monoxide, methane, and Sulphur dioxide [5]. Infrared gas sensor consists of one light source and one detector component as shown in Figure 2. The infrared

absorption of different gases occurs at characteristic corresponding wavelengths, which can be calibrated to uniquely identify specific gases. The concentrations of different gases are determined by the absorption intensity of the infrared radiation. which means the intensity of the infrared light monitored by the detector decreases as the gas concentration increases.

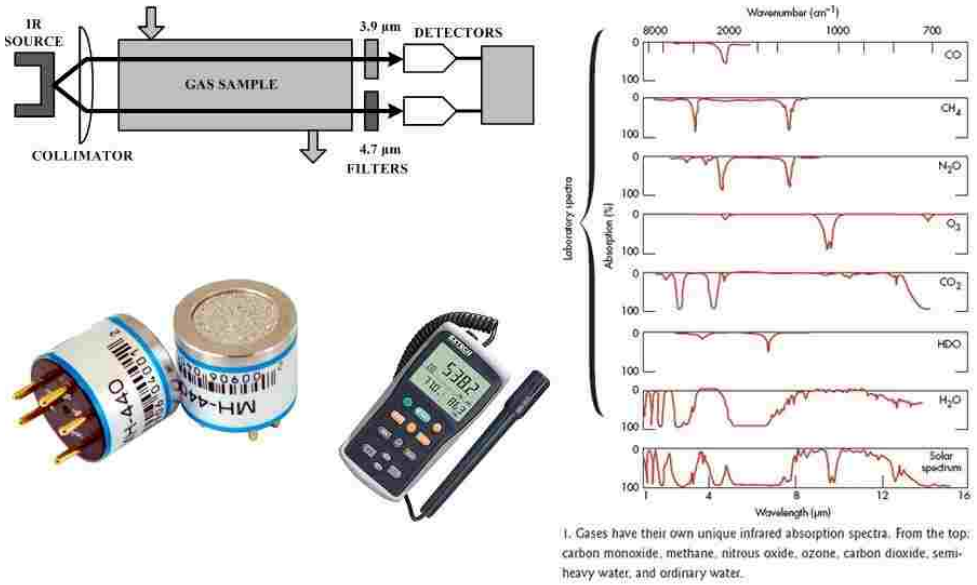


1. Gases have their own unique infrared absorption spectra. From the top: carbon monoxide, methane, nitrous oxide, ozone, carbon dioxide, semi-heavy water, and ordinary water.

Figure 2. Schematic of an Infrared Gas Sensor (left top), commercial examples (left bottom), and sensing results plots (right) [5].

The fundamental mechanism of infrared gas sensors is described by Beer's law, which forms the basis for analysis of the experimental results [5].

$$I = {I_0}/{e^{kP}} \tag{1}$$

$$P = \frac{\ln(\frac{I_0}{I})}{k} \tag{2}$$

Where $I$ is the intensity of the partially absorbed infrared light striking the detector, while $I_0$ is the measured light intensity of an empty sample chamber without target gas, $k$ is a system dependent constant, and $P$ is the concentration of the gas to be measured [5].

Based on Equation 2, the concentration of the target gas is inversely proportional to the intensity of detected infrared light.

List of advantages: Infrared Sensors a) are specific to a particular gas (suitable for gas species detection); b) possess high sensitivity and stability; c) have a long lifetime; d) are insensitive to environment change [4]; e) generally have a quick response [5].

List of disadvantages: Infrared Sensors a) require clean conditions (the result can be affected by dust and dirt on optics); b) are not suitable for multiple gas detection; c) are sensitive to humidity and water; d) incur high cost [5].

*Catalytic Gas Sensors (Thermal Conductivity Gas Sensors)*

Thermal conductivity gas sensors, which are also known as pellistors, have been used for combustible gas detection or for gases possessing thermal variation property [4, 6]. The species of the target gas can be identified by comparing the thermal conductivities of the detected gas with the reference gas (usually air) without any chemical reaction [4, 5]. Figure 3 shows the basic mechanism of a thermal conductivity gas sensors. A thermal conductivity gas sensor includes two main parts: the detector component (which is exposed to the target gas) and the reference compartment (which is sealed and filled with air or $N_2$) [5]. During detection operation, the two wire coils in these two compartments are heated to a specific temperature. The thermal conductivity is obtained from the resistance change of the wire coil compared to the reference [4]. In this way the species of the target gas can be identified unmistakably.

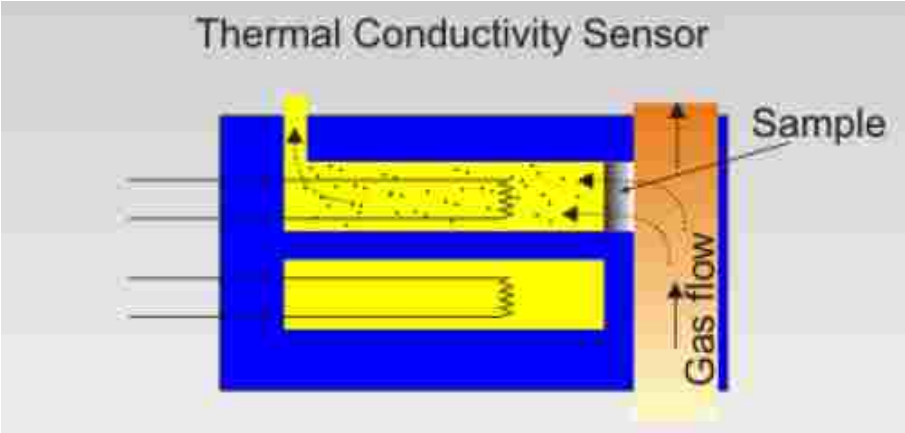


Figure 3. Schematic explaining the working principle of a thermal conductivity gas sensor [5].

Listing of advantages: thermal conductivity gas sensors possess a) high stability and reliability; b) have a long lifetime; c) are capable of high concentration detection; d) are not toxic [5].

Disadvantages: a) low accuracy; b) low sensitivity; c) narrow detection range; d) currently only used for gas leaking alarm [5].

*Electrochemical Gas Sensors*

Electrochemical gas sensors are based on the principle of a chemical reaction taking place between the gas and the material in the sensor. Following the chemical reaction an electrical signal will be produced which relates to the gas concentration [7]. Electrochemical gas sensors have been widely used in applications of oxygen and toxic gas detection (like carbon monoxide (CO), hydrogen sulfide ($H_2S$), and nitrogen dioxide ($NO_2$)) [7]. Electrochemical gas sensors typically contain two main parts: a detection electrode (sensing electrode) and a counter electrode, which are separated by a reference electrode as shown in Figure 4 [8]. The principle mechanism of the electrochemical gas sensor is based on the gas reactions (either oxidation or reduction) with the material on the surface of detection electrode. This will induce a current across the resistor attached

between the counter electrode and the detection electrode [8]. The measured current between the anode (detection electrode in Figure 4) and the cathode (counter electrode in Figure 4) is representative of the concentration of the gas flows into the electrochemical gas sensor and can be calibrated [8].

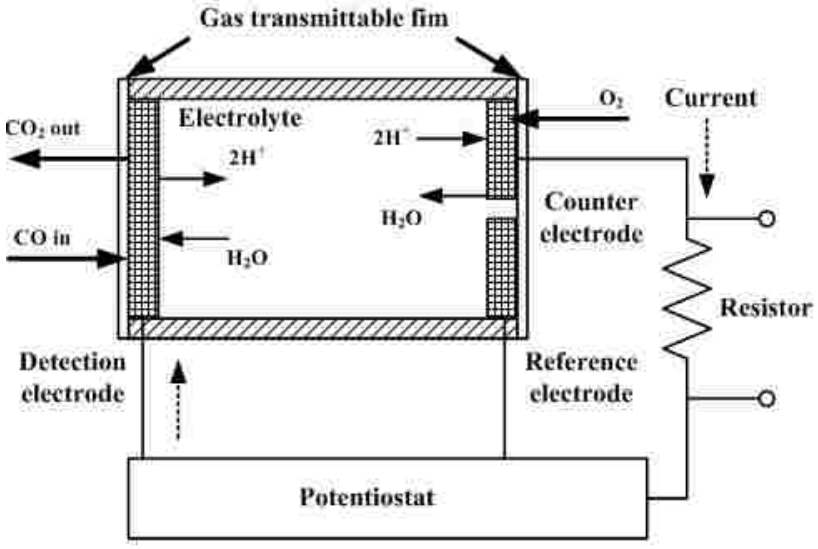


Figure 4. Schematic of the operating principle of an electrochemical gas sensor [5].

The various chemical redox reactions indicated in Figure 4 are shown in more detail below. Sensing electrode (oxidation, losing electrons):

$$CO + H_2O \rightarrow CO_2 + 2H^+ + 2e^- \quad (3)$$

Counter electrode (reduction, gaining electrons):

$$O_2 + 4H^+ + 4e^- \rightarrow 2H_2O \quad (4)$$

List of advantages: a) small size; b) low power consumption; c) numerous applications; d) high accuracy and good selectivity.

Disadvantages: a) limited lifetime; b) affected by air resulting in false alarm.

## 1.2 Introduction and Mechanism of MOS Gas Sensors

### 1.2.1 Introduction

The Metal Oxide Semiconductor (MOS) gas sensor working mechanism is based on the surface chemical reaction between a semiconducting metal oxide and the target gas. MOS gas sensors have been widely used in many gas detection applications due to their numerous advantages: resistant to aggressive harsh environment, applicable over a wide temperature range, possessing high sensitivity and stability, long life time, large detection range, rapid response, and low manufacturing cost [9]. Especially, MOS gas sensors have been applied for the detection and monitoring of harmful environmental gases, like carbon monoxide and nitrogen dioxide. Figure 5 shows numerous examples of MOS gas sensor applications for the detection of gas species and gas concentration.

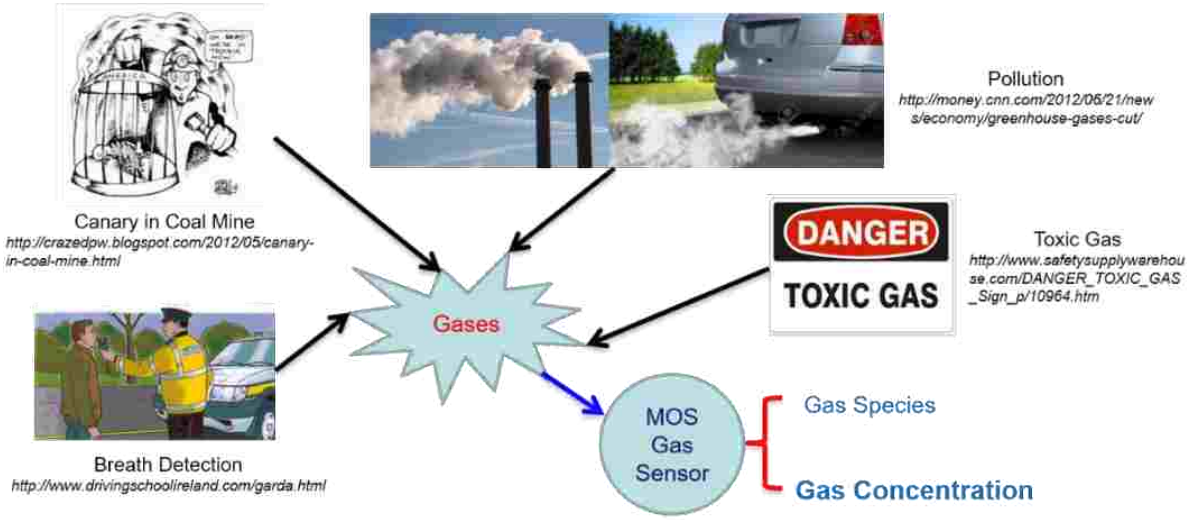


Figure 5. Examples for MOS gas sensor applications: gas species and gas concentration indication in coal mines, toxic gas detection, and pollution from industries and cars, alcohol concentration detection of driver's breath.

As indicated in Table III, MOS gas sensors have numerous unique advantages in terms of cost, lifetime, and size compared to the other competing gas sensors. Unfortunately, electrochemical gas sensors have a short lifetime, which renders them unattractive [10]. Even with high sensitivity, large selectivity, and rapid response time, optical gas sensors are still handicapped by limits on size and cost compared with MOS gas sensors [10].

TABLE III

Comparison of three gas sensing technologies [10].

| Characteristics | Electrochemical | Optical | MOS |
|---|---|---|---|
| Cost | Low | High | Low |
| Lifetime | Short | Long | Long |
| Sensitivity | High | High | High |
| Selectivity | Good | Excellent | Poor |
| Response Time | Fast | Fast | Fast |
| Size | Medium | Large | Small |

The fundamental mechanism of MOS gas sensors is the electrical resistance change (increase or decrease) after exposure to the oxidizing or reducing target gases under the corresponding optimum full-sensing-performance temperature range. The change in the resistance value of the sensor material can be readily measured. This resistance change is related to the concentration of the detected gas. MOS gas sensors are commonly designed with metal oxides deposited on heaters to enable operation at the optimum working temperature. As shown in Figure 6, there are four layers in an MOS gas sensor: substrate, heater layer, sensing electrodes, and active

sensing metal oxide film. The heating filament layer is heated by applying an electric current to enable the metal oxide layer to achieve the required optimum working temperature for the oxidation or reduction reaction with the target gases [5].

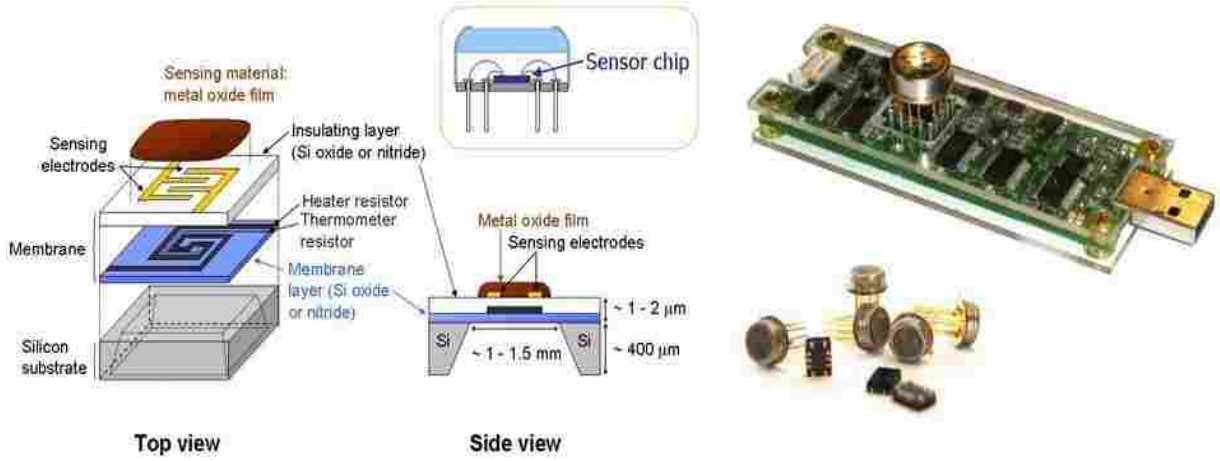


Figure 6. Schematic diagram of a typical Metal Oxide Semiconductor gas sensor device (left) and examples of commercial devices (right) [5].

*Parameters of MOS Gas Sensors*

To evaluate the gas sensor performance, there are several parameters of a gas sensor that need to be investigated [11].

1) Sensitivity: the accuracy of the changing rate of the measured signal as a function of the change of the gas concentration, which is expressed by the slope of the calibration graph of the result [12].
2) Selectivity: the response of the gas sensor to the specific gas or a group of gases [12].
3) Stability: the capability of the gas sensor to provide accurate results for a certain period with a specific sensitivity, selectivity, response, and recovery time [12].

4) Detection Limit: the gas sensor's lowest detected concentration of the analyte under certain conditions, especially at a specific temperature [12].
5) Dynamic Range: the detection concentration range of the gas sensor, from the lower detection limit to the maximum detecting concentration [12].
6) Linearity: the deviation of the determined calibration graph of the testing result compared to a straight line as shown in Figure 7 [12].
7) Response Time: the time used for the gas sensor to respond to a concentration change to a certain value as shown in Figure 8 [12].
8) Recovery Time: the time for gas sensor to return back to the initial working condition after use [12].
9) Working Temperature: the corresponding temperature condition of maximum sensitivity [12].
10) Life Cycle: the operating time of the gas sensor [12].

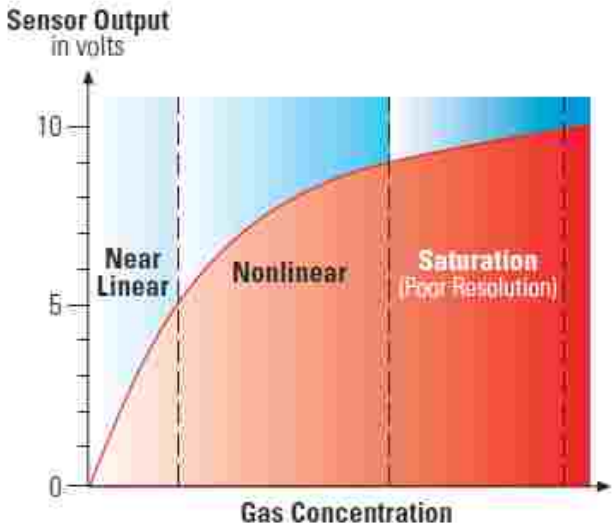


Figure 7. Typical gas sensor output curve [13].

Figure 7 shows the typical gas sensor output curve. The figure clearly demonstrates the relationship between the output of a gas sensor and the gas concentration. The calibration graph of the output is almost a straight near linear line under lower gas concentration. After a certain elevated gas concentration, the magnitude of the sensor output still increases as the gas concentration increases. However, the relationship between the sensor output and the gas concentration starts to become decidedly nonlinear. Finally, when the gas concentration reaches very high levels, the change of the sensor output becomes even smaller with increasing gas concentration due to the saturation reaction sites on the gas sensor [13]. Therefore, the output of the gas sensor is usually designed digitally linearized to the gas concentration [13].

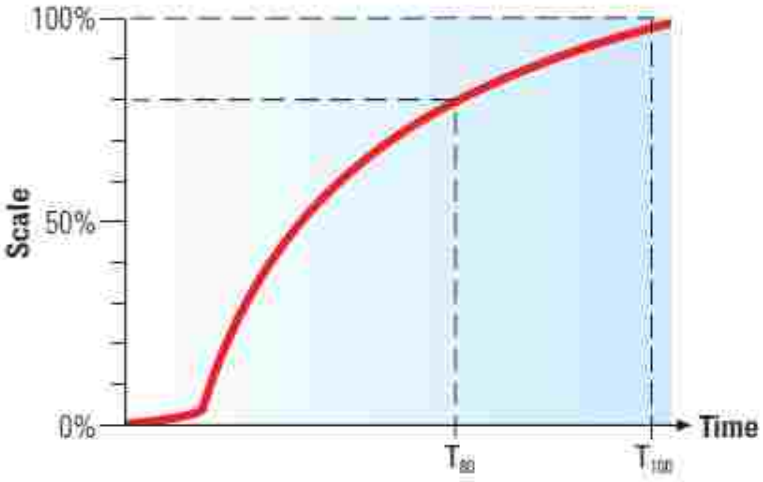


Figure 8. Example of typical MOS gas sensors response [13].

Figure 8 shows the typical relationship between sensor response time and percentage of gas sensor detection range when the gas sensor is exposed to the maximum scale concentration of the gas undergoing testing at saturation level. Let the setting of $T_{80}$ serve as an example. When the time reaches the $T_{80}$ setting, the sensor response scale is 80%. This means it takes the time of $T_{80}$

for the gas sensor to reach 80% of the full detecting range of this gas sensor after having been exposed to a full-scale concentration (at saturation level) of the corresponding gas [13].

The parameters listed above are commonly used to investigate the characteristics of a gas sensors. A good gas sensor is typically distinguished by the following properties: high sensitivity and stability, large dynamic range, wide selectivity, low detection limit, good linear output, and a long lifetime [12]. However, the desirable properties of a gas sensor should also be evaluated under the aspects of different commercial demands and efficiency requirements for various applications. In industrial environments, some applications don't place heavy demands on the properties and characteristics of gas sensors in accordance with the commercial restrictions. For example, the gas sensors used for hazardous gas leak detection typically don't need to satisfy demanding specifications on dynamic range, resolution, and linearity. The purpose of this type of gas sensor is only to monitor hazardous gas leaks in the environment rapidly and efficiently with lower detection limits and short response times [12].

The intrinsic properties and characteristics of sensors are important for the analysis of metal oxide semiconductor (MOS) gas sensors. To evaluate the functions and the efficiency of MOS gas sensors, the analysis needs to focus on the characteristics of the semiconducting metal oxide material deposited on the surface of MOS gas sensors, where the sensing reactions take place. In this dissertation, the sensing response, response time, and recovery time have been the selected parameters for the evaluation of the sensing performance of novel ZnO nanostructure gas sensors.

### 1.2.2 Mechanism

The fundamental operating mechanism of metal oxide semiconductor gas sensors is based on the change of the electrical conductivity of the semiconducting metal oxide during the

interaction process with oxidizing/reducing gases [9]. However, to better understand the mechanism of MOS gas sensors, this theory is not sufficient. The operating mechanism of MOS gas sensors involves the chemical composition of the semiconducting oxide, the surface structure and morphology, and the interaction between the gas particles and surface atoms of semiconductor sensing material [9].

The gas concentration detected by MOS gas sensors is obtained from the change in electrical resistance of the semiconducting metal oxide upon exposure to the gas. However, the resistance of a material is only a directly observable parameter of its electrical conductivity. But this is insufficient for the study and analysis of the mechanism of MOS gas sensors. In general, the measured electrical resistance of ZnO nanorod gas sensors (as is the case in this research study) is composed of two parts which includes the resistance along the hexagonal columnar nanorods and the resistance between individual nanorods [14]. For the first case, the mechanism of the electrical resistance along the hexagonal columnar nanorods is governed by the surface depletion layer model, while the resistance between individual nanorods is based on band bending (potential barrier) [14]. Therefore, the analysis of the mechanism of MOS gas sensor is focused on two issues which are related: the majority carrier concentration and band bending.

*Fundamental Procedure of MOS Gas Sensor*

Generally, in a MOS sensor, the semiconducting metal oxide active sensing material is deposited directly on top of a heating layer, because MOS gas sensors usually require an optimum operating temperature in the range of 100℃ to 500℃ [14]. In the case of an n-type MOS gas sensor, when the semiconducting oxide layer is heated in ambient air to 100℃-200℃, oxygen molecules will adsorb on the surface of the semiconductor and thereby through this oxidation process will be trapping electrons from the conduction band to form oxygen ions. In our case as

the ZnO gas sensor is being heated up to the required higher operating temperature, the ZnO undergoes oxidation thereby losing electrons, while the surface absorbed oxygen molecules undergo reduction and gain electrons. This oxidation process on the surface of n-type ZnO leads to a decrease of the majority carrier density, as shown in Equation 5 [14]. As the oxidation process continues at steadily higher temperatures, additional adsorbed oxygen molecules will attract more majority carriers, thereby promoting more electron transfer from the n-type ZnO conduction band and form $O^-$ and $O^{2-}$ ions as shown in Equations 6 and 7 [14]. In the following step after exposure to the reducing target gas to be tested, oxygen ions react with the target gas molecules and electrons are transferred back to the n-type ZnO conduction band, which increases the majority carrier density. In other words, in this process step the reductant transfers electrons to the oxidant ZnO. The detailed explanation of this reduction reaction is shown as Equation 8 [14].

Initial process step of Sensor Preparation during heating phase to reach operating temperature (oxidation reaction):

$$O_2(gas) + e^- \leftrightarrow {O_2}^-(adsorption) \tag{5}$$

$$\tfrac{1}{2}O_2 + e^- \leftrightarrow O^-(adsorption) \tag{6}$$

$$\tfrac{1}{2}O_2 + 2e^- \leftrightarrow O^{2-}(adsorption) \tag{7}$$

Gas Detection (reduction reaction):

$$X + O^{\delta-} \leftrightarrow X' + \delta e^- \tag{8}$$

Where $X$ is the target gas, $X'$ is the gas after the reaction, $\delta$ is the number of electron which depends on the reaction as shown in Equations 6 and 7.

The schematics of Figures 9 a) & b) explain the detailed oxidation step on the surface of the semiconducting metal oxide and electron adsorption from the conduction band to form an

oxygen ion layer on the sensor surface. This oxidation step leads to a decrease in the majority carrier density (lose of electrons) on the exposed active ZnO sensor surface. Then the third step is to introduce the reducing target gas to be tested (in our case ethanol) to the gas sensor in a controlled test equipment environment. The ethanol molecules react with the oxygen ions on the ZnO surface, thereby reducing the oxygen ions and causing a transfer of electrons back to the ZnO conduction band as shown in the schematics of Figures 9 c) & d) [15]. Following this process step, the electron (majority carrier in ZnO) concentration in the conduction band increases. As a result, the thickness of the depletion layer decreases, which leads to an increase in conductivity (or equivalently a decrease in resistivity) [15].

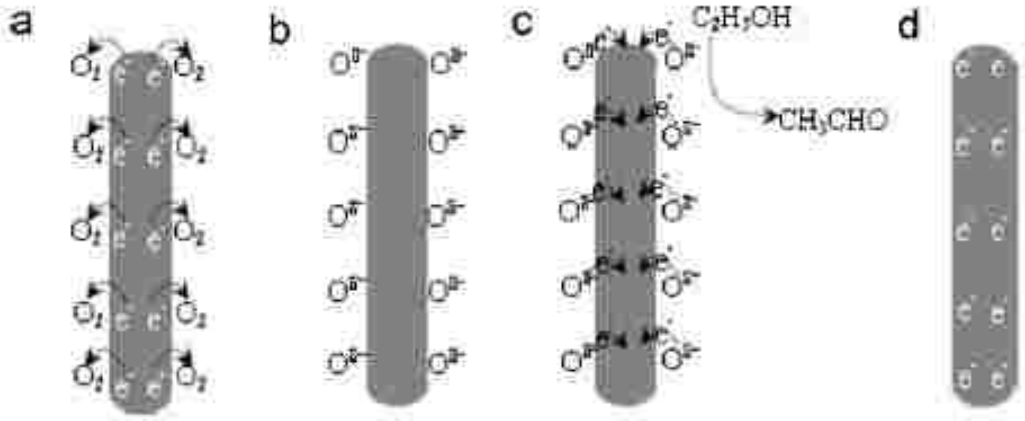


Figure 9. Schematic depiction of the sensing mechanism of ZnO nanorods exposed to ethanol vapors which is governed by surface redox reactions between the semiconductor and the target gas: a) exposure to ambient air during heating to reach the required operating temperature, b) number of ions adsorbed while ZnO undergoes oxidation thereby losing electrons to the oxidizing agent, c) exposure to ethanol, d) ZnO undergoes reduction reaction gaining back electrons to the conduction band [15].

*Majority Carrier Density*

Based on the basic operating principle of MOS gas sensors explained above, the target gas interacts by a redox reaction with the oxygen ions on the active surface of the semiconducting oxide, which leads to a change of the majority carrier concentration. The change in the majority carrier concentration results directly in a modulation of the semiconductor sensor conductivity. However, as illustrated in the introduction of MOS gas sensors, there are two types of MOS gas sensors, n-type and p-type, based on the doping of the semiconducting material used in the sensor. The two types of semiconductors have very different majority carriers and consequently the resulting changes in conductivity are different.

It is well established that the majority carriers in n-type semiconductors are electrons. After the target gas (in this case - reducing gas) has interacted with oxygen negative ions on the active semiconductor surface, the electrons on the oxygen ions are released to the conduction band of the n-type semiconductor. The concentration of electrons (the majority carriers) increases after this reducing gas interaction, which results in an increase in conductivity (or equivalently a decrease in resistivity) [14]. However, the majority carriers in p-type semiconductors are holes. After exposure to the target gas and the interaction between target gas and oxygen ions, the released electrons move to the valence band and recombine with the holes which leads to a reduction in the majority carrier concentration of the p-type semiconductor. This recombination process and loss of majority carriers results in the decrease in conductivity (or equivalently in an increase in resistivity) [14].

Figure 10 shows a comparison between n-type and p-type MOS gas sensors after exposure to a reducing target gas to be tested. Initially both types of MOS gas sensors were heated in air to form oxygen negative ions on the semiconducting sensor surface which causes the change in

resistance. The n-type MOS gas sensor experiences an increase in the resistance during the oxidation process due to the interaction with oxygen leading to a decrease in the majority carrier electron concentration. In contrast, the p-type MOS gas sensor experiences a resistance drop through the oxidation by exciting electrons from the valance band and leaving holes behind [14]. Therefore, the concentration of holes (majority carriers in p-type MOS) increases and the resistance decreases.

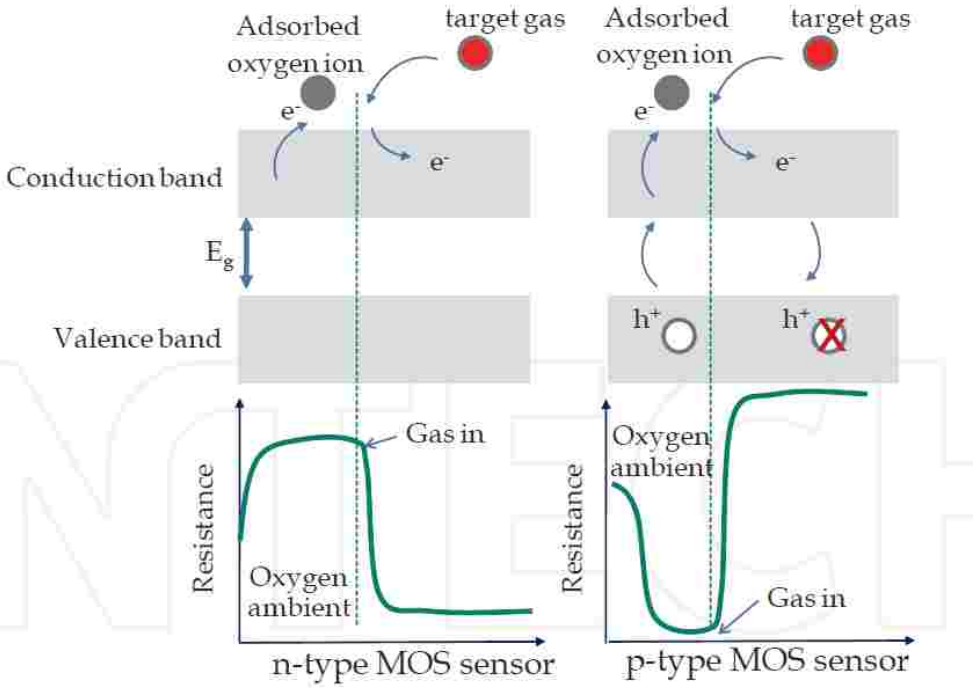


Figure 10. Schematic diagram highlighting the change of the sensor resistance upon exposure to the reducing gas in the case of n-type (left figure) and p-type MOS gas sensors (right figure) [14].

The left side of Figure 10 explains the operating processes during sensing in n-type MOS gas sensors. When a target gas (reducing gas) is introduced into the n-type MOS gas sensor, the gas molecules interact with the oxygen ions on the semiconductor surface and electrons are

released back into the conduction band, which leads to an increase in the electron concentration. The result shows the resistance of n-type semiconductor decreases as the electron carrier concentration increases after the surface interaction with the target gas. The right side of Figure 10 clearly shows the prevalent mechanism operating in p-type MOS gas sensors. The electrons are released after the interaction between the target gas and the semiconductor surface. Subsequently oxygen negative ions inject electrons into the valence band which recombine with the holes [14]. Consequently, this recombination process results in the reduction in holes, which implies the majority carrier concentration of the p-type semiconductor decreases as shown in Equation 13.

n-type MOS gas sensor:

Preparation:

$$O_2(gas) + e^- \leftrightarrow {O_2}^-(adsorption) \tag{9}$$

Gas Detection:

$$X + O^{\delta-} \leftrightarrow X' + \delta e^- \tag{10}$$

Added electron ➔ majority carrier density increases in n-type MOS

p-type MOS gas sensor:

Preparation:

$$O_2(gas) + (h - e^-)pair \leftrightarrow {O_2}^-(adsorption) + h^+ \tag{11}$$

Gas Detection:

$$X + {O_2}^-(adsorption) \leftrightarrow X' + e^- \tag{12}$$

$$h^+ + e^- \leftrightarrow null\ (recombined) \tag{13}$$

Recombination of hole ➔ majority carrier decreases in p-type MOS

*Band Theory (for the case of an n-type MOS Gas Sensor)*

Based on the information introduced in the previous chapter, the majority carrier density of metal oxide semiconductor sustains a corresponding change following exposure to the target gas (which is a reducing or an oxidizing agent). The final majority carrier density value is directly related to the target gas concentration, which is experimentally measured as the conductivity (or resistance) of the MOS gas sensor. In this section, the n-type MOS gas sensor, most relevant for ZnO, is discussed to demonstrate the mechanism of a MOS gas sensor based on band theory.

As pointed out in the introduction to MOS gas sensors, the target gas concentration is directly related to the conductivity or resistance of a MOS gas sensor, which can be measured in a straightforward manner. In general, conductivity in semiconductors is determined by the n- or p-type doping concentration, which is related to the majority carrier density, while conductivity at a semiconductor junction in an MOS system is also affected by the built in potential $V_{bi}$ or depletion layer width W. Therefore, to analyze the resistance or conductivity of a MOS gas sensor, requires studying the built-in potential and depletion layer width [16].

At a semiconductor junction and for example in a MOS system, the change in the majority carrier concentration causes a band bending which is related to the built-in potential [17]. The built-in potential $V_{bi}$ in a semiconductor junction is the potential across the depletion region of a junction at thermal equilibrium [18]. When an MOS gas sensor is exposed to a reducing gas, the gas molecules interact with the negative oxygen ions on the surface, and the resulting reduction reaction transfers electrons to the conduction band of the n-type semiconductor [17]. This reduction electron transfer interaction causes a reduction in the built-in potential $V_{bi}$ and a concomitant reduction of the surface charge, which in turn causes a decrease in the resistance. However, when an MOS gas sensor is exposed to an oxidizing gas, this will oxidize the

semiconductor and reduce the target gas which will gain electrons from the conduction band of the semiconductor and form a charge layer of negative oxygen ions on the semiconductor sensor surface. If the surface of the MOS sensor is already covered with one layer of negative charge formed by negative oxygen ions from the previous oxidation reaction, the reducing gas will react with the existing oxygen ions and lose electrons to the n-type semiconductor as a result of this reduction reaction. A chemical oxidation reaction with an n-type semiconductor causes a negative charge build-up on the semiconductor surface and the built-in potential $V_{bi}$ to increase (as shown in Figure 11, which implies the resistance of the MOS gas sensor increases because the depletion is simultaneously increased and thereby decreases the available cylindrical conductive channel in a nanorod sensor.)

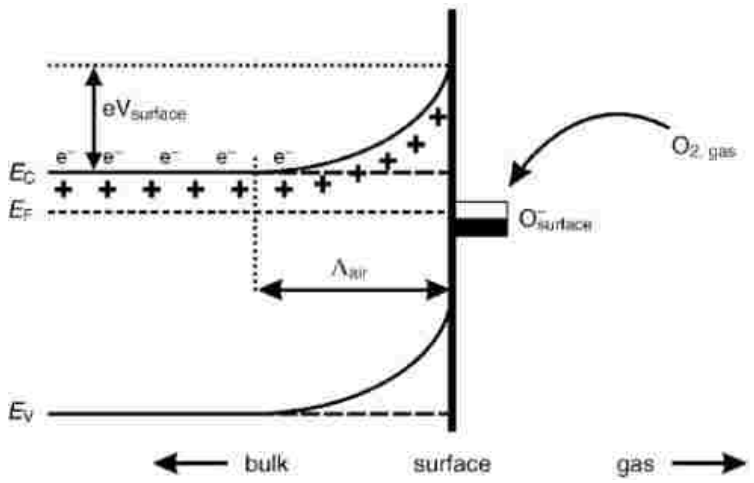


Figure 11. Schematic diagram of band bending at the semiconductor sensing surface exposed to a target gas representing a typical case of a generic MOS sensor [16].

The physics and theory of the relationship between the built-in potential $V_{bi}$ and the majority carrier concentration is based on the one-dimensional equation of Poisson states as shown in Equation 14.

$$\frac{d^2\varphi}{dx^2} = \frac{qN_i}{\epsilon}\epsilon_0 \tag{14}$$

where $\varphi$ is the potential, $N_i$ is the net density of ions in the space-charge region (depletion region), $\epsilon$ is the dielectric constant of the semiconductor, and $\epsilon_0$ is the permittivity of free space [19]. The donor density $N_D$ is independent of $x$ [19]. Therefore, the built-in potential can be defined as follows in Equation 15.

$$V(x) = \varphi_b - \varphi(x) \tag{15}$$

where $\varphi_b$ is the potential in the bulk of the semiconductor [19]. Then combining Equation 14 and 15 leads to Equation 16.

$$\frac{dV}{dx} = \frac{qN_i(x - x_0)}{\epsilon\epsilon_0} \tag{16}$$

where $x_0$ is the width of the space-charge region [19]. From the integration of Equation 16, follows Equation 17:

$$V = \frac{qN_i{x_0}^2}{2\epsilon\epsilon_0} \tag{17}$$

When $x = x_0$, $V$ equals to zero [19]. Therefore, the value of the surface barrier (built-in potential) $V_s$ ($V$ at $x = 0$) is shown in Equation 18 as:

$$V_s = \frac{qN_i{x_0}^2}{2\epsilon\epsilon_0} \tag{18}$$

For n-type material, $N_D x_0 = N_i x_0$ (the number of electrons per thickness of $x_0$ in the depletion region) also equals to $N_s$ (the number of electrons which moved to the surface). Therefore, Equation 18 changes to

$$V_s = \frac{qN_s{}^2}{2\epsilon\epsilon_0 N_i} \tag{19}$$

The energy $qV_s$ is the energy that electrons obtain to move to the surface, which can also be considered as the different energy level between the surface and the bulk [19]. Because $N_s$ is

defined as the number of electrons which moved to the surface, $N_s$ can also be defined as the number of electrons lost from the conduction band during oxidation or the number of electrons moved back to the conduction band during reduction. This means $N_s$ is related to the electron (majority carrier in n-type) concentration. During oxidation, electrons move from the conduction band to the surface, which means $N_s$ increases and the electron concentration in the semiconductor decreases. Based on Equation 19, the built-in potential ($V_s$) increases as the number of electrons which moved to the sensor surface ($N_s$) increases, and vice versa. Therefore, the conductivity or resistivity can be investigated from the built-in potential $V_{bi}$ and majority carrier concentration.

*Width of the Depletion Layer W*

The conductivity of an MOS gas sensor is eventually defined by the width of the depletion region at the semiconductor surface junction, which is related to the built-in potential $V_{bi}$ as shown in Equation 20.

The total depletion layer width:

$$W = \sqrt{\frac{2\varepsilon_S}{q}\left(\frac{N_A + N_D}{N_A N_D}\right) V_{bi}} \tag{20}$$

Figure 12 shows the schematic of the mechanism of structural and band models before and after exposure of the MOS gas sensor to a reducing gas (CO) [16]. When the semiconductor is exposed to oxygen, oxygen molecules attract electrons from conduction band and form a layer of negative oxygen ions on the surface, which causes an increase in the width of the depletion region and potential barrier as shown in Figure 12 a). In the case of polycrystalline semiconductor sensors, the potential barrier makes it hard for the electrons to move through the grains and across the grain boundaries, which causes an increase in the resistance. After exposing the MOS sensor material to the reducing gas (CO) as shown in Figure 12 b), CO gas molecules interact with negative oxygen ions and release electrons back to the conduction band, which causes an increase in the majority

carrier density. Based on Equations 19 and 20, the potential barrier and the depletion layer width decrease consequently. For polycrystalline semiconductor sensing material, the lowered Schottky barrier between two grains makes it convenient for electrons to move in sensing layers through different grains [16]. Therefore, the resistance decreases after exposure to a reducing target gas. Figure 12 (bottom) demonstrates the depletion layer change on the surface of cylinder during the Sensor Preparation step (Air) and the Gas Detection step (Reducing gas) of the reducing gas detection of MOS gas sensors.

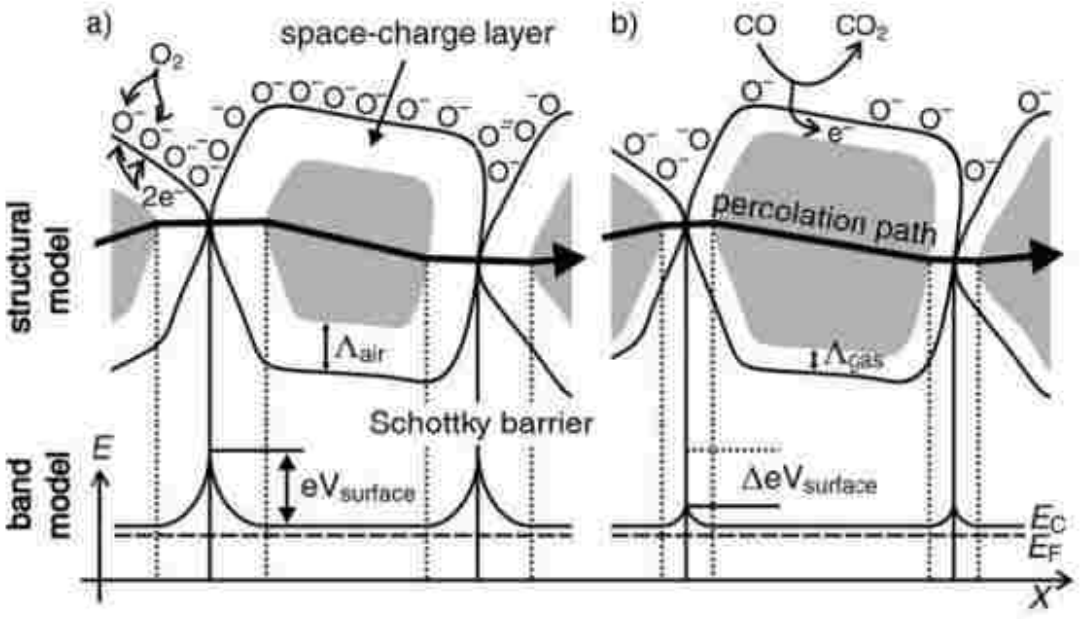


Figure 12. (a) Schematic structural model and band model of the conduction mechanism in polycrystalline active sensing material a) before exposure and b) after exposure to the target gas carbon monoxide CO [16].

Figure 13 demonstrates schematically the depletion layer width change on the surface of a single ZnO nanorod cylinder during the Sensor Preparation step (oxidation in Air) and the Gas

Detection step (Reducing gas) of the reducing gas detection of MOS gas sensors. The increasing constriction of the available conducting channel in the center of the nanorod by the expanding surface depletion layer width is clearly shown as a function of ongoing high temperature oxidation in air to reach the optimum working temperature. Such a constriction of the conducting channel triggers a rise in resistance.

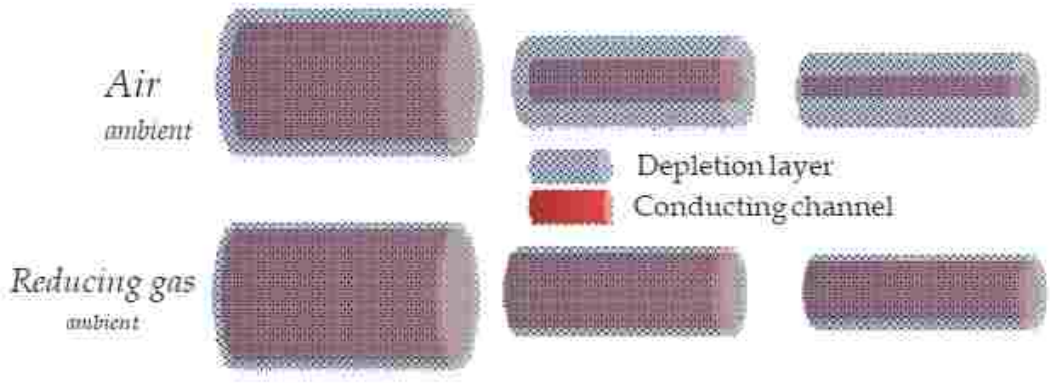


Figure 13. Schematic depiction of depletion width changes on the surface of a ZnO nanorod cylinder in the Sensor Preparation step (in Air) and subsequently during the Gas Detection step (in Reducing gas) upon exposure to the reducing gas of a generic nanorod MOS gas sensor. During the oxidation reaction of the heat up phase in air the surface depletion layer widens considerably, thereby constricting the cross-section of the available conducting channel in a ZnO nanorod, which is causing a resistance increase. Conversely, upon exposure to the reducing gas the surface depletion layer width gets reduced. This causes a widening of the available conducting channel cross-section and a concomitant drop in the resistance [14].

In summary, it is well established that the interaction between a metal oxide semiconductor gas sensor and a target gas involves chemical oxidation and reduction reactions. The relationship between the type of MOS gas sensor and the majority carrier concentration has been explained in

the previous sections. However, the interaction between the MOS gas sensor and the two different possible types of target gases are also different. Basically, there are two different types of target gases to be detected: oxidizing gases or reducing gases. An oxidizing gas is generally known as the gas that provides oxygen ions during the semiconductor's oxidation reaction, like oxygen. Conversely, a reducing gas is the type of gas that combines with oxygen during the semiconductor's reduction, like CO. The relationships among the two types of MOS gas sensors to two different gases, the majority carrier density, and the resistance are shown in Table IV.

TABLE IV

Resistance change in response to exposure to either oxidizing or reducing target gas [20].

| Type of MOS | n-type (Majority: electron) | | p-type (Majority: hole) | |
|---|---|---|---|---|
| Gas Classification | Oxidizing | Reducing | Oxidizing | Reducing |
| Surface Oxygen Ion Density | Increase | Decrease | Decrease | Increase |
| Majority Carrier Density | Decrease | Increase | Increase | Decrease |
| Potential Barrier | Increase | Decrease | Decrease | Increase |
| Resistance | Increase | Decrease | Decrease | Increase |

### 1.3 Dissertation Objectives

Motivated by the desire to improve the serious shortcoming of poor sensing performance of the current state-of-the-art ZnO gas sensors, a new device process integration and a novel sensor architecture design was conceived which serves to significantly increase the surface-to-volume

ratio of the sensor device and thereby improves the sensing performance of ZnO gas sensors. The flow chart in Figure 14 explains the motivation and the objectives in this dissertation.

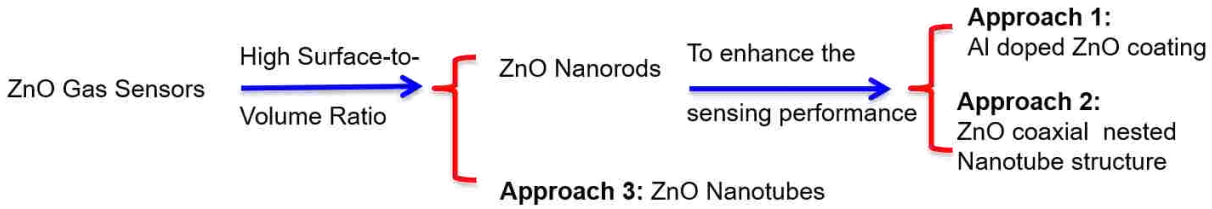


Figure 14. Dissertation motivation showing flow chart of the three experimental approaches pursued to achieve three objectives.

Figure 15 provides a graphic explanation of the increased surface-to-volume ratio gained by synthesizing ZnO nanowires on ZnO thin films versus the case of a conventional flat planar ZnO film sensor.

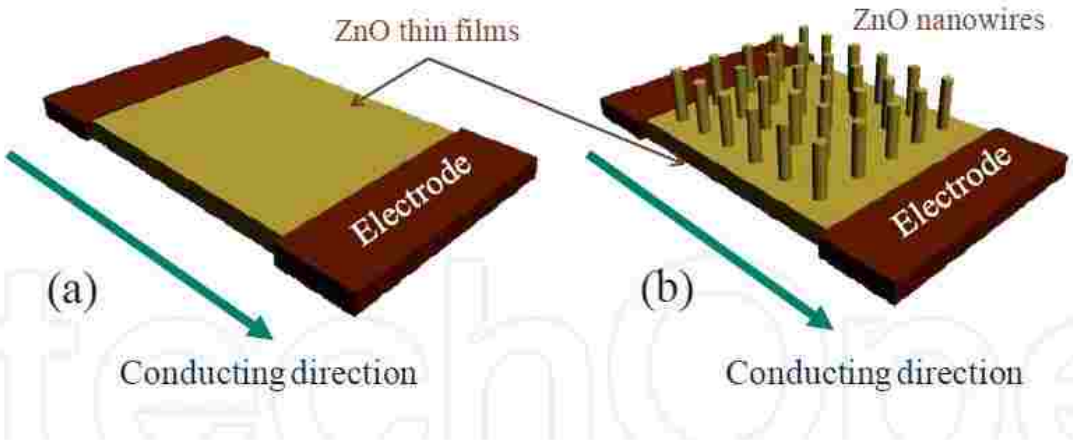


Figure 15. Schematic depiction of the increased surface-to-volume ratio gained for generic ZnO gas sensor devices by synthesizing ZnO nanorods on ALD fine grained ZnO seed films versus the case of a conventional flat planar ZnO film sensor [14].

Figure 16 demonstrates a graphical presentation of the concept of co-axial nested tube-in-tube nanostructure devices after removing the sacrificial $Al_2O_3$ layer separating the outer nanotube from the center nanotube [21]. This synthesis concept provides an opportunity to expose additional reaction surfaces to participate in the gas sensing process and to increase the surface-to-volume ratio of the gas sensor device, which is illustrated in detail in Chapter 4: Objective 2 and Chapter 5: Objective 3.

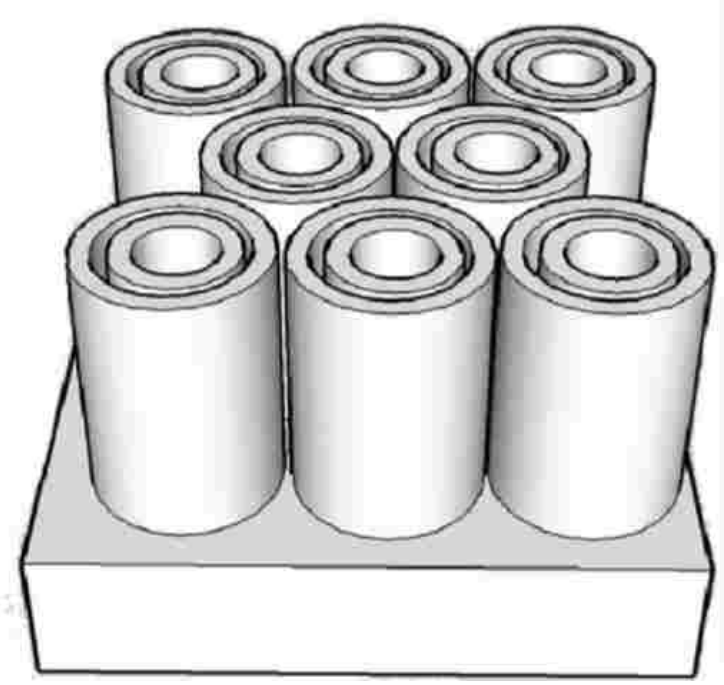

Figure 16. Graphical presentation of the concept of co-axial nested tube-in-tube nanostructure after removing the sacrificial $Al_2O_3$ layer separating the outer nanotube from the center nanotube [21].

Based on Equation 8, the electron density adsorbed to the surface can be calculated by Equation 21 [14].

$$\frac{d_n}{d_t} = k_{gas}[O]^{\delta}[X]^{\delta} \tag{21}$$

where $n$ is the electron density under the gas atmosphere, and $k_{gas}$ is the reaction rate constant defined as in Equation 22 [14].

$$k_{gas} = Aexp(-E_a/k_BT) \tag{22}$$

where $E_a$ is the activation energy of a reaction, $k_B$ is the Boltzmann constant, and $T$ is absolute temperature [14].

After integrating Equation 21 under gas ambient, the sensitivity relation is shown in Equation 23 and 24 [14].

$$n = \Gamma_t k_{gas}[O]^{\delta}[X]^{\delta} + n_0 \tag{23}$$

$$S_g = \frac{R_{gas}}{R_{air}} = \frac{n}{n_0} = \frac{\Gamma_t k_{gas}[O]^{\delta}[X]^{\delta}+n_0}{n_0} = \frac{\Gamma_t k_{gas}[O]^{\delta}[X]^{\delta}}{n_0} + 1 \tag{24}$$

Conventionally, the surface-to-volume ratio can be defined by the adsorbed oxygen ion density [14]. Therefore, the adsorbed oxygen ion density can be defined by Equation 25.

$$[O] = \frac{\sigma_0 \varphi V_m}{V_s} \tag{25}$$

where $\sigma_0$ is the number of oxygen ions per unit area, $\varphi$ is the ratio of surface area per volume of $V_m$, and $V_s$ is the system volume [14]. After substituting Equation 25 to Equation 24, we can get the sensitivity of the gas sensor related to the surface-to-volume ratio from Equation 26 [14].

$$S_g = \frac{\Gamma_t k_{gas}[\frac{\sigma_0 \varphi V_m}{V_s}]^{\delta}[X]^{\delta}}{n_0} + 1 \tag{26}$$

Equation 26 clearly shows the relationship between the sensitivity and the surface-to-volume ratio of MOS gas sensor, which also illustrate the agreement to the motivation of this dissertation.

Compared to conventional ZnO thin film gas sensors, ZnO gas sensors based on nanorods and nanotubes exhibit a significant improvement on the sensing performance due to a much higher surface-to-volume ratio. To further enhance the sensing performance, the first two approaches

were conceived employing ALD AZO coatings and increasing surface-to-volume ratio with additional reaction surfaces. Approach 3 combines the technical advantages of approach 1 and 2 with ALD AZO coating and additional reaction surfaces. Furthermore, approach 3 establishes a true top-down technology and renders it ready for commercialization.

***Objective 1:*** *ALD 3-D Wrap-around AZO Coating of ZnO Nanorods which serves to increase the Oxygen Vacancies to significantly increase the Sensing Response*

Among the various gas sensors based on suitable semiconductor materials, ZnO has been widely investigated for its electronic and photonic applications due to its low cost, good electrical conductivity, wide band gap of 3.37 eV, ~60 meV large exciton binding energy. Currently gas sensors based on ZnO nanorods have been widely employed due to their high electrochemical stability, nontoxicity, high surface-to-volume ratio, suitable doping. Especially, Al doped ZnO thin film coatings were synthesized on the surface of ZnO nanorods by ALD to further enhance the sensing performance of ZnO nanorod gas sensors by supplying additional oxygen vacancies and extra electrons. For this objective, Atomic Layer Deposition (ALD) technology was introduced for two required tasks: a) to deposit fine grained polycrystalline ZnO seed layers on Silicon substrates for hydrothermal growth of ZnO nanorods and b) finally to coat AZO thin films on the surface of ZnO nanorods due to its precisely controlled deposition thickness and composition. The concentration of the aluminum dopant was accurately controlled to 2%. After the ALD synthesis of a ZnO seed layer on the Si substrate, the ZnO nanorods were grown by hydrothermal technique at 80℃ for 16 hours in a solution of hexahydrate ($Zn(NO_3)_26H_2O$) and hexamethylenetetramine ($(CH_2)_6N_4$) dissolved in 60 mL DI water. The final step is to coat the surface of the synthesized ZnO nanorods with AZO thin films by ALD.

A gas sensor testing system was designed and built in-house with a sealed reaction chamber to investigate the sensing performance of ZnO nanorod gas sensors at various ethanol vapor concentrations at different temperatures. With the custom designed electrical circuit, the physical change of ZnO nanorod gas sensors in terms of resistance was detected and analyzed for the study of the ZnO nanorod gas sensors' sensing performance. An RTD was used to measure the temperature of the reaction chamber in real-time and to provide the temperature feedback signal for the temperature control of the heater. An interface was designed by LabView to display and record the real-time values of the circuit current, the voltage of the reference resistor, the voltage on ZnO gas sensor, the resistance of ZnO gas sensors, and of the control of the sealed reaction chamber temperature. The custom designed and built gas sensor testing system used for the objective 1 is introduced in Chapter 2 Section 3: Gas Sensor First Generation Prototype Testing System. By supplying oxygen vacancies and additional electrons, AZO thin film coatings significantly improved the sensing performance of ZnO nanorod gas sensors which was extensively verified from the sensing response tested.

The experimental procedures and sensing performance results of Objective 1 are further introduced and discussed in Chapter 3.

***Objective 2:*** *ZnO Nanorod Gas Sensors with Novel Nested Nanorod-in-Nanotube Architecture using $Al_2O_3$ Sacrificial Layers to Expose Additional Sensing Surfaces*

Numerous methods have been applied to enhance the sensing performance of ZnO nanorod gas sensors. However, the majority of methods are based on coatings with specific doping to enhance the sensing performance of ZnO nanorod gas sensors, like Pd, [22] InSb, [23] Ni, [24] etc. In our case, for the approach taken in this study a coaxial nanorod/nanotube structure was

fabricated to improve the sensing response of ZnO nanorods to ethanol vapor based on an increased surface-to-volume ratio due to a novel device architecture. Single crystal ZnO nanorods were grown by hydrothermal method on fine grained polycrystalline ZnO seed layers deposited by ALD. Subsequently an $Al_2O_3$ sacrificial layer was deposited by a 3-D wrap-around ALD coating on the surface of the ZnO nanorods for the synthesis of a coaxial nested ZnO nanotube sensor. This process was followed by one layer of ALD ZnO layer coating to complete the formation of ZnO nanotubes. To expose the $Al_2O_3$ sacrificial layer on the sample surface, a Precision Ion Polishing System (PIPS) was introduced to remove by ion milling the top coating cover generated by the ALD deposition, which is further explained introduced in Chapter 2. The $Al_2O_3$ sacrificial layer was preferentially etched off by Sodium Hydroxide (NaOH) based on the different selective solubility ranges of $Al_2O_3$ and ZnO. In this manner, nested coaxial ZnO nanorod/nanotube gas sensors were synthesized with additional exposed sensing reaction surfaces for the detection of ethanol vapors.

In the course of this work, a newly designed second-generation gas sensor testing system was custom designed and built for this objective with two Mass Flow Controllers (MFC) to accurately control the concentration of the target ethanol vapor. The sensing performance of conventional ZnO nanorod gas sensors compared to the novel nested ZnO nanorod/nanotube gas sensors were benchmarked and recorded by the second-generation gas sensor testing system under various concentrations of ethanol vapor at different temperatures. The optimum working temperature, the saturation level, and enhancement gain of the novel nested ZnO nanorod/nanotube gas sensors were analyzed and recorded based on the sensing response results.

The experimental details and results are described in more detail and analyzed in Chapter 4.

***Objective 3:*** *Novel ZnO Nanotube Devices Synthesized by Template Replication Technology using Porous Substrates.*

To properly prepare novel nested ZnO nanostructure gas sensors for pre-production and ultimately for commercial applications, the reproducibility and reliability has to be considered in the research phase of ZnO gas sensors. With this goal in mind, a true top-down technology was introduced by using microelectronics clean room proven mask and photolithography patterning techniques for the synthesis of ZnO nanotube gas sensors with high surface-to-volume ratio and a controlled nanotube density in conjunction with template replication. For this objective, nested ZnO nanotubes were fabricated inside porous templates, which include porous Anodic Aluminum Oxide (AAO) and porous Silicon, for the precise detection of ethanol vapor concentrations. Atomic Layer Deposition technology was employed to synthesize $Al_2O_3$ sacrificial layers and ZnO thin films inside the pores of porous templates with accurately controlled thickness and composition. PIPS ion milling was used to remove the top cover after ALD deposition and NaOH was sequentially introduced to preferentially etch away the sacrificial layer. This new process generates novel nested ZnO nanotube gas sensors in porous templates for the accurate detection of ethanol vapors. To further improve the sensing performance, ALD AZO coatings were deposited on the surface of the nested ZnO nanotube gas sensors.

The advantages of approach 1 and 2 were combined in this approach. The sensing performance of ZnO nanotube gas sensors with one coaxial layer and two coaxial layers was measured and analyzed by the gas sensor testing system for a comparative study. Additionally, the sensing performance of ZnO nanotube gas sensors before and after coating with ALD AZO thin films were also investigated. The experimental procedures and sensing performance comparison are studied in Chapter 5.

# CHAPTER 2

# EXPERIMENTAL TECHNIQUES

This chapter is focusing on the description of the four major techniques used for novel nested ZnO nanostructure gas sensors synthesis and analysis, which consist of Atomic Layer Deposition, Hydrothermal Growth Method, Precision Ion Polishing System (PIPS), and the sealed gas sensor testing system.

## 2.1 Atomic Layer Deposition

### 2.1.1 Introduction

Numerous methods and technologies have been utilized to synthesize planar ZnO thin films, like radio frequency magnetron sputtering [25], electron beam evaporation [26], sol-gel spin coating [27], dip coating [28], successive ionic layer adsorption and reaction (SILAR) method [29], and spray pyrolysis [30]. However, the thickness of ZnO thin films synthesized by these methods cannot reach the nanotechnology thickness requirements in this dissertation within 20 nm. Therefore, in this dissertation, Atomic Layer Deposition was introduced for the processes of the deposition of ZnO seed layer on Si wafer, AZO coatings, $Al_2O_3$ sacrificial layer, and ZnO 3D thin film coatings, which can only be realized by ALD technology with precisely Angstrom controlled deposition thickness and composition. Due to the ALD deposition advantage of one atomic layer thickness per growth cycle, the ALD deposition growth rate for ZnO by using Diethylzinc (DEZ) and water vapor as precursors is controlled to around 1.8 $\dot{A}$/cycle at 180℃ as shown in Figure 17 [31].

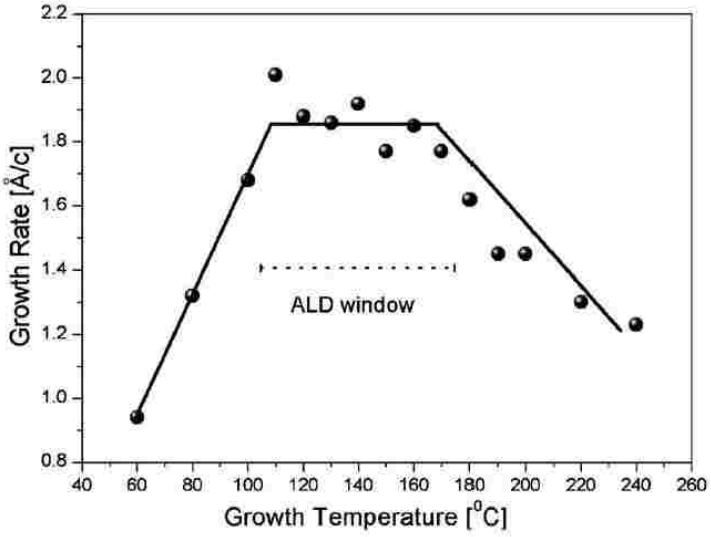


Figure 17. ZnO growth rate versus growth temperature with Diethylzinc and water vapor as ALD precursors. The constant growth rate plateau between ~ 105 – 170 ℃ establishes the ALD process window [31].

This chemical reaction for ZnO thin films deposition by ALD with DEZ ($C_2H_5 - Zn - C_2H_5$) and water ($H_2O$) as precursors is shown in Equation 27 [31].

$$C_2H_5 - Zn - C_2H_5 + H_2O \rightarrow ZnO + 2C_2H_6 \quad (27)$$

The reaction formula can also be separated into two equations during two phases [31].

DEZ phase [31]:

$$surface - OH + C_2H_5 - Zn - C_2H_5 \rightarrow surface - O - Zn - C_2H_5 + C_2H_6 \quad (28)$$

Water phase [31]:

$$surface - O - Zn - C_2H_5 + H_2O \rightarrow surface - O - Zn - OH + C_2H_6 \quad (29)$$

Atomic Layer Deposition is defined as a thin film deposition technique which is based on the sequential use of self-limiting gas-to-solid reactions. The significant advantage of ALD technology is to precisely control the thickness, stoichiometry, composition, and uniformity of the

deposition films due to the surface saturation self-limiting chemical reaction between two precursors. The basic mechanism of ALD technology consists of sequentially introducing alternate precursor pulses in gaseous phase to the reaction chamber which result in subsequent chemisorption and surface reactions [32]. Figure 18 shows the sequential deposition procedure of ALD technology. First, precursor A is introduced into the chamber for certain time to control the input volume. With the help of carrier gas $N_2$ and pump, the unreacted precursor A and byproducts are vacuumed away from the chamber. Then a short precursor B vapor pulse is released into the chamber. This is known as one single ALD growth cycle. To achieve nanoscale thin films with a controlled thickness, more ALD growth cycles are required with a predetermined number of n ALD cycles based on the growth rate of the material. Therefore, the thickness and composition are controlled with atomic Angstrom precision.

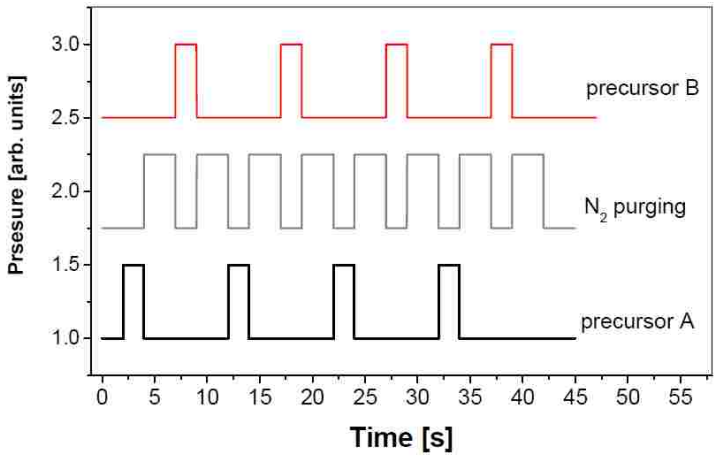


Figure 18. Schematic of ALD sequential pulsed deposition process highlighting the two precursor gas pulses and the $N_2$ carrier gas [31].

Taking $Al_2O_3$ thin films deposition as an example, trimethylaluminum (TMA, $Al(CH_3)_3$) and DI water vapor are the common chemicals used as ALD precursors to synthesize $Al_2O_3$ thin

films. Figure 19 explains schematically the example of the $Al_2O_3$ thin films deposition process. First, a cleaned and properly prepared substrate, for example a Si wafer, with hydroxyl surface termination to optimize reaction sites with hydroxyl groups is placed in the ALD reaction chamber. Then, TMA as the first precursor, which contains three methyl groups, is introduced into the reaction chamber when the ALD valve releases a short gas pulse of TMA. One of the three methyl groups reacts with a hydroxyl group (-OH) and leaves one layer of Al with two methyl groups on the surface as shown in Figure 19 ② and ③. The unreacted TMA and any byproducts (methane, $CH_4$) are pumped out, after which the second precursor pulse in the form of DI water vapor is released into the reaction chamber as shown in Figure 19 ④. With hydroxy group, $H_2O$ reacts with the two methyl groups left with Al. Therefore, one layer of $Al_2O_3$ with a hydroxyl group is formed on the surface of the substrate as shown in Figure 19 ⑥. The remaining hydroxyl group is available for the next chemical reaction. This process is defined as one super reaction cycle. More super cycles are required to obtain $Al_2O_3$ thin films with final desired thickness. For instant, 82 ALD growth cycles are required to synthesize 10 nm $Al_2O_3$ thin films with an ALD $Al_2O_3$ growth rate of 1.22 $\dot{A}$/cycle at 200℃ [33]. The chemical reaction of the synthesis of $Al_2O_3$ thin films are shown in 1st reaction cycle (Equations 30 and 31) and nth reaction cycle (Equations 32 and 33).

1st reaction cycle:

$$Si - OH + Al(CH_3)_3 \rightarrow Si - O - Al(CH_3)_2 + CH_4 \quad (30)$$

$$Si - O - Al(CH_3)_2 + 2H_2O \rightarrow Si - O - Al - OH + 2CH_4 \quad (31)$$

nth reaction cycle:

$$-Al - OH + Al(CH_3)_3 \rightarrow -Al - O - Al(CH_3)_2 + CH_4 \quad (32)$$

$$-Al - O - Al(CH_3)_2 + 2H_2O \rightarrow -Al - O - Al - OH + 2CH_4 \quad (33)$$

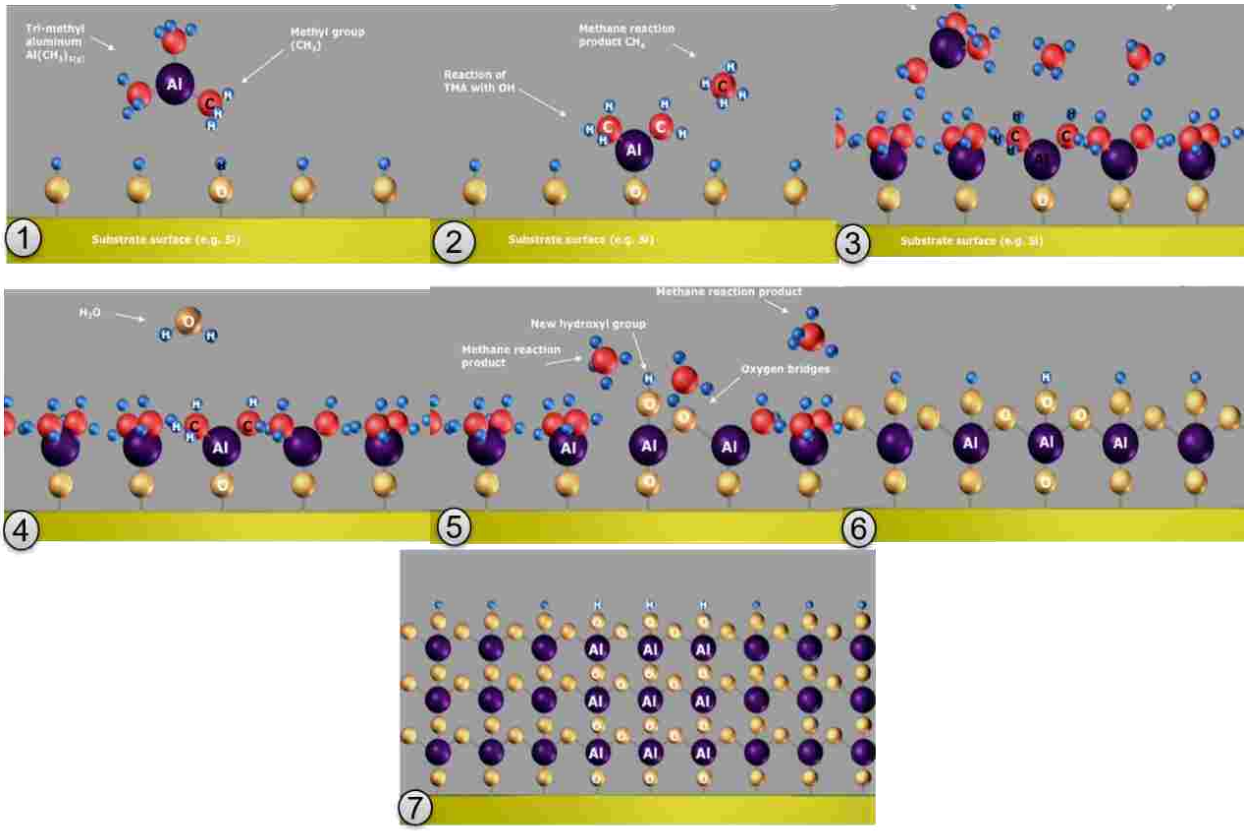


Figure 19. Schematic of ALD process for the synthesis of $Al_2O_3$ thin films with a classic atomic layer by atomic layer deposition.

### 2.1.2 Custom-built ALD System for ZnO Project

There are three complete ALD systems in our lab, which have been applied for various other projects, like thermoelectric material (PbTe-PbSe) depositions, iridium synthesis on Si, $TiO_2$ coating, etc. However, to avoid cross-contamination, one ZnO deposition related ALD system with brand new ALD reaction chamber and controller was custom designed and built with a stable temperature control system and accurate precursor input control system.

To properly design a new controller used for the ALD system, the first priority is to understand all the required functions the controller needs to perform. Basically, the controller

needs to provide four functions: temperature control of each heater element for the reaction chamber, gauge signal reading, mass flow controller (MFC) communication, and time control of each ALD valve opening to release the precursor gas pulse into the chamber. As shown in Figure 20, the controller reads the feedback signal from each temperature indicator (RTD) and provides the power signal to the corresponding heater to form a closed-loop temperature control system. The Gauge is used to indicate the vacuum pressure in the reaction chamber and provides the ready signal by the controller to guarantee the chamber pressure has reached the required vacuum value for ALD thin films deposition. The $N_2$ carrier gas volume control takes on a significant role in ALD technology due to its two important functions. First, the $N_2$ carry-gas carries the precursor vapor into the chamber without any coating on the surface of the manifold (the stainless-steel input channels of all ALD precursors). The second function is to flush clean the reaction chamber and to remove any unreacted precursors and byproducts during the process gap between the input of the two different precursors. Therefore, a mass flow controller (MFC) is applied to control the input volume of the carry-gas $N_2$. The MFC communicates with the ALD controller by reading the desired volume signal from the controller and providing a real-time volume signal to the controller.

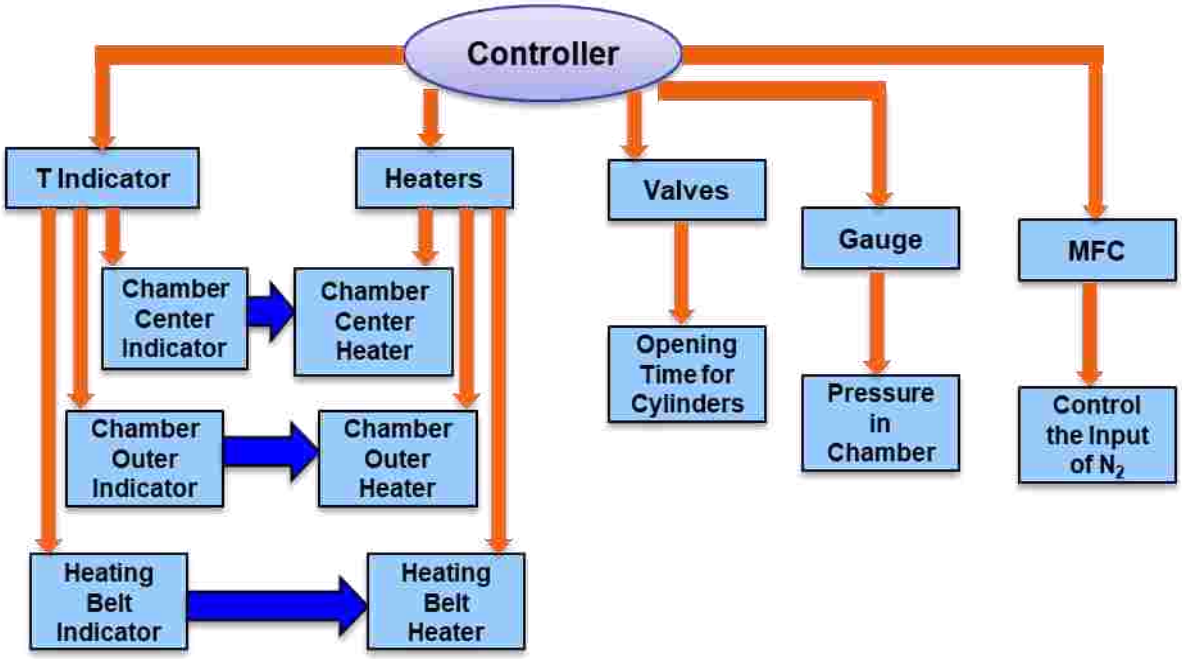


Figure 20. Schematic of ALD electronic control system diagram with four basic functions: temperature control, pneumatic ALD valve control, gauge signal indication, and mass flow controller control.

In ALD technology, each specific thin film material synthesis requires its own corresponding ALD precursors and certain composite materials require even more than one ALD precursor. Furthermore, the ALD growth rate depends on the deposition temperature. The chemical precursor species and the deposition temperature have to be incorporated into the programming of every ALD deposition recipe, which leads to a variety on the input volume of the precursor. Special pneumatic ALD valves are installed on the equipment to control the release of extremely short puffs of precursor vapor on a millisecond time scale into the ALD reaction chamber. Therefore, the ALD controller is required to provide a control signal to each pneumatic ALD valve for the control of cylinder opening time on a millisecond time scale.

A Compact Rio 9068 from National Instruments was utilized to design the ALD controller due to its extensive multi-functionality, high stability, accuracy, and suitability for both Field Programmable Gate Arrays (FPGAs) and real-time control. The Compact Rio 9068 can be considered as a controller base unit, which contains 8 slots for different functional modules based on the design requirements. The technical information of the modules and function used in the ALD controller design is shown in Table V.

TABLE V

National Instruments Modules used in ALD controller design.

| Module | Quantity | Function |
|---|---|---|
| NI 9217 | 2 | Read temperature signals from RTDs |
| NI 9263 | 2 | Provide power signals to heaters |
| NI 9474 | 1 | Provide control signals to valves |
| NI 9381 | 1 | Read gauge pressure signal and communicate with MFC |

For a stable temperature control of each reaction chamber heater, a closed-loop control system is required which collects feedback signals from the RTD circuit. The working principle of an RTD device is based on a resistance change as a function of the temperature. Therefore, an RTD is usually installed into a temperature signaling circuit. Figure 21 demonstrates a flow chart of the closed-loop temperature control system used in the ALD controller design. For example, in case the ALD reaction chamber needs to be heated up to 200℃ which is considered as setup temperature. After sending the temperature requirement to the controller by the programmed

interface, the controller sends out the calculated control signal to the relay in the heater power circuit. Then the heater will receive the corresponding power. Then the RTD circuit indicates the real-time temperature of the heater and sends the temperature signal to the controller. Therefore, the controller can modify the output power signal as required by the feedback signal, like reducing the output when the real-time temperature is higher than 200℃ or increasing the output when the temperature is lower than 200℃.

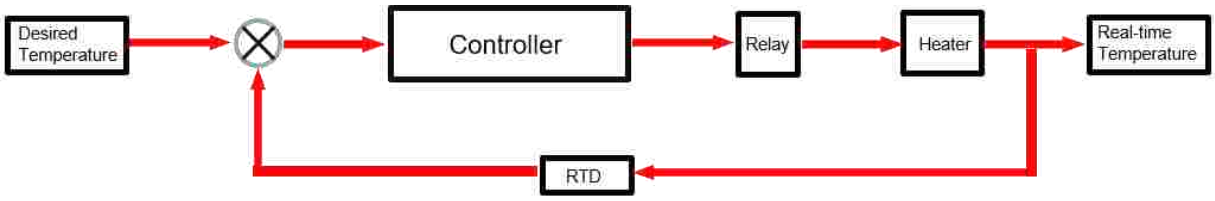


Figure 21. Flow chart of the designed closed-loop temperature control system.

Figure 22 (top) shows the programmed ALD control system software interface which is using LabView 2013. The software interface includes temperature control, $N_2$ carrier-gas volume control, MFC control, pressure indication, recipe edition table, and pneumatic valve operating indication lights. The three figures in Figure 22 (bottom) show the hardware setup after completion of connecting the controller with the ALD equipment.

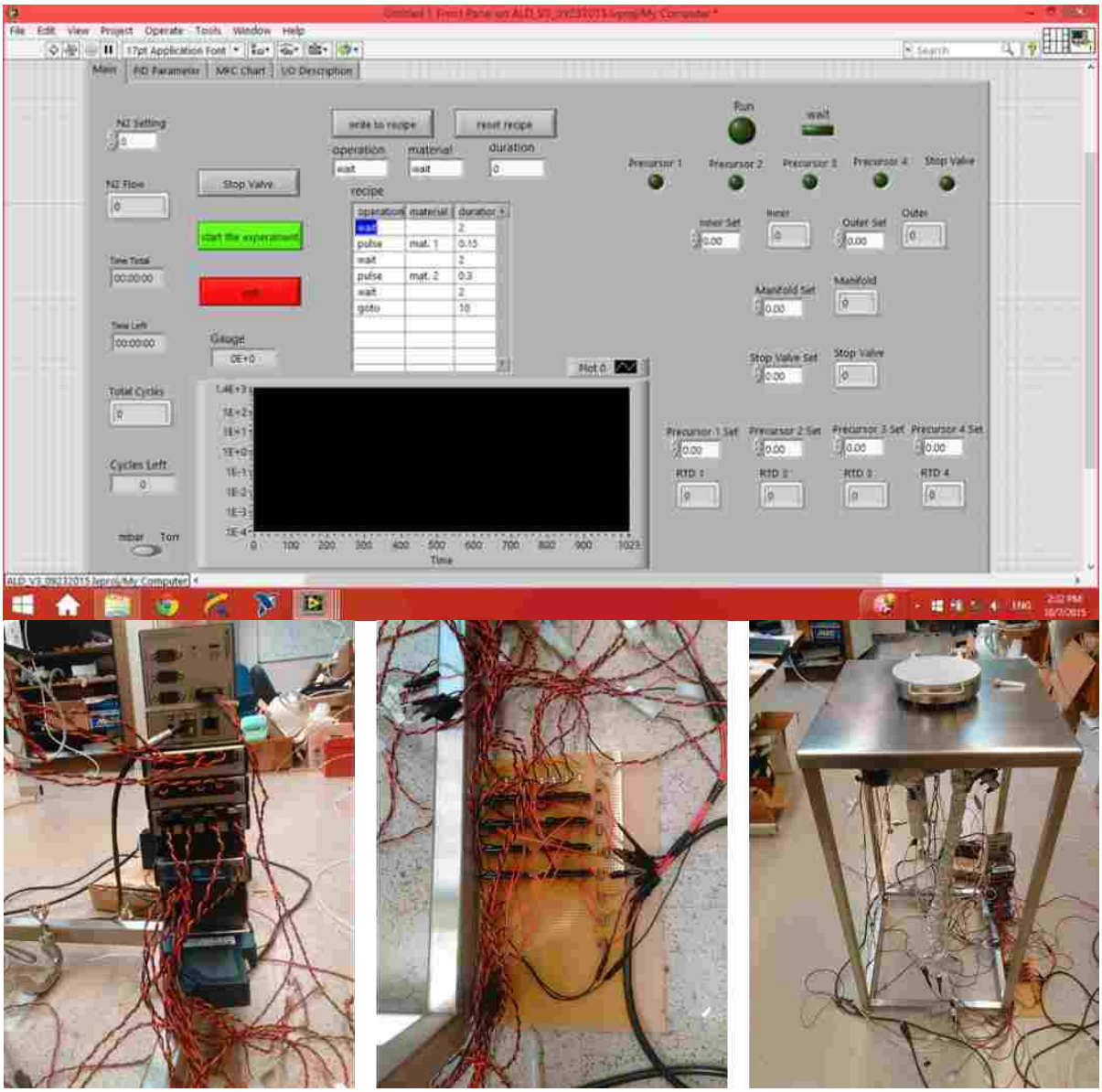


Figure 22. ALD control system software interface (top) and custom-built hardware setup with controller (bottom three).

## 2.2 Hydrothermal Growth Method

There are numerous methods and technologies which have been investigated for the synthesis of ZnO nanorods, such as thermal evaporation [34], laser ablation [35], chemical vapor deposition [35], arc plasma reaction [37], and solution methods [38]. In this dissertation research,

the hydrothermal growth method was applied for the initial growth of the intrinsic ZnO nanorods. Compared to other ZnO nanorods synthesis methods, hydrothermal growth method was introduced into the ZnO nanorods growth in this dissertation because it strikes a good balance between fine crystal growth results and reasonable cost on the instrument, energy, and precursor [39]. Furthermore, hydrothermal growth method can be combined with other processes for various projects, like electrochemistry, ultrasound, microwave, optical radiation, to gain enhanced reaction kinetics or a potential path for new material synthesis [39]. Hydrothermal growth is commonly defined as a technique to synthesize crystallizing substances from aqueous solutions under high operating temperature and vapor pressure which are conditions where an otherwise insoluble precursor becomes soluble in the solution. However, the precursors used for ZnO nanorod growth are soluble in deionized (DI) water. For our ZnO nanorod hydrothermal growth experiments a lab oven with accurate temperature control was employed.

The Autoclave used as a sealed reaction chamber in hydrothermal growth technology is capable to tolerate high temperature and pressure. Corrosion resistance is another important feature factored into the material choice of an Autoclave to enable it to stand up to the chemical reaction inside the autoclave [40]. Because of this requirement, only corrosion resistant materials have been considered for the design of autoclaves, like stainless steel, iron, nickel, titanium, etc [40]. The requirements of an ideal hydrothermal autoclave are shown below [40]:

1) Inert to acids and oxidizing agent
2) Capable to tolerate high temperature and pressure with long duration time
3) Capable to seal the reaction solution at high temperature and pressure
4) Easy to operate (assemble and dissemble)

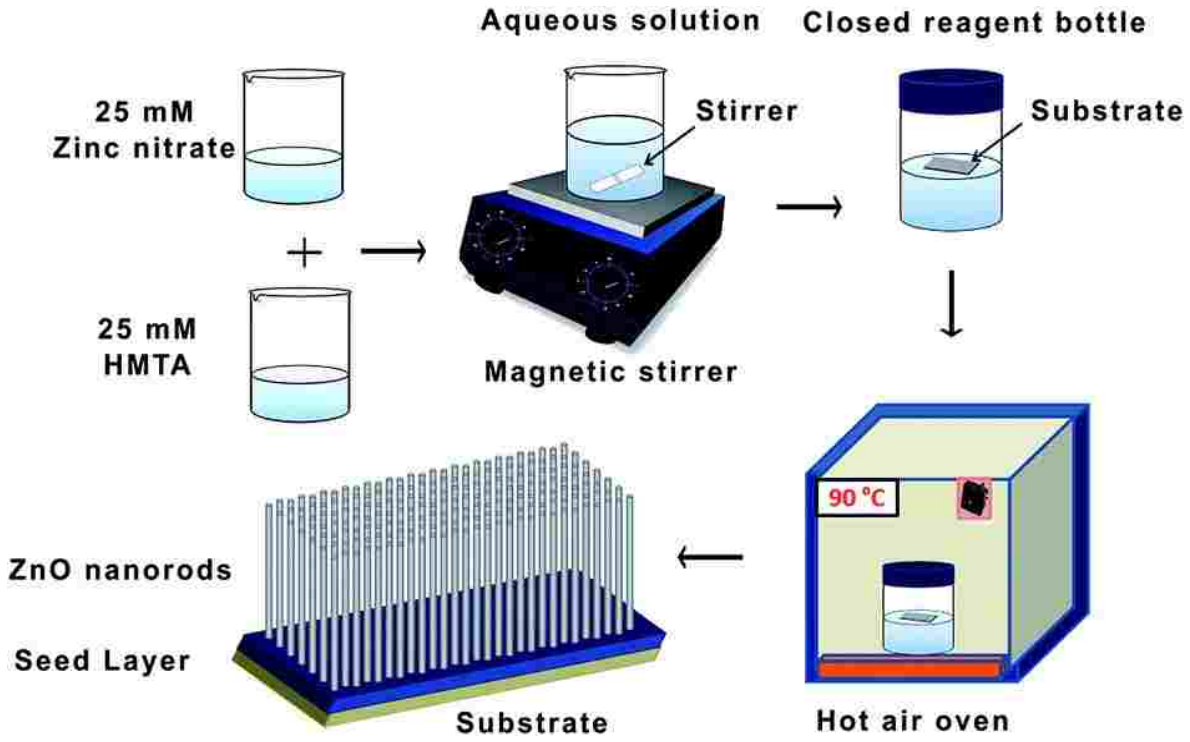


Figure 23. Schematic diagram of hydrothermal growth method for synthesis of ZnO nanorods detailing the individual process steps [40].

Figure 23 shows the individual process steps required for the synthesis of ZnO nanorods by hydrothermal growth which are summarized in the following [40].

1) Zinc nitrate hexahydrate and Hexamethylenetetramine (HMTA) are used as the precursors dissolved into DI water with same molar concentration of 25 mM.
2) Magnetic stirrer is introduced to completely dissolve the solutes into the solvent for the preparation of the reaction solution.
3) The substrate, typically Si covered with a fine grained polycrystalline ALD ZnO seed layer is sealed in the autoclave which contains the prepared reaction solution.
4) The reaction autoclave is heated up to 90℃ in the lab oven for 5 hours. During that time, single crystal ZnO nanorods grow by nucleation on the seed layer.

**2.3 Precision Ion Polishing System (PIPS)**

The Precision Ion Polishing System from Gatan Inc. was utilized to remove the top cover generated as a result of the subsequent ALD 3-D wrap-around layer coatings of the hydrothermal ZnO nanotubes. PIPS is known as the thinning polisher or ion milling used for thinning and polishing Transmission Electron Microscope (TEM) specimens on a nanometer scale by two Argon ion beams without much damage to the sample. Many methods and technologies have been investigated to polish the surface of samples for different applications, which includes mechanical polishing, colloidal silica polishing, and electro-polishing [41]. However, both mechanical polishing and colloidal silica polishing are handicapped by long operation time and the generation of surface damage on the sample [41]. Electro-polishing method imposes certain requirements on the prepared sample and the polishing chemical solution. The prepared sample needs to be electrochemically active, and the polishing chemical solution needs to correspond to the type material of the sample [41]. Furthermore, the polishing thickness of the sample cannot be precisely controlled in nanometer scale with these three methods.

By following the process sequence for novel nested co-axial ZnO nanorod/nanotube gas sensors described under Objective 2, all surfaces of the ZnO nanorods are getting completely covered with $Al_2O_3$ sacrificial layer and ZnO thin films due to the surface saturating property of ALD. As a result, the PIPS is needed to remove the ~40 nm surface top ALD cover films to expose the sacrificial layer without causing any damage to the ZnO nanorods. Further details are illustrated in Chapter 4 on Novel Nested ZnO Nanorod/Nanotube Gas Sensors. The PIPS used for this research objective is model 691 from Gatan Inc. as shown in Figure 24.

Figure 24. Photograph of Precision Ion Polishing System - Model 691 from Gatan Inc.

## 2.4 Gas Sensor Testing System

In this dissertation, the sensing performance of ALD synthesized novel ZnO nanostructure gas sensors was investigated by an in-house gas sensor testing system. The gas sensor testing system was custom designed and in-house built to investigate the sensing performance of ZnO nanostructure gas sensors for various target gas concentrations at different temperatures.

### 2.4.1 First Generation Prototype Gas Sensor Testing System

The custom designed home-built gas sensor testing system contains three basic features: a sealed reaction chamber, a resistance indicating circuit with a reference resistor, and a stable temperature control system. A laboratory glass flask, which was wrapped with a heating belt and

sealed with a rubber cap, was used as the sensor test chamber as shown in Figure 25 (left). The completed ZnO nanorod gas sensor was placed into the test chamber with the target gas to measure the sensing performance. Meanwhile, an RTD was also inserted into the test chamber for temperature detection to form a closed-loop temperature control system. The concentration of the ethanol test vapor was controlled by the injected volume of liquid ethanol using a syringe. Figure 25 (right) shows the connection method used to connect the resistance indicating circuit and the ZnO nanorod gas sensor. Two thin copper wires were connected to the surface of the ZnO sample with silver paste. Due to the high testing temperatures, the plastic cladding material of the copper wires had to be removed to prevent the melting plastic cladding from contaminating the target gas under test. The opposite ends of the two copper wires were connected to the resistance indicating circuit by two alligator clips.

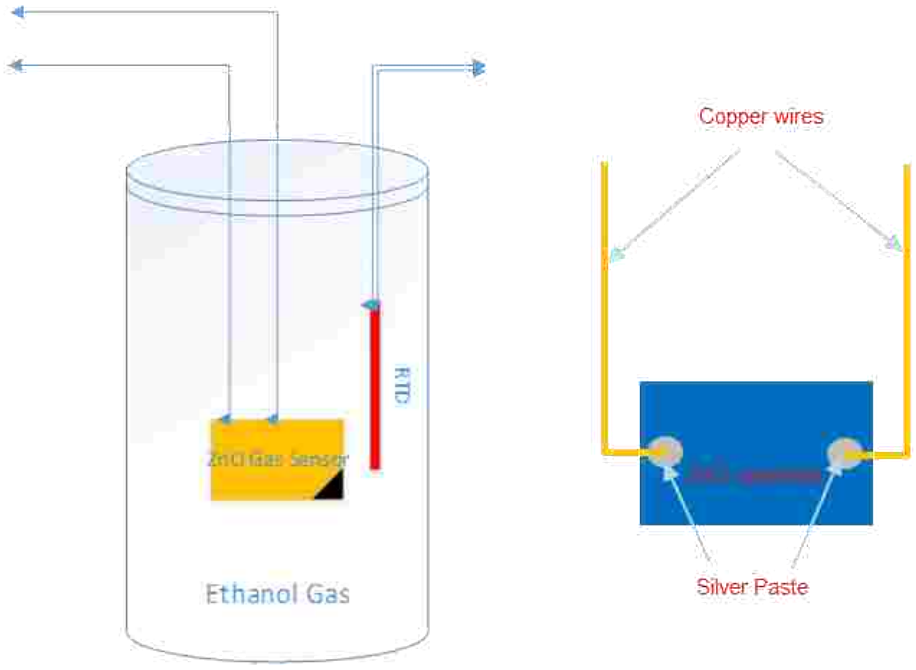


Figure 25. Schematic of first generation ZnO gas sensor testing chamber (left) and ZnO nanorod gas sensors connection (right).

Figure 26 (left) shows the layout of the resistance indicating circuit. The resistance indicating circuit is employed in the gas sensor testing system to monitor the resistance change of the ZnO nanorod gas sensor. With the help of the reference resistor installed in series in the circuit, the circuit current change and the voltage change on the ZnO sample can be accurately measured. Consequently, the resistance change of the ZnO nanorod gas sensors can be calculated based on Ohm's law as shown in Equations 34, 35, and 36 [42].

Voltage on ZnO sample:

$$V_{Sample} = V_{Source} - V_{Reference} \tag{34}$$

Current of the circuit:

$$I = \frac{V_{Reference}}{R_{Reference}} \tag{35}$$

Resistance of ZnO sample:

$$R_{sample} = \frac{V_{Sample}}{I} = \frac{V_{Source} - V_{Reference}}{V_{Reference}/R_{Reference}} \tag{36}$$

where $V_{Source}$ is the source voltage of the circuit, $V_{Reference}$ is the voltage on the reference resistor which can be indicated by the controller, $R_{Reference}$ is the resistance of the reference resistor.

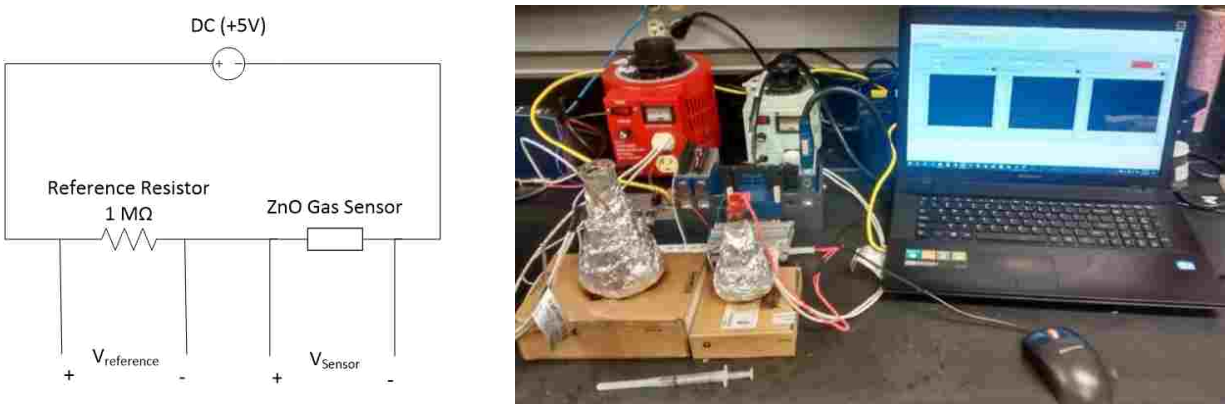


Figure 26. Schematic of ZnO gas sensor testing circuit (left) and inhouse-built sensing analysis system (right).

Figure 26 (right) shows a photograph of the custom designed in-house built sensing analysis system hardware setup. The sensing test chamber, the resistance indicating circuit, the real-time system controller, and the computer with software interface were all connected to monitor the resistance change of the ZnO nanostructure gas sensors during exposure to a preset ethanol vapor concentration under controlled temperature. The controller is based on the Compact Rio 9068 and several corresponding modules from National Instrument [42]. The schematic diagram of the Compact Rio 9068 contains 8 module communication slots shown in Figure 27 [43]. The modules NI 9217 and NI 9269 were installed in the Compact Rio 9068 for temperature control by collecting the temperature signal from the RTD and by providing power signal to the relay which connects with the heater [43]. Based on digital control theory, the temperature feedback signal is collected by the controller for the formation of a closed-loop temperature control system for the accurate and stable control of the temperature of the reaction chamber [43]. The third module, NI 9381, was used to connect the resistance indicating circuit by providing circuit power and collecting the voltage change on the reference resistor [43]. Therefore, the resistance change of ZnO nanostructure gas sensors can be calculated based on Equations 34 to 36.

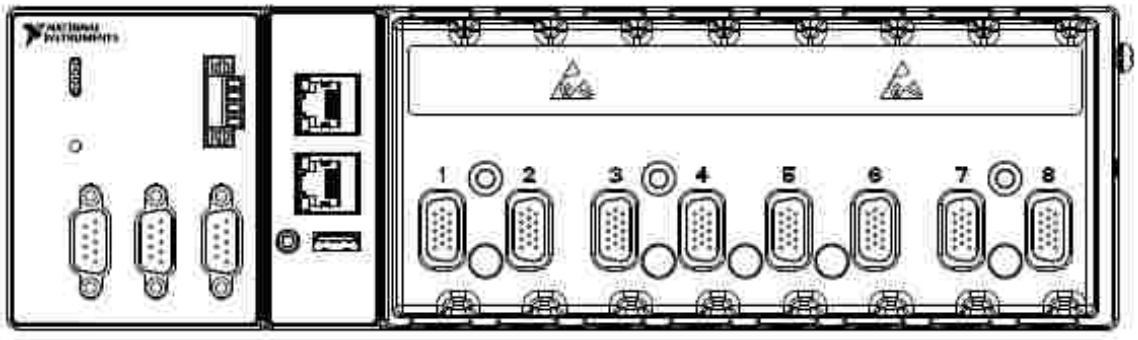


Figure 27. Compact Rio 9068 Horizontal Mounting [42].

Figure 28 shows the software interface programmed by LabView 2013 for the gas sensor testing system. The software interface was programmed to indicate and record the real-time values of the current of the circuit, the voltage on the ZnO sample, and the resistance change of the ZnO sample. As shown in Figure 28, the value changes of these three factors are monitored in the three flow charts. However, the physical value of the resistance indicating circuit that can be directly measured is the actual voltage on the reference resistor. Equations 34 to 36 are introduced into the calculation of the three factors based on the voltage change on the reference resistor. The interface also contains the value setup of the circuit power, the reference resistor, and the desired temperature setting. A closed-loop temperature control system was designed and built with feedback signal from an RTD. To accurately control the temperature, the Proportional Integral Derivative (PID) control theory was introduced into the design of the temperature control. The PID control parameter setting can be set and modified in the back panel.

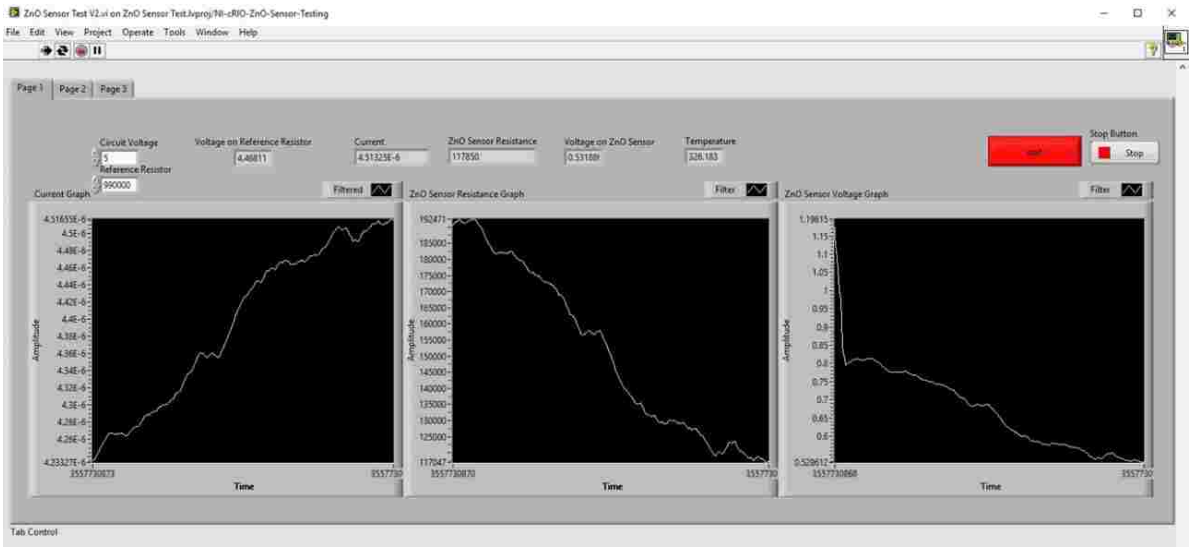


Figure 28. Display of Computer Monitor Interface of designed sensor testing software.

Figure 29 (left) and (right) demonstrates the sensing response data that are directly collected from the software interface. As introduced in Chapter 1.2.2 describing the gas sensing mechanism of ZnO nanostructure gas sensors, the resistance of the active ZnO sensor drops after exposure to reducing test gas. Therefore, the current of the resistance indicating circuit increases after exposure to a reducing test gas. When the reducing target gas was removed from the test chamber, the resistance increased back to the original value, which caused a decrease in the value of the circuit current as shown in Figure 29 (left) and (right). To calculate the sensing response of the novel nested ZnO nanostructure gas sensors, the following sensing response equation is applied as shown in Equation 37.

Sensing response as a factor of time [44]:

$$Response = \frac{R_{air} - R_{gas}}{R_{air}} \times 100\% \quad (37)$$

where $R_{air}$ is the resistance of ZnO nanostructure gas sensors in ambient air and $R_{gas}$ is the resistance of ZnO nanostructure gas sensors after having been exposed to the target gas.

Figure 29 (bottom) shows the sensing response change during the gas detection. The sensing response of ZnO nanostructure gas sensors increases after exposure to the target gas and reaches a response value characteristic for the target gas concentration and operating temperature. The sensing response resorted back to the initial value when the target gas was completely removed from the test chamber.

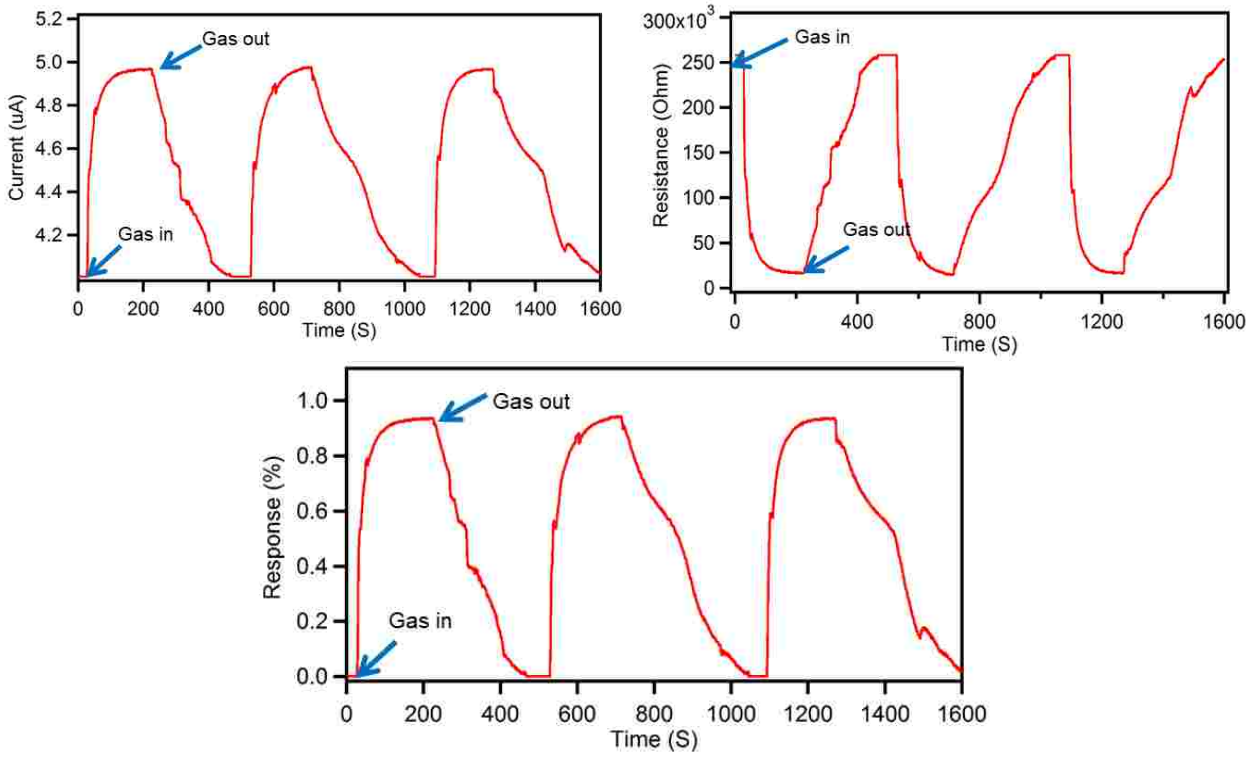


Figure 29. Examples of measured characteristic Current-Time plots (left), Resistance-Time plots (right), and Response-Time plots obtained from our experimental ZnO gas sensor device (bottom).

2.4.2 Second-generation gas sensor testing system

Based on the learning of the initial experiments, an upgraded gas sensor testing system was designed and built in-house for superior control of the concentration of the injected ethanol test vapor using two mass flow controllers (MFCs). Figure 30 (bottom) shows the photograph of the second-generation gas testing system hardware setup.

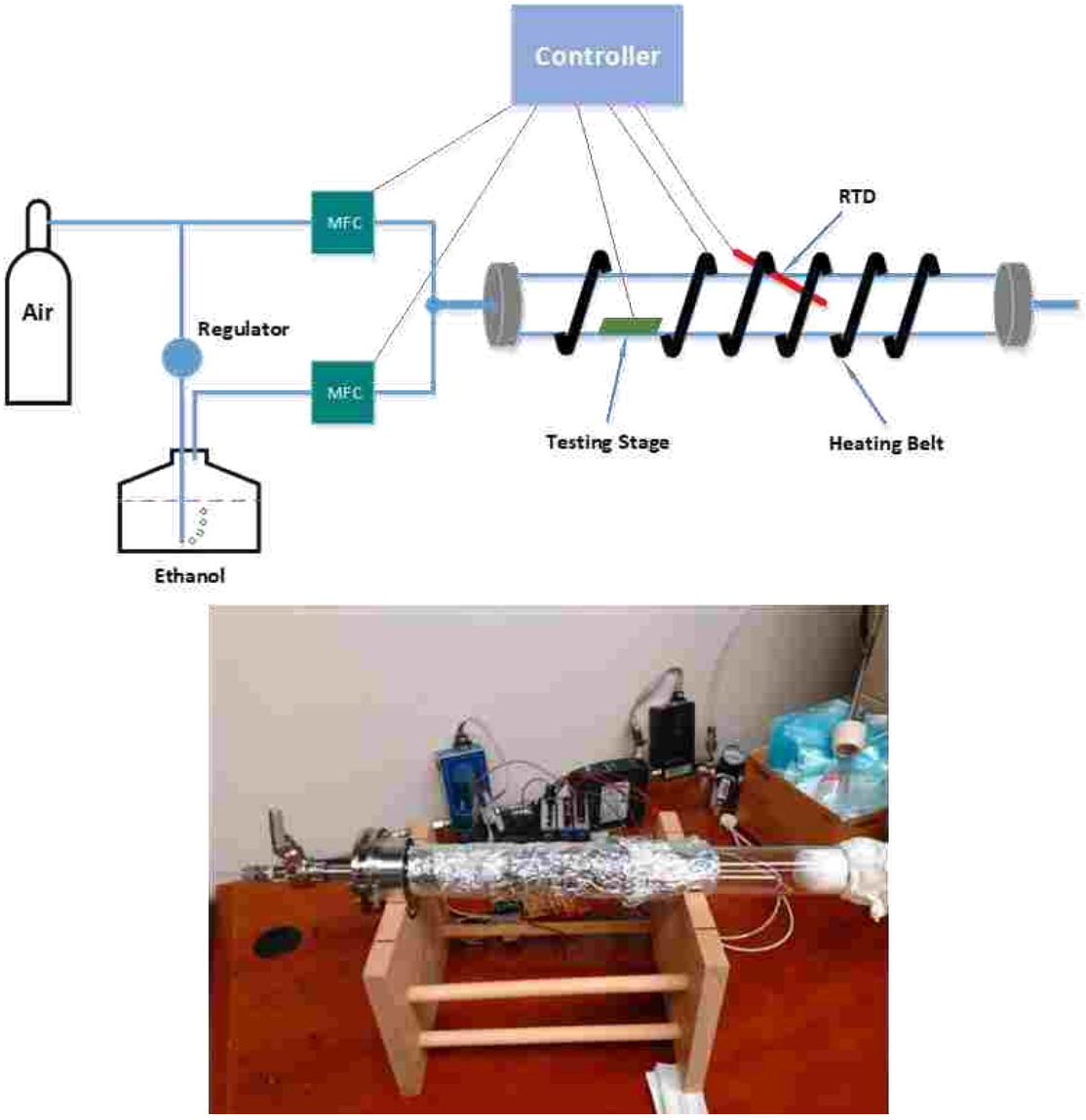


Figure 30. Schematic diagram of the second-generation gas sensor testing system (top) and photograph of the hardware setup (bottom).

Figure 30 (top) shows the schematic of the second-generation gas sensor testing system. Compared to the prototype gas sensor testing system, the upgrade of the system includes two novel features: a new test chamber and two MFCs. The previous test chamber consisting of a 500 mL

lab flask was replaced with a 2.4 L quartz furnace tube which enlarges the accuracy of the ethanol vapor concentration control based on the gas concentration Equation 38.

Gas concentration:

$$n = \frac{V_{gas}}{V_{Chamber}} \times 100\% \tag{38}$$

Where $V_{gas}$ is the standard volume of ideal gas at temperature T and pressure P, $V_{Chamber}$ is the volume of the reaction chamber.

Based on Equation 38, a larger volume of target gas needs to be injected into the larger test chamber compared to the small previous test flask to obtain the same desired target concentration. For example, to obtain 0.01% (100 ppm), the volume of the target gas should be 5 mL for 500 mL chamber and 24 mL for 2.4 L chamber. Therefore, the large test chamber is more convenient and straight forward for the controller to control the accuracy of the target gas concentration to be tested.

As shown in the schematic of the gas sensor testing system in Figure 30, two MFCs were used to control the input volume of ethanol vapor and air. Use of MFCs renders the target gas concentration controller more stable and accurate compared to operating with a syringe. The MFC used in the gas sensor testing is model GE50A from MKS with flow scale of 5 to 1000 $sccm$. Air is flowing through bubbler flask filled with liquid ethanol to form an ethanol vapor generator. The ethanol vapor mixed with air provides the input of the bottom MFC. The ethanol vapor concentration calculation is based on the Dubowski equation which is shown in Equation 39 [45].

$$\beta_{gas} = 0.04145 \times 10^{-3} \times \beta_{liquid} \times e^{(0.06583 \times t)} \tag{39}$$

where $\beta_{gas}$ is the mass concentration of ethanol in the gaseous phase in $mg/L$, $\beta_{liquid}$ is the mass concentration of ethanol in the liquid phase in $mg/L$, and $t$ is the temperature in ℃. For example, at 34 ℃, the mass concentration of ethanol is shown in Equation 40.

$$\beta_{gas} = \frac{\beta_{liquid}}{2573} \tag{40}$$

Therefore, the concentration of the ethanol vapor from the bottom MFC in the schematic of Figure 30 is calculated based on Equation 39. After mixing with the air from the output of the top MFC, the final concentration of the ethanol vapor in the test tube chamber is calculated according to Equation 41 with the unit conversion of $mg/L = ppm$.

Ethanol vapor concentration:

$$n_{ppm} = \frac{\beta_{gas} \times V_{gas}}{V_{gas} + V_{air}} = \beta_{gas} \left(\frac{V_{gas}}{V_{gas} + V_{air}}\right) \tag{41}$$

where $n_{ppm}$ is ethanol vapor concentration in $ppm$, the $\beta_{gas}$ is the mass concentration of ethanol in the gaseous phase calculated in Equation 39, $V_{gas}$ is the output volume of the ethanol vapor mixed gas from the bottom MFC in $sccm$, and $V_{air}$ is the output volume of the air gas from the top MFC in $sccm$.

# CHAPTER 3

## OBJECTIVE 1: IMPROVED ZNO NANOROD GAS SENSORS WITH ALD AZO COATINGS

This chapter introduces the initial approach to improve the sensing performance of ZnO nanorod gas sensors of ethanol vapor concentrations by depositing Aluminum doped ZnO thin films by Atomic Layer Deposition technology. This section discusses the synthesis method, the enhancing mechanism, and the sensing performance results to ethanol vapor concentration detection. Gas sensors based on ZnO nanorods have been widely investigated due to their electrochemical stability, nontoxicity, high surface-to-volume ratios, suitable doping. Numerous methods have been tried to enhance and boost the sensing performance of ZnO nanorod gas sensors. The majority of methods trying to achieve a boost of the performance center around introduce thin film coatings, like Pd [22], InSb [23], Ni [24], etc. However, the objective in this dissertation research was to investigate Aluminum doped ZnO thin films deposited by ALD to boost the sensing performance of ZnO nanorod gas sensors. Aluminum doping was primarily selected because of such desirable features as good electrical conductivity, non-toxicity, low material cost, and good thermal stability [46, 47, 48].

In this project, intrinsic single crystal ZnO nanorods were initially synthesized by the hydrothermal method with a fine grained polycrystalline ALD ZnO seed layer on Si. Al doped ZnO thin films with 2% Al dopant were coated in a 3-D wrap-around manner on the surface of ZnO nanorods by ALD to improve the sensing performance of ZnO nanorod gas sensors. Due to the limited available spacing between each ZnO nanorod determined by the density of ZnO

nanorods per cm2 grown by hydrothermal method, the thickness of AZO coating was limited to a maximum of 25 nm. Therefore, ALD has been conceived as the only technology capable to realize the required unique conformal 3-D wrap-around AZO coating with precisely controlled deposition thickness and composition. The custom designed and in-house built gas sensor testing system was utilized to investigate and benchmark the sensing response, response time, and recovery time of ZnO nanorod gas sensors before and after being coated with ALD AZO thin films.

## 3.1 Synthesis Method

### 3.1.1 Synthesis Procedure

Based on the requirements of this project objective, there are a total of four processes to fabricate ZnO nanorod gas sensors: initial growth of ZnO seed layers, subsequent growth of ZnO nanorods, followed by AZO deposition, plus annealing and Al out diffusion to form uniform AZO layers.

*ZnO Seed Layer Synthesis (ALD)*

Random polycrystalline ZnO thin films with very fine grain structure used as seed layer for ZnO nanorods growth were deposited on Si substrate by ALD at 200℃ operating temperature. Diethylzinc (DEZ, $Zn(C_2H_5)_2$) was used as the ALD precursor of Zn and DI water vapor was used as precursor two and oxidation agent. Both ALD precursors were alternating introduced into the chamber by $N_2$ carrier gas flow when the pneumatic ALD valves opened to release a puff of vapors into the reaction chamber. The thickness of the ALD synthesized ZnO seed layer was controlled to 30 nm. Following the ALD deposition, the ZnO seed layer samples were evenly split into two equal pieces and received labelling of non-annealed ZnO seed layer and annealed ZnO seed layer. The intent was to investigate if the seed layer annealing benefits the hydrothermal growth by

driving out any remaining solvent from the seed film. To this end, the annealed ZnO seed layer samples were annealed in ambient air in the furnace for 30 minutes at 350℃.

*Hydrothermal Growth of ZnO nanorods (Chemical Reaction)*

For comparison intrinsic single crystal ZnO nanorods were grown by the hydrothermal method on both non-annealed and annealed ZnO seed layers synthesized by ALD. The reaction solution was prepared with 0.03756 g zinc nitrate hexahydrate ($Zn(NO_3)6H_2O$) and 0.0176 g hexamethylenetetramine ($(CH_2)_6N_4$) dissolved in DI water [49]. A comparison was made based on the ZnO nanorods synthesized with different molar concentrations of solute by changing the volume of solvent. Then the prepared ZnO seed layers were sealed in the autoclave and kept in the lab oven at 75℃ for 16 hours [49]. The experimental hydrothermal growth conditions for ZnO nanorods are shown in Table VI.

TABLE VI

ZnO Nanorod Hydrothermal Growth Conditions.

| Precursor | Temperature and Time | ALD ZnO Nanocrystalline Seed Layer | Solute Concentration |
|---|---|---|---|
| Zinc Nitrate Hexahydrate ($Zn(NO_3)6H_2O$) Hexamethylenetetramine ($(CH_2)_6N_4$) | 75℃ for 16 hours | Not Annealed | 25 mM, 20.8 mM, 17.8 mM (50 mL, 60 mL, 70 mL DI water, respectively) |
| | | Annealed at 350℃ for 30 mins | |

The chemical reaction equations during the ZnO hydrothermal growth are show in Equations 42 to 45 [50].

Decomposition Reaction:

$$(CH_2)_6N_4 + 6H_2O \leftrightarrow 4NH_3 + 6HCHO \quad (42)$$

Hydroxyl Supply Reaction:

$$NH_3 + H_2O \leftrightarrow NH_4^+ + OH^- \quad (43)$$

Supersaturation Reaction:

$$Zn^{2+} + 2OH^- \leftrightarrow Zn(OH)_2 \quad (44)$$

ZnO Nanorod Growth Reaction:

$$Zn(OH)_2 \leftrightarrow ZnO + H_2O \quad (45)$$

It is noteworthy that the ZnO nanorods nucleating on the fine-grained seed layers in the sealed hydrothermal autoclave grow in general as single crystal nanorods displaying a strictly crystallographic hexagonal cross-section, which provides the tell-tale prove of single crystallinity.

*AZO Deposition (ALD)*

ALD was introduced to deposit AZO thin film coatings of myriad the surface of synthesized ZnO nanorods in the previous hydrothermal process step. Diethylzinc, trimethylaluminum (TMA, $Al_2(CH_3)_6$), and DI water were used as the ALD precursors for the deposition of AZO. The chemical reaction formulas are based on Equations 27 to 33 in Chapter 2. The selected percentage of Al dopant was 2% and the coating film thickness was around 25 nm. To illustrate the details of the processes, Figure 31 shows a schematic top-down and also a cross-sectional view of a single ZnO nanorod which received alternate ALD nanolaminate coatings of AZO followed by a furnace annealing. The recipe of 2% ALD AZO is composed of nanolaminates consisting of several single cycles of 56 monolayers of ZnO thin films and 1 layer of $Al_2O_3$ thin

film deposition followed with another 56 layers of ZnO thin films. This specific nanolaminate sequence was designed to generate 2% Al doping of the ZnO following furnace annealing and Al out-diffusion. After annealing, the final thickness of the uniform AZO coating is around 25 nm. Based on the synthesis method of ZnO nanorods, the average available spacing between individual nanorods is around 100 nm. Thicker AZO thin film coatings might cause nanorods to completely fill all the available spacing in between nanorods and to stick to each other which will impede the sensing performance improvement of AZO coating. In our case of hydrothermal growth of dense ZnO nanorods the available spacing between individual nanorods left only sufficient room for one single cycle of 2% ALD coatings deposition with 56 layers of ZnO thin films and 1 layer of $Al_2O_3$ layer followed with 56 layers of ZnO thin films.

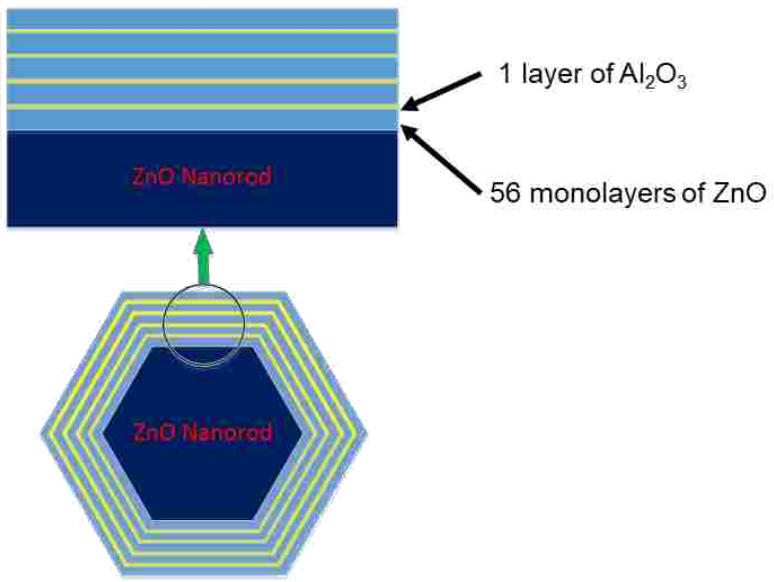


Figure 31. Top-down and cross-sectional view of schematic diagram of one single crystal ZnO nanorod having received alternate ALD nanolaminate coatings of 56 layers of ZnO followed by 1 layer of $Al_2O_3$ which was followed by a furnace annealing step to generate AZO by Al out-diffusion and Al doping of the ZnO.

*AZO Annealing*

Following the previous process steps, the obtained coating can only be characterized as an ALD nanolaminate composite composed of distinct layers of separate ZnO and $Al_2O_3$ thin films. To achieve aluminum doped ZnO coatings, ZnO nanorod samples had to be annealed at 300℃ for 30 minutes to diffuse aluminum atoms uniformly from the $Al_2O_3$ diffusion source layer to the surrounding ZnO layers and to electrically activate the Al doping. This last annealing and diffusion are the crucial process to ultimately produce 2% aluminum doped ZnO (AZO) coatings synthesized on the surface of the myriad ZnO nanorods on each sample.

### 3.1.2 Physical Characterization

As part of the physical characterization work for this part of the research work, X-ray powder diffraction (XRD) was performed to determine the crystal structure of the ZnO nanorod gas sensors before and after ALD AZO coating. Field Emission Scanning Electron Microscope (FE-SEM) was employed to analyze the morphology of the synthesized ZnO nanorod gas sensors, while the elemental composition of AZO thin films was analyzed by energy dispersive X-ray spectroscopy (EDS).

*XRD Analysis*

Figure 32 shows the XRD results of ZnO nanorods before and after coating with ALD AZO thin films and subsequent furnace annealing. The three XRD peaks at 31.92°, 34.64°, and 36.44° have been indexed to the (100), (002), and (101) directions of the ZnO hexagonal wurtzite structure [51]. Comparing the two results reveals, there is an increase in the intensities for the three peaks on the result of ZnO nanorods with AZO coatings, which is attributed to the subsequent furnace annealing process to actually create an electrically activated AZO coating. Following the furnace

annealing, to out-diffuse the Al dopants uniformly from the $Al_2O_3$ source, the ZnO nanorods orientation remained unchanged and merely reproduced all three indexed peaks of the intrinsic nanostructure of the hydrothermal ZnO nanorods [52]. However, there is a significantly increased intensity for the (002) orientation and for the (100) peak of the ZnO nanorods after coating with ALD AZO thin films and subsequent annealing, which establishes preferred crystal growth along the c-axis orientation of the ZnO hexagonal wurtzite structure. The furnace annealing procedure at higher annealing temperature of 300℃ causes solid-state growth of the core ZnO nanorod and also grain growth of the ALD polycrystalline ZnO coating along the preferred c-axis orientation [53].

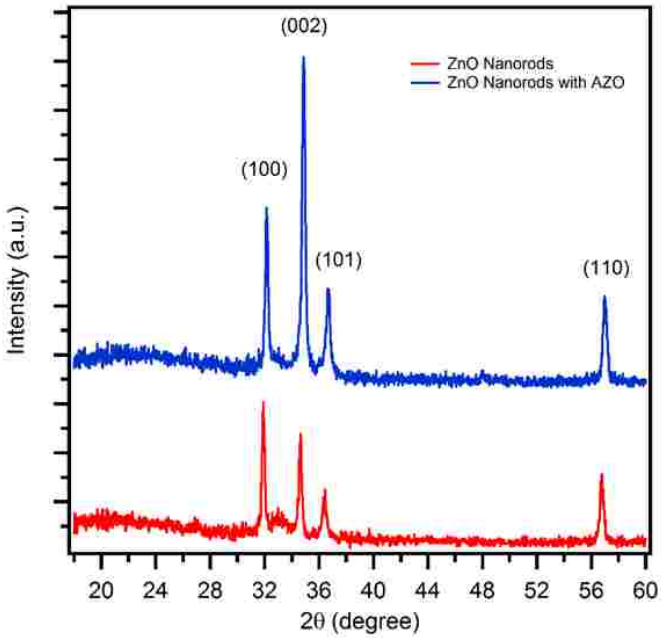


Figure 32. XRD results of undoped intrinsic ZnO nanorods compared with intrinsic ZnO nanorods with a conformal AZO wrap-round coating, which results in a significant increase of the (002) peak establishing preferred growth along the c-axis orientation of the hexagonal wurtzite structure.

*FE-SEM Analysis*

Figure 33 shows the FE-SEM results of the initial ZnO nanorods synthesized by hydrothermal growth on polycrystalline ZnO seed layers before (left) and after (right) coating with an ALD 3-D wrap-around coating with AZO thin films. The strictly crystallographic hexagonal shape of the original intrinsic nanorods grown by hydrothermal method indicates single crystal ZnO nanorods as shown in Figure 33 (left). The granular surface of the ZnO nanorods shown in the right two micrographs of Figure 33 demonstrate the subsequent coating with ALD polycrystalline AZO thin films surrounding all hydrothermal ZnO nanorods.

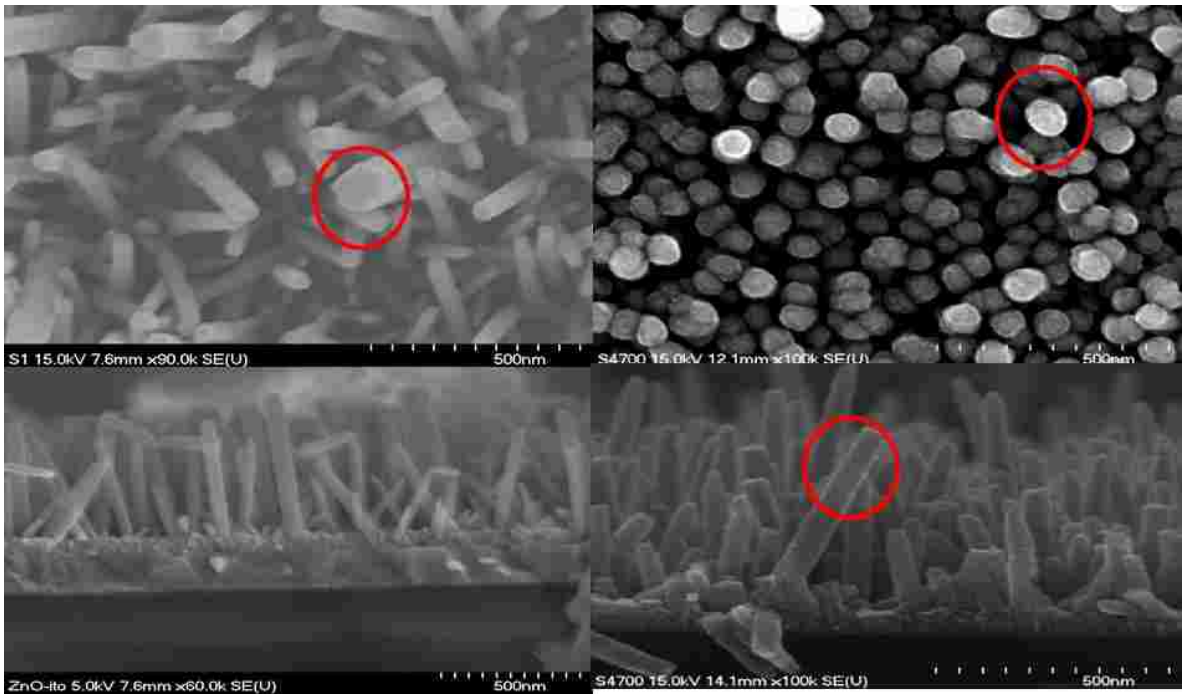


Figure 33. FE-SEM micrographs of original intrinsic ZnO nanorods grown by the hydrothermal method before (two micrographs on the left) and after being coated with ALD AZO films (two micrographs on the right). The SEM cross-sections reveal an average height of the nanorods of about ~600 nm.

*Energy Dispersive X-ray Spectroscopy EDS*

The EDS result shown in Table VII reveal the elemental composition of the ALD AZO thin films deposited by ALD. The Al dopant percentage testing was performed on the AZO thin films deposited on additional Si test wafer samples which were placed in the ALD reaction chamber during the regular coating process of AZO thin films on the surface of the ZnO nanorod gas sensors. Based on the EDS result, the percentage of Al atoms achieved was 2.57%, which is very close to the expected target percentage of about 2% for our experimental design of the solid Al diffusion source in the form of $Al_2O_3$.

TABLE VII

EDS Result of 2% Al Doped ZnO Thin Film.

| Element | Weight% | Weight% | Norm. Wt% | Norm. Wt% Err | Atom% | Atom% Err |
|---|---|---|---|---|---|---|
| O | 20.06 | +/- 0.35 | 20.06 | +/- 0.35 | 49.86 | +/- 0.87 |
| Al | 1.74 | +/- 0.14 | 1.74 | +/- 0.14 | 2.57 | +/- 0.20 |
| Zn | 78.20 | +/- 0.79 | 78.20 | +/- 0.79 | 47.57 | +/- 0.48 |
| Total | 100.00 | | 100.00 | | 100.00 | |

*Electrical Resistance*

The conductivity of the ZnO nanorod gas sensor was also improved by ALD AZO coatings due to the high conductivity characteristic of Al dopant. To establish the optimum conditions for the fabrication of ZnO nanorod sensors a series of experiments were run, where many parameters of the hydrothermal growth conditions were varied. Table VIII shows the comparison between

ZnO nanorods before and after coating with AZO thin films, synthesized on non-annealed and annealed seed layers, and synthesized in the three tested hydrothermal growth reaction solutions with different molar concentrations of solute. Based on Table VIII, hydrothermal ZnO nanorods grown on annealed ZnO seed layers by exhibit a better electrical conductivity compared to ZnO nanorods synthesized on non-annealed seed layers due to the increased ZnO grain size after annealing and complete solvent removal. ZnO nanorods synthesized in the reaction solution with 20.8 mM molar concentration of the solutes possess the lowest resistance compared to the other two solute concentrations. The conductivity comparison between the ZnO nanorods before and after coating with ALD AZO thin films shows an improvement in the electrical conductivity of ZnO nanorods by coating the surface with AZO thin films due to the Al doping effect.

TABLE VIII

Resistance Comparison.

| | 25 mM (50 mL) | | 20.8 mM (60 mL) | | 17.8 mM (70 mL) | |
|---|---|---|---|---|---|---|
| | No Anneal | Anneal | No Anneal | Anneal | No Anneal | Anneal |
| Before | 390 KΩ | 210 KΩ | 300 KΩ | 190 KΩ | 310 KΩ | 240 KΩ |
| After | 380 KΩ | 196 KΩ | 276 KΩ | 170 KΩ | 301 KΩ | 210 KΩ |

### 3.2 Mechanism of ZnO Sensor Performance Enhancement

This section explains the enhancing mechanism of the sensing performance enhancement of ZnO nanorod gas sensors as a result of introducing ALD AZO coatings by ALD technology. Al dopants introduce more oxygen vacancies and electrons to the ZnO nanorod gas sensors for the

detection of ethanol vapor after coating ZnO nanorods with AZO thin films. Initially the AZO fabrication process by ALD coating forms a delta doping source in the form of alternating nanolaminates of thin $Al_2O_3$ layer, which act as solid diffusion source for Al doping. During the annealing process after introducing ALD AZO thin films deposition, interstitial $Al_i$ (isolated interstitial Al) pushed away Zn ion and changed to $Al^+$ (in the 1+ charge state) in the substitutional position, which leads to an increase on the density of $Zn_i$ (isolated interstitial Zn) in the 2+ charge state ($Zn^{2+}$) [54]. The substitutional $Al^+$ (named as $Al_{Zn}$) and the interstitial $Zn^{2+}$ (named as $Zn_i$) are considered as shallow donors and formed as $Al_{Zn}$-$Zn_i$ complex [54]. Based on the low formation energy of $Al_{Zn}$ for Fermi levels close to conduction band, it was assumed that the interstitial Al contributed one electron to the majority carriers of ZnO [54]. Therefore, there would be more oxygen molecules adsorbed to the surface of ZnO nanorods with AZO coatings to form oxygen negative ions, which leads to an increase on the reaction sites.

As shown in Figure 34, the additional oxygen vacancies and electrons generate more reaction sites (oxygen negative ions) during oxidation reaction based on Equations 5 to 7. Therefore, there will be more target gas molecules that are able to react with the added oxygen negative ions. Furthermore, through the surface oxidation process more electrons are released back to the conduction band that causes an increase in the majority charge carriers and a resistance drop of the ZnO nanorods. According to Equations 19 and 20, the depletion layer and the potential barrier of AZO nanoparticle become thinner compared to these two features of ZnO nanoparticle as shown in Figure 34. To sum up, the sensing response of ZnO nanorod gas sensors increase with increased resistance change caused by the introduction of Al dopant.

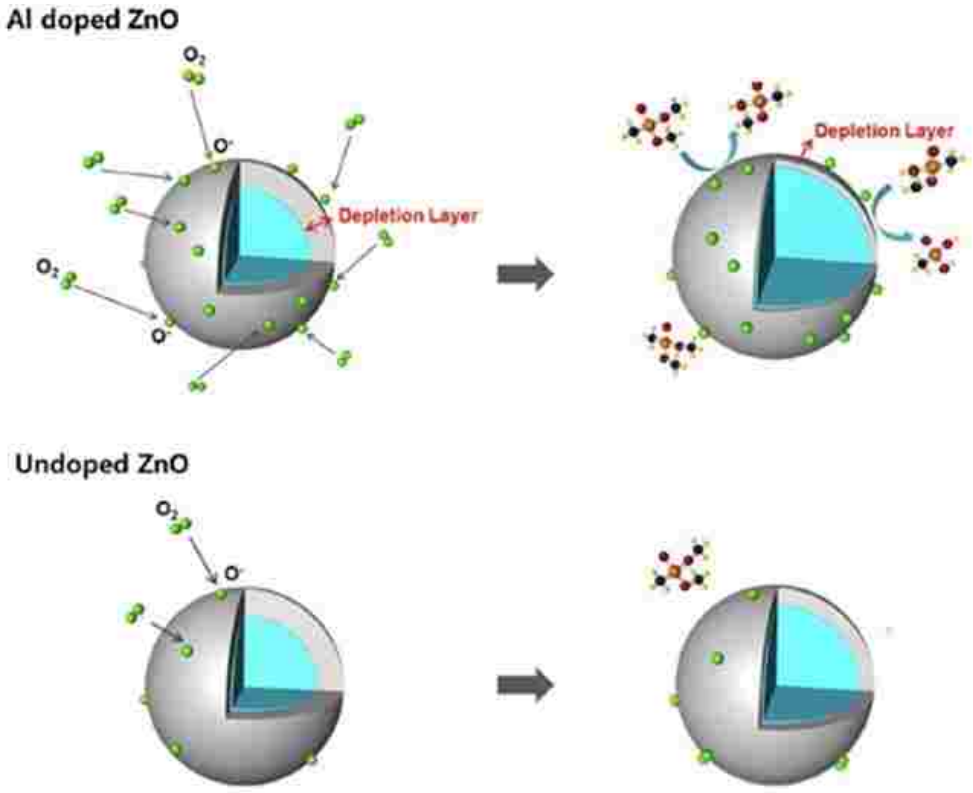


Figure 34. Schematic depiction of the changes occurring in the depletion layer width of an undoped ZnO nanoparticle (shown in bottom figure) versus an Aluminum doped ZnO nanoparticle (shown in top figure) after exposure to a reducing gas [55].

## 3.3 Gas Concentration Detection

### 3.3.1 ZnO Nanorod Gas Sensor Selection

Using the custom designed in-house built gas sensor testing system a careful analysis was performed of the sensing performance for concentration detection of ethanol vapors of ZnO nanorod gas sensors with and without ALD AZO coatings. As illustrated in Chapter 1, the crucial parameters to evaluate the sensing performance of gas sensors include sensitivity, selectivity, stability, response time, recovery time etc. In this section, the sensing response, response time, and

recovery time of ZnO nanorod gas sensors before and after introducing ALD AZO coatings were analyzed.

Based on the hydrothermal growth procedure described in the previous sections, the ALD ZnO seed layer sample was evenly split into two parts, one remained as prepared and the other one was furnace annealed in air. Also, several series of experiments were performed to optimize the ZnO nanorod hydrothermal growth to achieve the highest sensing response through modifying the concentration of the solute dissolved in the reaction solution modified by changing the volumes of solvent (DI water). Figure 35 shows the ethanol sensing response (calculated by Equation 37) of ZnO nanorod gas sensors synthesized under different hydrothermal growth conditions by varying solute concentration and by modifying ZnO seed layer post treatment.

In Figure 35, the label of annealed 25 mM ZnO nanorod gas sensors signifies the ZnO nanorod sensor devices was grown on an annealed ALD ZnO seed layer in the hydrothermal growth reaction solution with solute concentration of 25 mM. Based on the comparison between Figure 35 (a), (c), (e) and Figure 35 (b), (d), (f), the sensing responses of ZnO nanorod gas sensors synthesized on annealed ALD seed layers present better sensing result than the responses of ZnO nanorods grown on non-annealed seed layer. Furthermore, the response time and recovery time of ZnO nanorod gas sensors are also improved with the use of annealed seed layers.

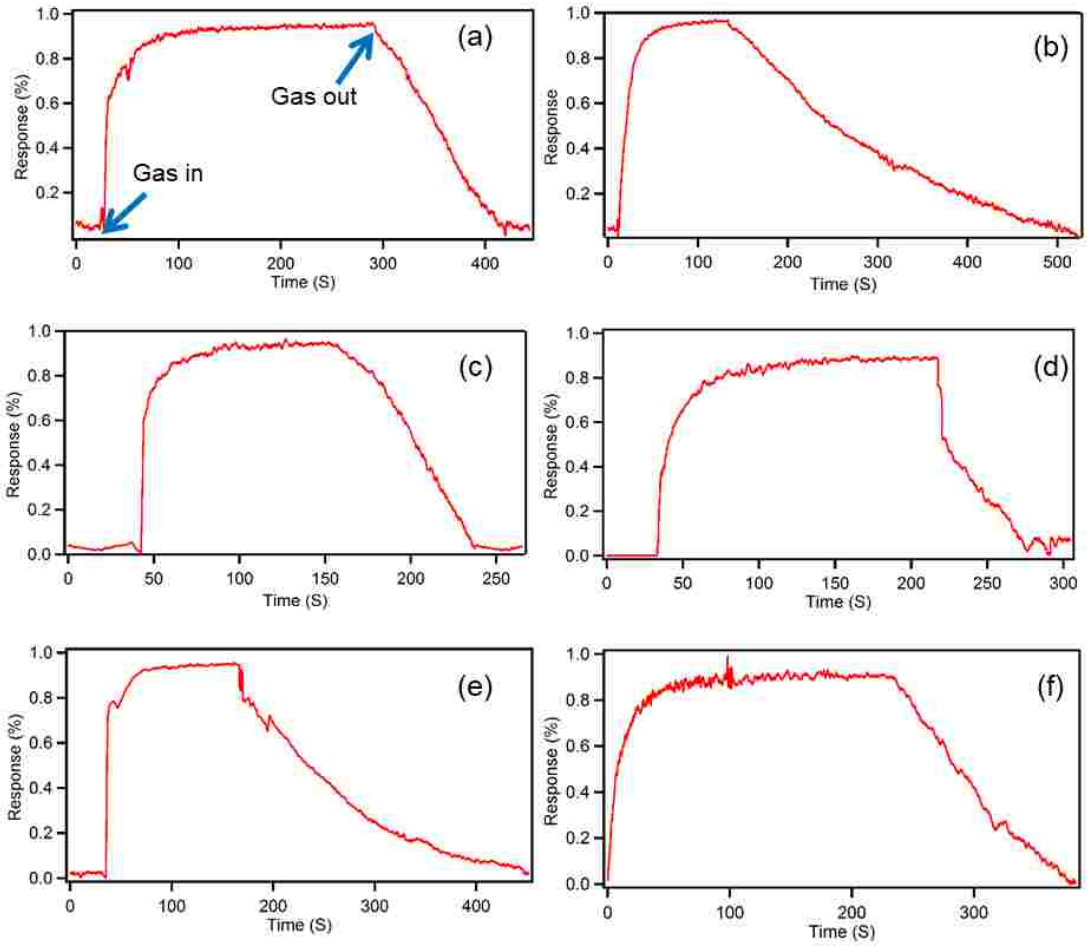


Figure 35. Comparison of Sensing response of ZnO nanorod gas sensors grown on annealed seed layers and hydrothermal solute 25 mM (a), 20.8 mM (c), 17.8 mM (e) versus grown on non-annealed seed layers with 25 mM (b), 20.8 mM (d), 17.8 mM (f) with 800 ppm ethanol vapor at 320℃.

After furnace annealing the ZnO seed layer, the grain size of random polycrystalline ZnO grains increased at the higher temperature, which negatively affects the surface-to-volume ratio of the sensing layer (ZnO nanorods). According to hydrothermal growth theory, ZnO nanorod nucleate and grow on top of ZnO seed grains which serve as nucleation catalyst. Therefore, the diameter of the ZnO nanorods increase with enlarged grain sizes of the ZnO seed layer, which can

cause a decrease on the surface-to-volume ratio. However, ZnO nanorods synthesized on annealed seed layers, which have high crystalline nanostructures, are less affected by this drawback. Based on the measured sensing responses shown in Figure 35, the better sensing performance exhibited by ZnO nanorods grown on annealed seed layers can be attributed to the observation that annealed and enlarged seed grains are more efficient for nucleating ZnO nanorod growth compared to the smaller grains on non-annealed seed layers.

Evaluation of the experimental data listed in Table VIII and Figure 35, strongly suggested to select ZnO nanorods grown under optimum conditions on annealed seed layers by hydrothermal method in the reaction solution with 20.8 mM molar concentration of each solute for the sensing enhancement analysis of ZnO nanorod gas sensor before and after coating with ALD AZO thin films.

### 3.3.2 Analysis of Sensing Response as a function of Various Temperatures

In this section, the sensing responses of ZnO nanorod gas sensors to ethanol vapor with saturation level concentration at different temperatures were measured with and without ALD AZO thin film coating to investigate the relationship between temperature and the sensing response of ZnO nanorod gas sensors. The gas sensor testing temperatures include 25℃, 37℃, 100℃, 150℃, 200℃, 250℃, 320℃, and 340℃ as shown in Figure 36. Both sensing responses of ZnO nanorods with and without coating with ALD AZO thin films demonstrate that the sensing response increases with rising temperature until a maximum value at 320℃ is reached, which is considered the optimum working temperature of ZnO nanorod gas sensors. During the reduction reaction described in Equation 8, electrons are released back to the conduction band by the reaction between the target gas molecules and oxygen negative ions immediately after exposure to the reducing gas

(ethanol vapor). After reaching the optimum operating temperature, the sensing response decreases for higher temperatures beyond the peak, which is attributed to the increased number of electrons adsorbed from conduction band at the surface of ZnO nanorods at these higher temperatures. This is caused by the fact that the oxidation (desorption) rate is faster than the reduction (chemisorption) rate according to Equations 5, 6, and 7. Both oxidation reactions and reduction reactions occur during the gas detection process after exposure to ethanol vapors. At low temperatures, the oxidation reaction rate is slower than the reduction speed, which means the oxidation reaction is remaining at the stage of in Equations 5 and 6 with small amount electrons adsorbed to the surface to form oxygen negative ions. However, at higher temperatures, the oxidation reaction reaches the level of Equation 7 with more electrons adsorbed from the conduction band to the surface, which leads to a decrease in the majority carrier density and an increase in depletion layer width and the potential barrier. Therefore, the sensing response decreases at these higher temperatures beyond the optimum working temperature.

The bottom part of Figure 36 shows a comparison between the sensing response of ZnO nanorod gas sensors to saturation level concentration ethanol vapors as a function of temperature before (blue line in the figure) and after (red line in the figure) introduction of ALD AZO coatings. The sensing response of ZnO nanorod gas sensors without AZO coatings to ethanol vapor at low temperature is week and unstable as demonstrated in Figure 36 (left). After coating with ALD AZO thin films, the ZnO nanorod gas sensors exhibit a significantly higher sensing response compared with the original non-coated intrinsic ZnO nanorod samples. This benchmark test result comparison shows good agreement with the theory that AZO coatings provide extra oxygen vacancies and additional electrons which serve to improve the sensing response of ZnO nanorods.

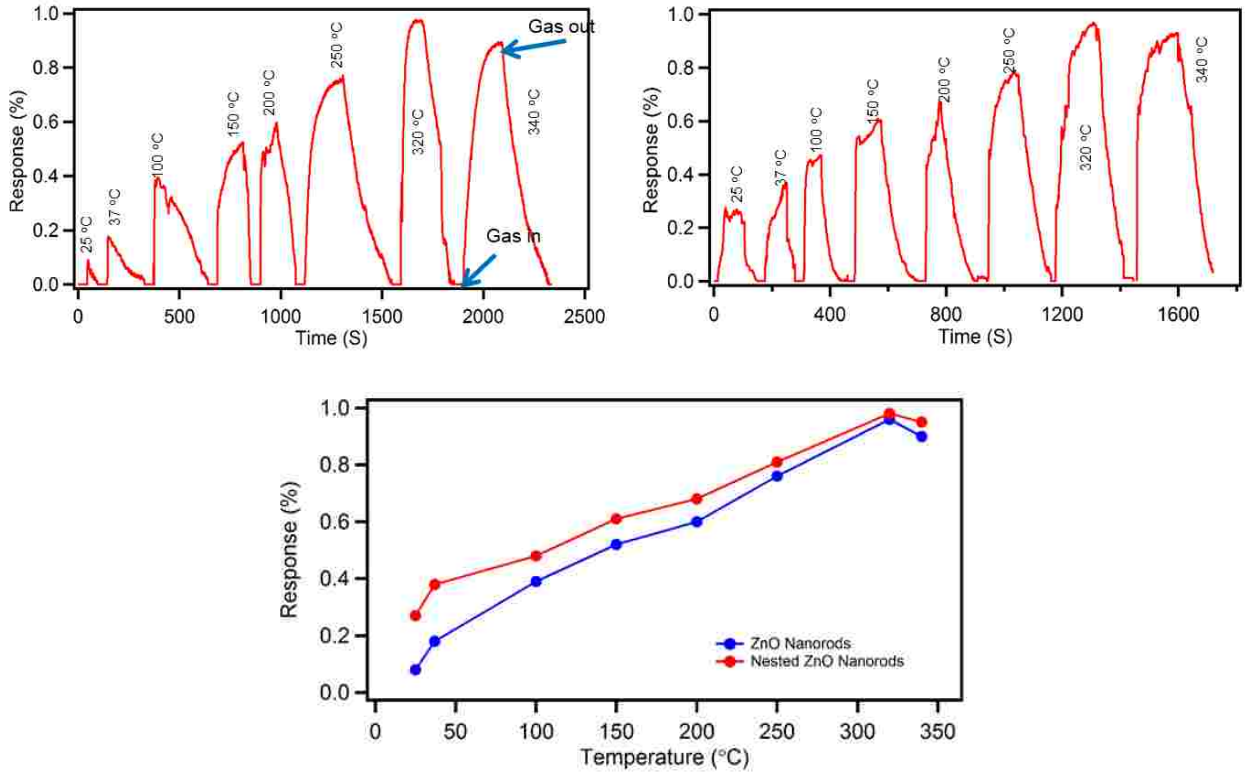


Figure 36. Sensing responses of ZnO nanorods to ethanol vapor with saturation level concentration at different temperatures without (top left) and with receiving ALD AZO layer coating (top right). (Bottom figure) Comparison of Sensing Response as a function of temperature.

Furthermore, the sensing response of ZnO nanorod gas sensors gains a significant improvement at lower detecting temperatures from the presence of AZO coatings. At 37℃, the enhancement gain reaches up to 100% based on Equation 46, as shown in Figure 37. However, the enhancement gain of the sensing response of ZnO nanorod gas sensors with AZO coatings drops as a function of further increasing operating temperature, which is attributed to the faster oxidation reaction rate at high temperature compared to the reduction reaction rate.

Gained Enhancement Equation:

$$Enhancement = \frac{\beta_{ehanced} - \beta_{original}}{\beta_{original}} \times 100\% \quad (46)$$

where $\beta_{original}$ is the sensing response of the ZnO nanorod gas sensors without AZO coating, $\beta_{ehanced}$ is the sensing response of ZnO nanorod gas sensors with AZO coatings.

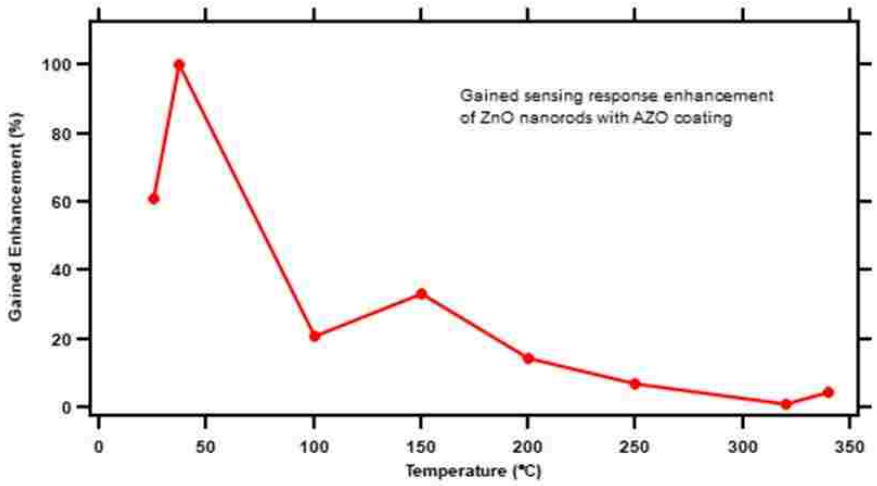


Figure 37. Enhancement gain on the sensing response of ZnO nanorod gas sensors with AZO wrap-around coatings.

3.3.3 Analysis of Sensing Response as a Function of various Ethanol Vapor Concentrations

In this section, the sensing response of ZnO nanorod gas sensors was investigated as a function of different concentrations of ethanol vapor at 320℃ optimum working temperature before and after coating with ALD AZO thin films. These measurements serve to determine the relationship between the sensing response and the target gas concentration and the saturation level of the detecting concentration. As shown in Figure 38 (top left) and (top right), the sensing response of both ZnO nanorods before and after coating with ALD AZO thin films increases with rising concentration of ethanol vapor and reaches saturation when the concentration is increased to 800 ppm and 1000 ppm, respectively. The saturation level is limited by the number of available reaction sites on the surface of ZnO nanorod gas sensors, which are created during the oxidation

reaction. Therefore, as explained in the previous section on the enhancing mechanism, the increased saturation level of the ZnO nanorod gas sensors after the introduction of AZO coatings is attributed to the extra oxygen vacancies and additional electrons contributed by the Al dopants, which can generate more reaction sites.

Figure 38 (bottom) shows the sensing response comparison between ZnO nanorods before and after being coated with ALD AZO. This comparison demonstrates the improvement in the sensing response of ZnO nanorod gas sensors to ethanol vapor with the introduction of AZO coatings, especially at lower concentration.

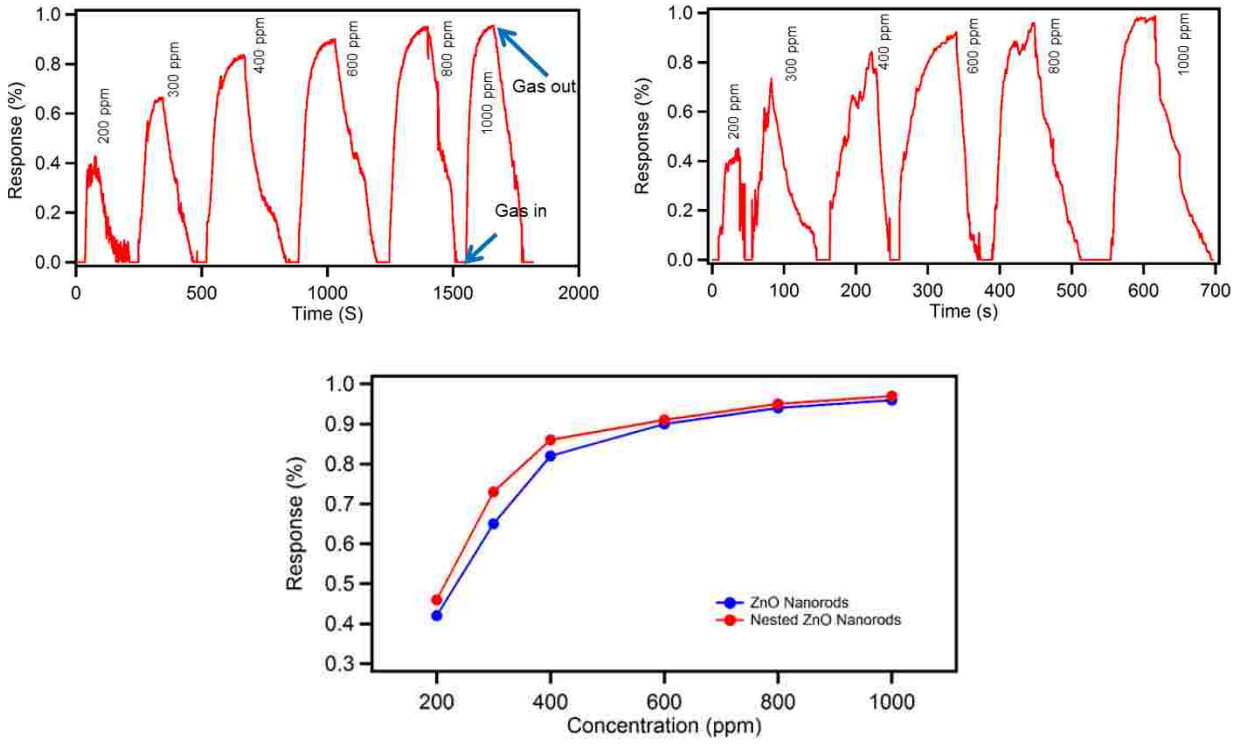


Figure 38. Sensing responses of ZnO nanorods reacting to different concentrations of ethanol vapor at 320℃ optimum working temperature before (top left) and after (top right) ALD coating with AZO layers. (bottom figure) Comparison of Sensing response as a function of ethanol concentration.

### 3.3.4 Response Time and Recovery Time Analysis

Response time and recovery time are also two significant parameters used to evaluate the sensing performance of solid-state gas sensors. Therefore, the response time and recovery time of ZnO nanorod gas sensors was investigated before and after coating with ALD AZO to ethanol vapor under optimum working condition (saturation concentration and optimum working temperature) as shown in Figure 39. The response time of sensor is defined as the time span starting from the moment when the sensor is exposed to the target gas until the moment when the response reaches 90% (known as $T_{90}$). The recovery time is defined as the time span from onset of target gas removal (= gas-out, measured at the point of 100% of the response) until the moment when the sensor response has decreased to 10% of the response ($T_{10}$). The response time of intrinsic hydrothermal ZnO nanorod sensors was 29 seconds and the recovery time was 207 seconds as shown in Figure 39 (left). After coating with AZO thin films, the sensing response of ZnO nanorod gas sensors experienced a significant improvement in the response time and recovery time, which were decreased to 17 seconds and 120 seconds respectively. These are two important parameters of ZnO nanorod gas sensors and our measurements demonstrate that the introduction of AZO coatings result in a considerable shortening of the response time and recovery time. After coating the original hydrothermal ZnO nanorods with granular polycrystalline ALD AZO nanolaminates, the surface-to-volume ratio of initially smooth single crystal ZnO nanorods is increased, which is one of the contributing factors that cause the decrease on the response time and the recovery time to ethanol vapor detection.

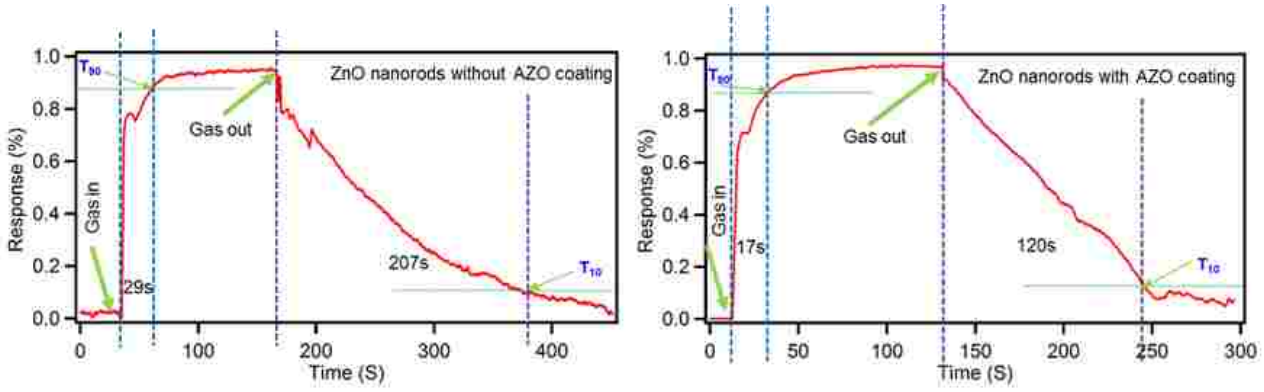


Figure 39. Sensing response of intrinsic ZnO nanorod sensors at saturation level ethanol vapor concentration at optimum operating temperature of 320℃ before (left) and after (right) having been coated with AZO.

### 3.4 Summary

In this chapter, the sensing performance enhancement of ZnO nanorod gas sensors by coating ALD aluminum doped ZnO thin films to the detection of the ethanol vapor concentration was demonstrated and investigated by using home-built gas sensor testing system. Single crystal ZnO nanorods were successfully grown by the hydrothermal method utilizing fine grain ALD ZnO seed layers deposited on a silicon substrate. A novel approach of ALD 3-D wrap-around nanolaminate coatings of delta doped AZO films was employed to enhance the sensing performance of ZnO nanorod gas detectors in terms of their sensing response, response time, and recovery time. The optimum operating temperature of the synthesized ZnO nanorod gas detector for ethanol vapor reaches a peak at 320℃. When the operating temperature is further increased beyond the peak temperature at 320℃, the sensing response of the ZnO nanorods to ethanol vapor dropped steadily, which was caused by a faster oxidation rate compared to the reducing reaction. Furthermore, the sensing response of the same ZnO nanorods before and after ALD coating with AZO increases as a function of increasing ethanol vapor concentration and reached saturation

when the concentration was increased to about 800 ppm and 1000 ppm, respectively. As a tangible improvement, the response time and recovery time of ZnO nanorod gas detectors for ethanol detection were shortened by the new approach of ALD AZO coatings. The sensing response improvement peaks at 37℃ human body temperature with approximately 100% performance enhancement.

# CHAPTER 4

## OBJECTIVE 2: NOVEL NESTED ZnO NANOROD/NANOTUBE GAS SENSORS

This chapter demonstrates a novel improvement on the sensing performance of ZnO nanorod gas sensors for ethanol vapor concentration detection by perfecting the design architecture of ZnO nanorod device bringing about a refinement in increasing the surface-to-volume ratio. A new integrated fabrication method combining hydrothermal method, Atomic Layer Deposition, introduction of sacrificial ALD layers serving as dummy variables and precision Ion Polishing System (PIPS) were conceived to realize the synthesis of novel nested coaxial ZnO nanorod/nanotube gas sensors. In this research, an $Al_2O_3$ sacrificial layer deposited by ALD as dummy variable was first introduced to wrap around the inner ZnO nanotube as a "gap filler". The initial ZnO nanorods serving to anchor the final sensor device were grown by hydrothermal growth on a fine grained ALD ZnO seed layer deposited on silicon substrates. Afterwards in the next process step ALD was introduced to deposit an $Al_2O_3$ sacrificial layer coating and plus another ZnO thin film to wrap around the surface of initial ZnO nanorods for the preparation of the ZnO nanotube. Due to the conformal deposition mechanism of ALD coating everything, next PIPS was required in the next step to selectively remove only the coating layers from the top of the ZnO nanorods in nanometer scale to expose the sacrificial $Al_2O_3$ layer and the outer ZnO layer. The exposed $Al_2O_3$ sacrificial layer was preferentially dissolved by wet-etching using a sodium hydroxide (NaOH) solution with pH 11 to finally form the novel nested coaxial nanorod/nanotube device architecture.

In this project, the sensing response of ZnO nanorod gas sensors without and with novel nested coaxial nanotubes were investigated by the upgraded gas sensor testing system containing two MFCs to accurately control the input concentration of the ethanol vapor. Two sensing response comparisons between conventional ZnO nanorod gas sensor design and the novel nested coaxial ZnO nanotube gas sensors were performed. This benchmark test includes the sensing response detection to exposure of ethanol vapor at saturation level concentration as a function of temperature to determine the optimum operating temperature and the response to the introduction of different concentrations of ethanol vapor at optimum working temperature to investigate the saturation level. The sensing response of the novel ZnO nanorod gas sensors designed with nested nanotubes achieved a maximum 150% performance improvement at low temperature over conventional ZnO nanorod gas sensors.

## 4.1 Synthesis Method

### 4.1.1 Synthesis Procedure

According to the architecture features of ZnO nanorod/nanotube gas sensors, the synthesis procedure comprises three basic processes: hydrothermal ZnO nanorod growth, coaxial ZnO nanotube fabrication by successive wrap-around ALD coating depositions including a sacrificial layer, and finally the formation of nested coaxial ZnO nanotubes.

*ZnO Nanorods Growth*

As explained in the synthesis procedure of Objective 1, hydrothermal growth was perfected to synthesize ZnO nanorods on ZnO seed layers prepared by ALD technology on a silicon substrate. The ZnO seed layers with 30 nm thickness were deposited by ALD at 200℃ with Diethylzinc (DEZ) and DI water used as the ALD precursor for Zn, while precursor 2 served as

oxidation agent. Afterwards the prepared seed layer received a furnace annealing in the air for 30 min at 350℃. Then the required intrinsic ZnO nanorods were grown on the ZnO seed layer by hydrothermal growth method in the autoclave with the reaction solution prepared with 0.03756 g zinc nitrate hexahydrate ($Zn(NO_3)6H_2O$) and 0.0176 g hexamethylenetetramine ($(CH_2)_6N_4$) dissolved in 60 mL DI water with 20.8 mM molar concentration of each solute [49]. Following hydrothermal growth, the prepared ZnO nanorods samples were ready for the next process steps as shown in Figure 40 (a).

*Nested Coaxial ZnO Nanotube Preparation*

The following three sub-procedures for the formation of the novel nested coaxial ZnO nanotubes were successfully implemented. First the idea was conceived ALD to deposit by ALD a sacrificial $Al_2O_3$ layer as a wrap-around dummy variable surrounding the original ZnO nanorod in the center which was followed by another ZnO thin film coating as the outermost layer. Due to the limited available spacing between the myriad of ZnO nanorods grown by the hydrothermal method, the thicknesses of the sacrificial layer and the ZnO layer were controlled to 20 nm. As shown in Figure 40 (b), the ALD deposition of the $Al_2O_3$ sacrificial layer was operated at 250℃ with trimethylaluminum ($Al_2(CH_3)_6$) and water vapor as the precursors of Al and oxidation agent, respectively. Figure 40 (c) shows the additional ZnO thin films deposited on the surface by ALD at 200℃ with diethylzinc ($Zn(C_2H_5)_2$) and water vapor as the precursors for Zn and oxidation agent, respectively. Following these two ALD coating processes, all surfaces of the ZnO nanorods were fully and uniformly covered with an $Al_2O_3$ sacrificial layer and followed by a ZnO thin film outer coating. Finally, the PIPS step was applied to expose the sacrificial layer by selectively removing the top cover (around 40 nm) on a nanometer scale as depicted in Figure 40 (d). The milling current was controlled at 20 μA and the rotation speed was set to 3 rpm. The operating

angle between the argon penning ion gun and the surface of the sample was 3° and the operating time was 2 minutes.

*Coaxial ZnO Nanotubes Formation*

The $Al_2O_3$ sacrificial layer functioning as "dummy variable" was exposed by removing the top ALD cover by PIPS. The purpose of the sacrificial layer is solely to leave an open annular ring surround the inner ZnO nanorod and thereby opening up two additional ZnO surfaces available to react with the target gas. To this end a special method or had to be developed to remove the sacrificial layer without causing any damage to the inner ZnO nanorods and the outer ZnO layer coating to merely leave the intended empty annular ring behind. Therefore, a sodium hydroxide (NaOH) solution with pH 11 was introduced to preferentially wet-etch away the sacrificial layer taking advantage of the different solubility ranges of $Al_2O_3$ and ZnO in basic solutions [21]. The precise chemical mechanism is discussed in Section 4.2 Synthesis Mechanism. After the sacrificial layer selective removal by NaOH, the novel coaxial nested ZnO nanotube gas sensors were finally completed exhibiting two additional sensor reaction surfaces created by the open inner and outer surface of the empty annular ring layer for ethanol vapor concentration detection as schematically shown in Figure 40 (e).

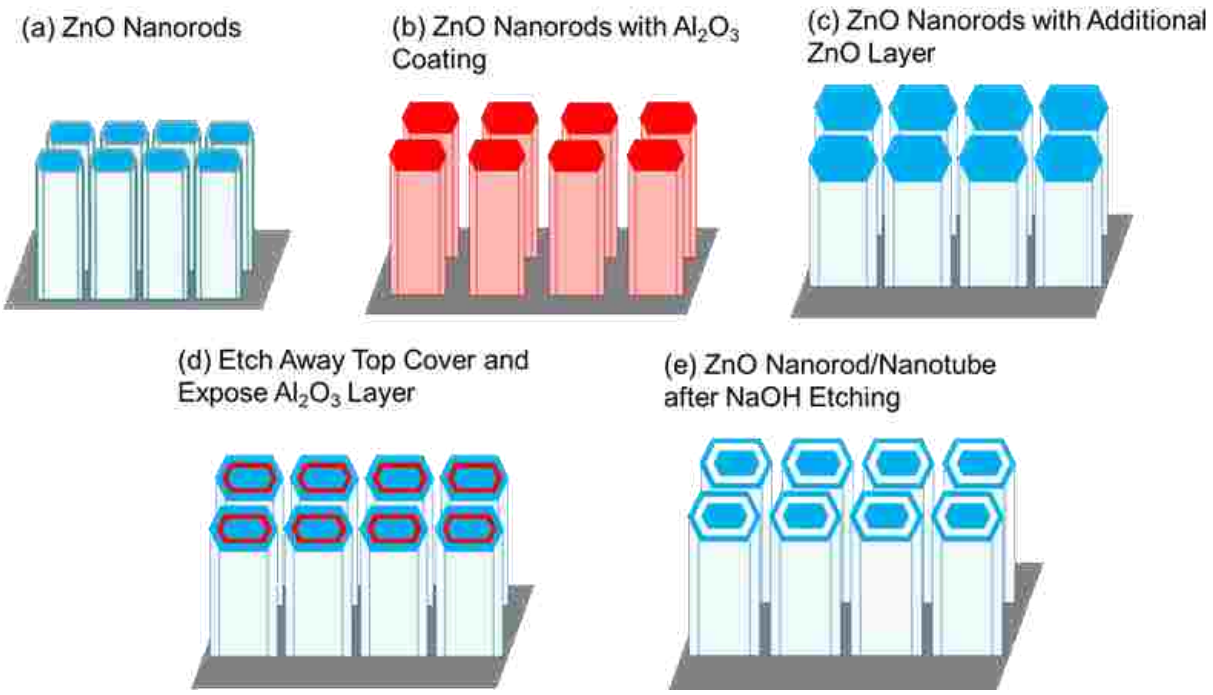


Figure 40. Schematic 3-D depiction of (a) original hydrothermal ZnO nanorods, (b) ZnO nanorods with ALD $Al_2O_3$ sacrificial wrap-around layer, (c) ZnO nanorods with additional ALD ZnO wrap-around layer, (d) top cover removed by PIPS ion milling, (e) ZnO nanorod/nanotube after removal of sacrificial layer with NaOH etching leaving ultimately the intended empty annular ring exposing two additional reactive ZnO surfaces to the target gas.

Figure 41 shows a schematic in cross-sectional view of the complex sacrificial layer removal to leave an exposed empty annular ring g structure surrounding the inner ZnO nanorod which completes the novel nested coaxial nanotube gas sensors synthesis process sequence. Figure 41 (a) explains how the top cover is formed with the inner ZnO nanorods receiving 3-D ALD wrap-around coatings with the $Al_2O_3$ sacrificial layer followed by the outer ZnO thin film coating. The thickness of the top cover was around 40 nm with 20 nm $Al_2O_3$ layer and 20 nm ZnO thin films respectively. After PIPS removed the top layer covering, the cross-sectional schematic view of the ZnO nanorods with the sacrificial layer exposed from the top for wet-etching is shown in

Figure 41 (b). After preferentially wet-etching for complete removal of the sacrificial layer, the nested coaxial ZnO nanotube gas sensors were finally completed exhibiting now two additional reaction surfaces formed by the empty annular ring of the former sacrificial dummy layer as shown in Figure 41 (c).

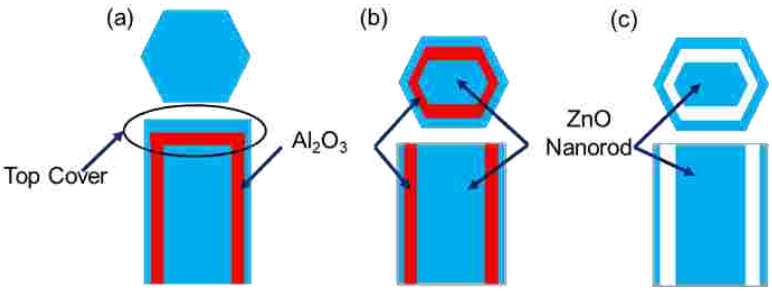


Figure 41. Cross-sectional schematic view of (a) ZnO nanorod with $Al_2O_3$ sacrificial layer coating and an outer ZnO layer, (b) ALD top cover layers removed by PIPS, (c) completed novel nested coaxial ZnO nanotube sensor design after NaOH etching to remove the sacrificial layer.

### 4.1.2 Physical Characterization

FE-SEM was applied to investigate the surface morphology of the synthesized coaxial nested ZnO nanorod/nanotube gas sensor design. Figure 42 shows the FE-SEM micrographs of ZnO nanotube gas sensors highlighting special features at various stages during the fabrication process. The original single crystal ZnO nanorods displaying precise crystallographic hexagonal cross-sections from the hexagonal wurtzite ZnO structure were grown by hydrothermal method and are shown in Figure 42 (a). Figure 42 (b) shows a granular coating on all ZnO nanorods resulting from the ALD $Al_2O_3$ sacrificial layer and ZnO thin films depositions, which cover and seal the surface of all ZnO nanorods the very top cover of the ZnO nanorods. In the following PIPS was applied to remove the two ALD $Al_2O_3$ and ZnO thin films from the top of the ZnO nanorods

to expose the sacrificial layer from the top as shown in Figure 42 (c) and (d). The $Al_2O_3$ sacrificial layer was preferentially etched by NaOH alkali solution, creating an empty annular ring surrounding the isolated intrinsic ZnO nanorods in the center. It is important to remind the reader that this process step of dissolving the sacrificial $Al_2O_3$ layer in alkali solution and thereby creating an empty annular space ends up exposing two additional reaction surfaces. This process creates the ultimate refinement of our novel sensor design achieving our objective of significantly increasing the surface-to-volume ratio by fabricating a true nested coaxial ZnO nanotube with a center nanorod as shown in Figure 42 (e) and (f). Theoretically every additional sacrificial layer will expose two more reactive ZnO surfaces available to contribute to improved sensing performance. The density of initial hydrothermal nanorods and the remaining spacing between neighboring nanorods are the only practical limits and obstacle to adding n-number of sacrificial layers. However, replacing the bottoms up approach of allowing random nucleation of nanorods could be replaced by a top-down technology involving photolithographic patterning to design a lower density of ZnO nanorods. In such a case of lower density of nanorods it is straightforward to fabricate nested ZnO nanotubes with several sacrificial layers. However, the optimum between lower density of ZnO nanorods and larger numbers of sacrificial layers would have to be determined by a long series of experiments, which was beyond the scope of this work. Figure 42 (g) shows a cross-sectional view of the novel nested synthesized ZnO nanorod/nanotube gas sensors revealing an average height of nanorods of ~750 nm.

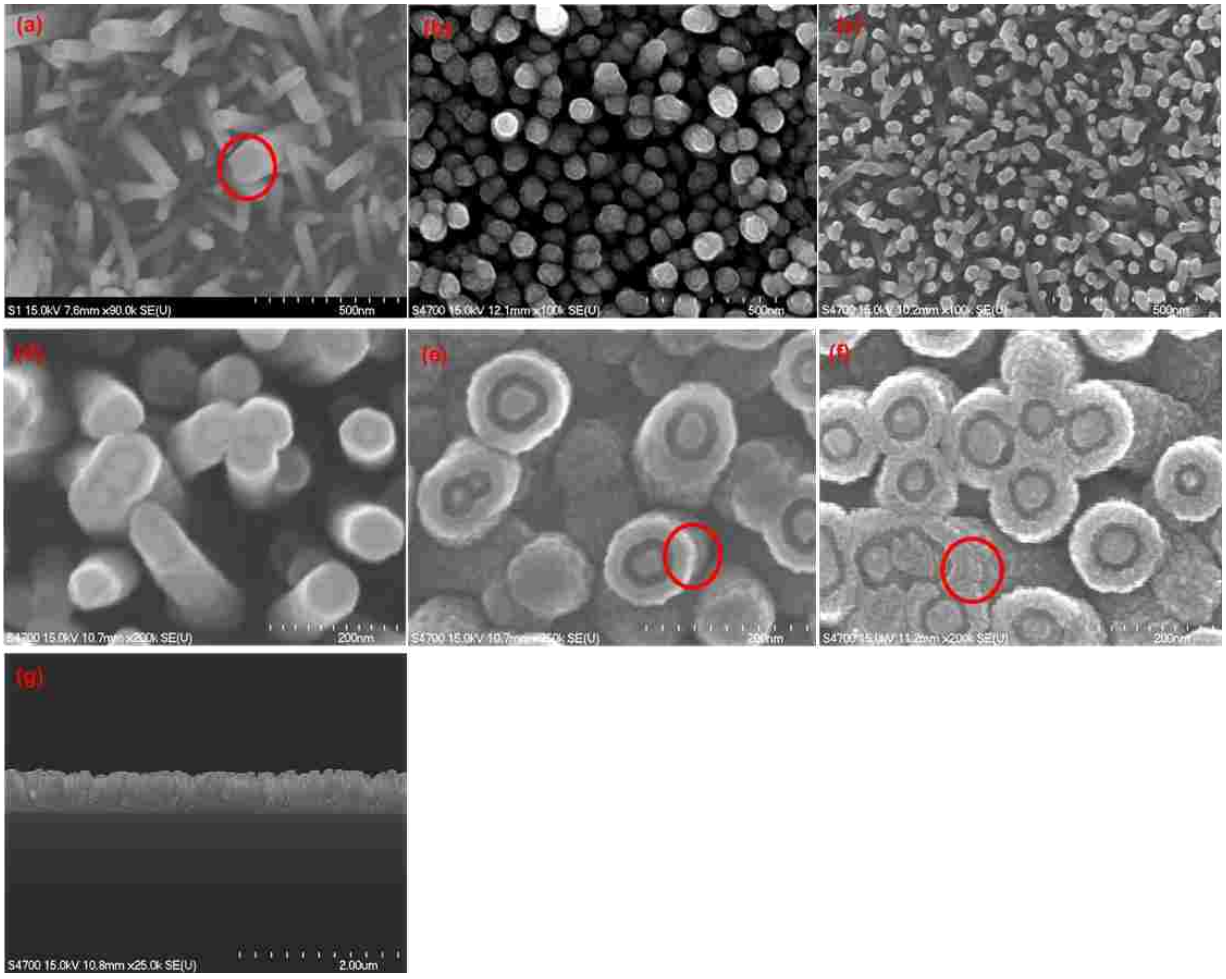


Figure 42. FE-SEM images of novel ZnO nanorod/nanotube coaxial structure synthesis process a) intrinsic hydrothermal ZnO nanorods with hexagonal wurtzite structure, b) granular coating on ZnO nanorods after coating with an $Al_2O_3$ sacrificial layer and ZnO thin films, c) and d) top cover removed by PIPS ion milling to expose the sacrificial layer, e) and f) the sacrificial layer preferentially etched away by pHs11 NaOH solution, and g) cross-section revealing an average height of nanorods of ~750 nm.

### 4.2 Synthesis Mechanism

For the practical realization of the novel nested ZnO nanorod/nanotube sensors, the conception of the $Al_2O_3$ sacrificial layer is the most innovative element for the fabrication process

of the nested coaxial ZnO nanotube sensor design. The chemical dissolution of the $Al_2O_3$ sacrificial layer serves to separate the central ZnO nanorod from the outer ZnO nanotube with an empty annular ring remaining in between. Due to the crucial importance of the sacrificial layer for the novel device architecture of the novel nested ZnO nanotube gas sensors, it was critically important to develop a safe method for the selective removal of the $Al_2O_3$ sacrificial layer to complete the ZnO nanotube sensor device structure without causing any damage to the center ZnO nanorods and the outer surrounding ZnO nanotubes.

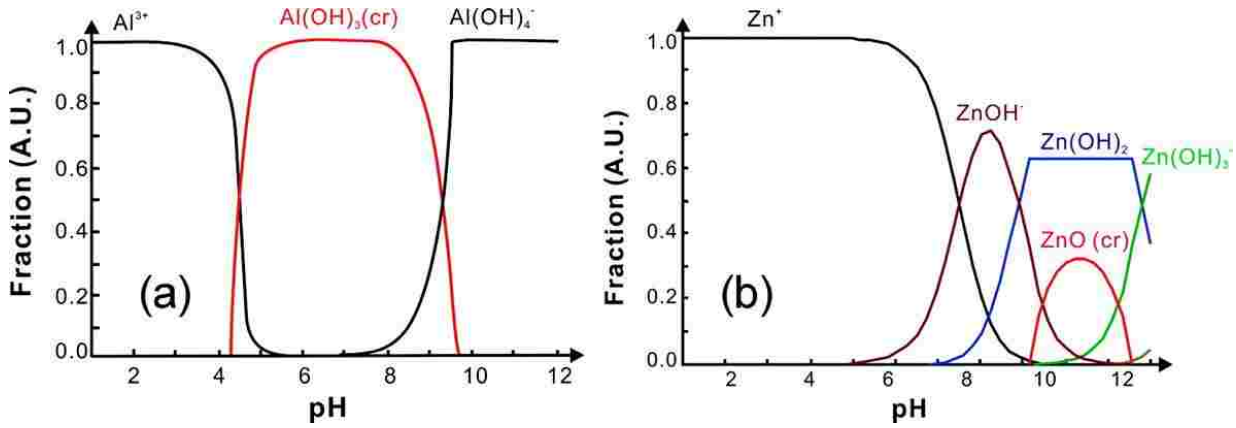


Figure 43. Thermodynamic modeling diagram showing the distributions of the fraction (a) $Al^{3+}$ species as a function of pH, (b) $Zn^{2+}$ species vs pH of alkali etch solution [21].

Wet-etching was the method of choice and was introduced to preferentially remove the $Al_2O_3$ sacrificial layer to form nested ZnO nanorod/nanotube structures based on the solubility of $Al_2O_3$ and crystalline ZnO. Figure 43 (a) demonstrates the thermodynamic modeling diagram of the distribution of the status of $Al^{3+}$ species in the $Al^{3+}$ solution with 0.001 mM molar concentration with various pH values at 298 K [21]. Based on Figure 43 (a), solid alumina is capable to exist in a solution with pH range of 4.2 to 9.8, which implies solid alumina can be dissolved in a solution

with pH value of either below 4.2 or above 9.8. However, according to the thermodynamic modeling diagram in Figure 43 (b), the condition to maintain crystalline ZnO in the solution lies in the pH range between 9.2 and 11.5 [21]. Therefore, to remove $Al_2O_3$ while simultaneously preventing any chemical attack on ZnO, the safe pH value of the wet-etching alkali solution has to be in the range of 9.8 to 11.5. Based on our experimental test results, a sodium hydroxide solution with a pH 11 was chosen to dissolve the $Al_2O_3$ sacrificial layer and form ZnO nanorod/nanotube structure while maintaining the integrity of the surrounding ZnO.

## 4.3 Gas Concentration Detection

### 4.3.1 Sensing Response Analysis as A Function of Temperature

In this section, the sensing response of our novel nested coaxial ZnO nanorod/nanotube gas sensors was investigated as a function of temperature by exposing the active ZnO sensor material to ethanol vapors at saturation level concentration at different temperatures (25℃, 37℃, 100℃, 150℃, 200℃, 250℃, 320℃, 340℃) to determine the optimum working temperature. A sensing response comparison between the novel nested ZnO nanorod/nanotube gas sensors and conventional ZnO nanorod gas sensors was performed, as shown in Figure 44. Both the sensing responses of the novel nested ZnO nanorod/nanotube gas sensors and the conventional ZnO nanorod gas sensors increased with rising temperature until the maximum value at 320℃ is reached. Afterwards, the sensing response steadily decreases for higher temperatures beyond the peak. This is attributed to the faster oxidation reaction at the higher peak temperature compared to the slower reduction reaction. The improvement mechanism is illustrated in Section 3.3.2.

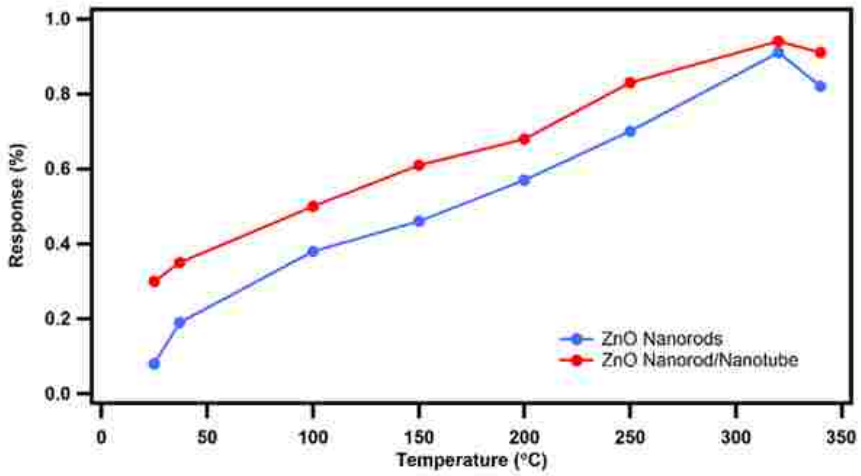


Figure 44. Comparison of the sensing response to ethanol vapor at saturation level concentration as a function of temperature of the novel nested coaxial ZnO nanorod/nanotube gas sensors versus conventional ZnO nanorod gas sensors.

Based on the direct comparison of the sensor response versus temperature data shown in Figure 44, the novel nested ZnO/nanotube gas sensor design exhibits a significant improvement in sensing response compared to the conventional ZnO nanorod gas sensors. The observed enhancement in the sensing response of the novel nested sensor design is primarily caused by the increased surface-to-volume ratio. The removal of the $Al_2O_3$ sacrificial layer, created a novel ZnO nanorod sensor with a nested coaxial nanotube structure, where the resulting empty annular ring space generated two additional ZnO reaction surfaces. In our new sensor design and process integration the chemical dissolution & removal of the $Al_2O_3$ sacrificial layer served to uncover and to expose two additional reaction surfaces for ethanol vapor detection. The tangible benefit resulted in a sizeable increase of the surface-to-volume ratio, which translated into a much better sensing response performance.

The sensing response of ZnO nanorod gas sensors was vastly improved after implementing the nested coaxial nanotube design creating two additional reaction surfaces for an increased surface-to-volume ratio. The plot of Figure 45 shows the enhancement gain of the novel nested ZnO nanorod/nanotube gas sensors to the ethanol vapor concentration detection under saturation level concentration as a function of temperature. The enhancement gain at each temperature was calculated based on Equation 46. The data demonstrate that the largest enhancement gain can be realized at lower temperatures with maximum enhancement gain of ~150% at 25℃. The data also emphasize that the response difference between the two sensor designs narrows down as the temperature approaches the optimum peak operating temperature. This effect is attributed to the much faster oxidation reaction rate at high temperature compared to the competing reduction reaction rate.

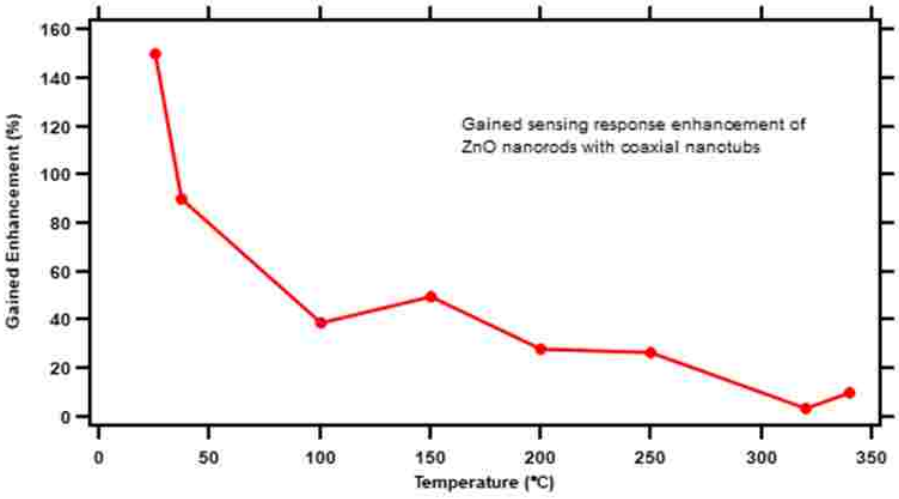


Figure 45. Enhancement gain on the sensing response of the novel nested ZnO nanorod/nanotube gas sensors compared to conventional ZnO nanorod gas sensors.

4.3.2 Analysis of Sensing Response as A Function of Ethanol Vapor Concentration

In this section the sensing response of ZnO nanorod gas sensors with and without nested coaxial ZnO nanotubes has been investigated as a function of ethanol vapor concentrations (200 ppm, 300 ppm, 400 ppm, 600 ppm, 800 ppm, 1000 ppm) at the confirmed optimum working temperature (320℃). The plot of Figure 46 shows the sensing response comparison between the novel nested coaxial ZnO nanorod/nanotube gas sensors and the conventional ZnO nanorod gas sensors.

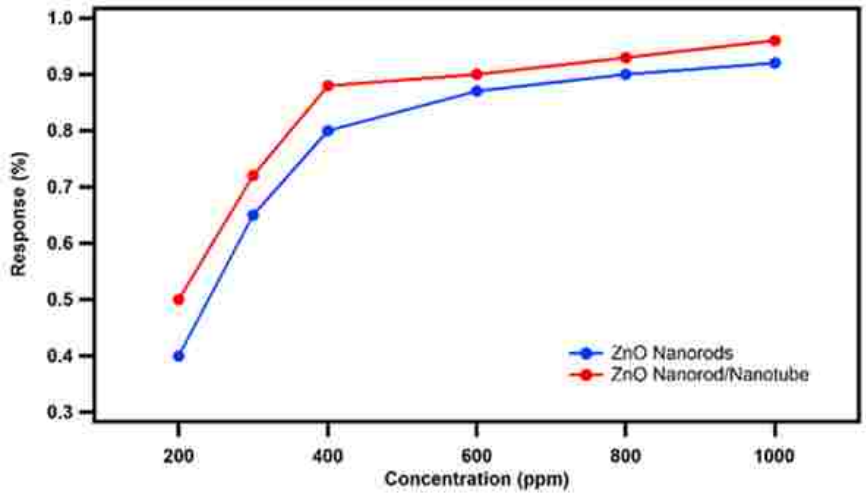


Figure 46. Comparison of the sensing response to ethanol vapor as a function of concentrations at 320℃ of the novel nested ZnO nanorod/nanotube gas sensors versus conventional ZnO nanorod gas sensors.

The sensing response for both sensors increases as a function of rising ethanol vapor concentration until saturation level. The data of plot reveal that the novel ZnO nanorod gas sensors with coaxial ZnO nanotubes always achieve a higher sensing response at every target gas concentration compared to the conventional ZnO nanorod gas sensors. Furthermore, the saturation

level concentration of the novel nested coaxial ZnO nanotube gas sensors is around 1000 ppm, which is higher than the saturation concentration of conventional ZnO nanorod gas sensors (800 ppm). This is attributed to the two additional reaction surfaces generated by the empty annular dummy ring space of the novel nested coaxial ZnO nanotube design, which translates to an increased surface-to-volume ratio for the new sensor.

### 4.4 Summary

In this chapter, a novel nested coaxial ZnO nanotube gas sensor device was fabricated by an integrated process combining hydrothermal growth of nanorod anchors with ALD technology. These novel nested ZnO gas sensor architectures were investigated with newly upgraded gas sensor testing system using two MFCs for the precise control of the target vapor concentration. As a key component an ALD $Al_2O_3$ sacrificial layer was introduced to create nested coaxial ZnO nanotubes. After removing the top cover by PIPS, the $Al_2O_3$ sacrificial layer was preferentially removed by wet chemical etching in a NaOH solution at pH 11. This novel sensor device design and process integration successfully created nested coaxial ZnO nanorod/nanotube structures with two additional reaction surfaces which generates another critically important advantage by simultaneously increasing the surface-to-volume ratio. In principle our approach is amenable to add more than one sacrificial layer to create more multiple nested tube-in-tube ZnO nanostructure sensor devices. Theoretically, every additional annular sacrificial layer will add two new reaction surfaces after wet chemical etch removal. However, in our case due to the limited available spacing between neighboring ZnO nanorods grown by the hydrothermal method, only one layer of coaxial ZnO nanotube was synthesized to fabricate our nested coaxial ZnO nanorod/nanotube gas sensors. By increasing reaction surfaces and nucleation sites with our new design, the sensing response of

ZnO nanorod gas sensor achieved a significantly improved response enhancement employing nested coaxial ZnO nanotubes with empty annular sacrificial layers. Especially, the saturation level was improved from 800 ppm to 1000 ppm. Compared to conventional ZnO nanorod gas sensor benchmarks, our novel nested ZnO nanotube gas sensors achieved a sensing response improvement of roughly 150% at a low temperature of 25℃, which is considered a major milestone for our novel sensor design.

# CHAPTER 5

## OBJECTIVE 3: COAXIAL ZNO NANOTUBE GAS SENSORS SYNTHESIZED INSIDE POROUS TEMPLATES

This chapter pursues a completely different technology approach and serves to illustrate the sensing performance of coaxial ZnO nanotube gas sensors synthesized inside the myriad of pores of porous templates by Atomic Layer Deposition technology to ethanol vapor concentration detection. Section 1.3 explained that properly designed coaxial nested ZnO nanotube gas sensors provide the key advantages of higher surface-to-volume ratio and add two additional reaction surfaces for ethanol vapor concentration detection. This process design leads to more reaction sites in the same area compared to conventional ZnO nanorod sensors. The process method in this chapter combines ALD technology, PIPS, and chemical wet-etching technique to fabricate coaxial nested ZnO nanotube gas sensors inside the individual pores of porous templates. In contrast to the previous chapters, here the feasibility of fabricating ZnO nanotubes with template replication was investigated which presents a radical shift in technology. In this section ZnO nanotubes as well as nanotubes were synthesized inside porous templates, which can be either porous Anodic Aluminum Oxide (AAO) or porous silicon. For reasons of mechanical stability porous Si templates were the preferred substrates for this work. The fabrication strategy focused on building the ZnO nanotube sensor device one layer at the time via ALD synthesis inside the plethora of millions of pores in a porous template sample. Unlike the case in the previous chapter, assembling the nanolaminate layers for a ZnO nanotube device design by template replication, here the outer ALD layer had to be synthesized first by chemisorption on the walls of the individual pores. ALD

synthesis of nanolaminates in template replication works from the outside to the inside. The outer layers of the nanotube get completed first by ALD and the innermost one is the last to be completed, because the process sequence works in reverse order with template replication. Another major difference is the absence of the single crystal inner ZnO nanorod grown by hydrothermal method. As in the previous cases, the deposition thicknesses of the $Al_2O_3$ sacrificial layer and ZnO thin films were precisely controlled by ALD technology. In an analogous process step PIPS was applied to remove the top cover of ZnO nanotube to provide access to the partially exposed sacrificial layer. This was followed by NaOH alkali preferential wet-etching to form ZnO nanotubes with an empty annular ring synthesized completely inside the pores of porous Si templates. Additionally, ALD AZO coatings were deposited on the surface of the novel nested coaxial ZnO nanotube gas sensors to further improve the sensing performance.

In this research, the sensing responses of ZnO nanorod gas sensors with one layer and two layers of ZnO nanotube to ethanol vapor were investigated as a function of temperature and concentration by our custom-built gas sensor testing system. In an effort to continually improve the sensor performance further the best features and practices from Objectives 1 and 2 were combined AZO coatings on the surface of ZnO nanotube gas sensors were also studied. The template replication approach required another ZnO film coating with same thickness as AZO coatings by ALD were deposited on the surface of ZnO nanotube gas sensors to provide a conductive layer to connect each nanotube, which were disconnected and electrically isolated by the PIPS milling action. The twofold purpose of the additional ZnO conductive layer with same thickness is to guarantee a scientifically equivalent comparison with only one sensor variety for the analysis of the performance enhancement for ethanol vapor concentration detection.

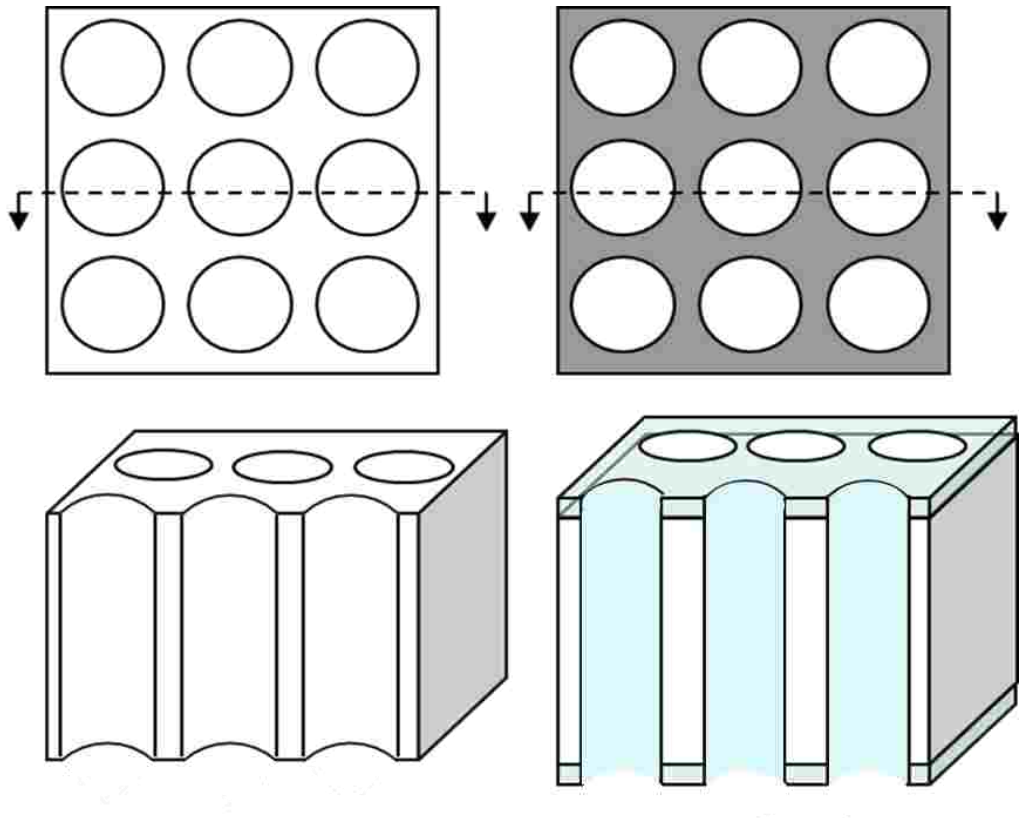

Figure 47. Schematic depiction of top view and cross-sectional view of porous templates before (left) and after (right) introducing ALD film deposition with completely conformal coatings covering the inside walls of every single pore as well as the template surface. The ALD coating follows a sequence from first synthesizing the outermost layer on the pore walls, which is subsequently followed by the inner ALD layers one by one.

Figure 47 illustrates the schematics of top view and cross-sectional view of porous templates before (left) and after (right) introducing ALD deposition with completely uniform coatings on both top and the walls of pores. The top cover will be removed by ion milling to expose the sacrificial layer. Figure 48 shows the SEM micrograph of feasibility study in porous Si template demonstrating the potential to create multiple annular empty spacings for gas detection after wet etch removal of several sacrificial $Al_2O_3$ layers.

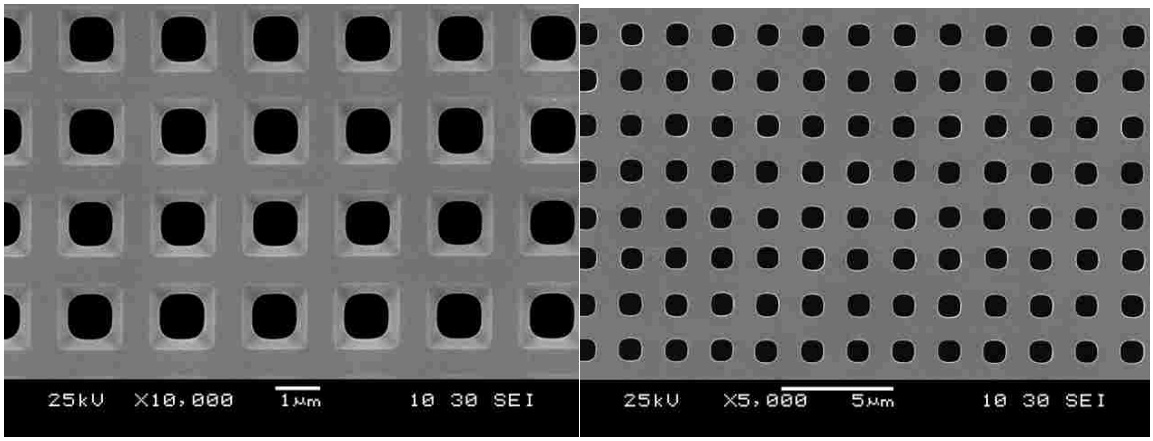


Figure 48 a). The two SEM micrographs present a front (left) and backside (right) view of a generic porous Si template sample, revealing a regular array of pores, which are defined by mask and photolithography technology used in microelectronics clean rooms.

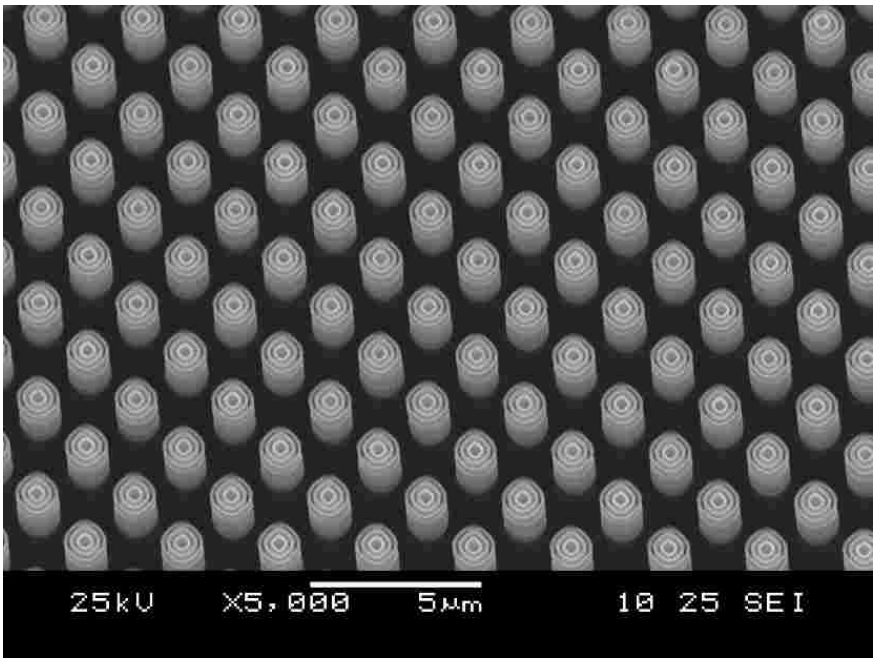


Figure 48 b). The SEM micrograph shows a feasibility study in a porous Si template demonstrating the potential to create multiple annular empty spacings for improved gas detection architectures after wet etch removal of several sacrificial $Al_2O_3$ layers. The remaining nested nanotubes consist of alternating ALD layers of ZnO.

## 5.1 Synthesis Method for the Template Replication Approach

### 5.1.1 Synthesis Procedure

The ALD synthesis procedure of our novel nested coaxial ZnO nanotube gas sensors inside porous Si templates includes the same four basic processes: ALD thin films deposition, PIPS milling, ZnO nanotube formation, and further enhancement with AZO coatings. The main difference for the template replication approach is the complete absence of the hydrothermal inner ZnO nanorod because all nanolaminate layers are now synthesized by ALD, but in reverse order first starting with the outer layer and ending up with the innermost layer.

*ALD Deposition*

According to the conformal deposition feature, ALD deposition technology requires a suitable surface for coating and in the case of the porous Si templates the inside walls of the millions of individual pores were coated following the sequence of outer layer first followed the next inner layer in the assembly of the final nanolaminate structure. In this manner first the ZnO layer was ALD deposited on the inner wall of pores and in the 2$^{nd}$ step the ALD $Al_2O_3$ sacrificial layer followed. To continuously operate the ALD deposition it was necessary to compromise on one single deposition temperature for both the alumina and zirconia films. Therefore, the ALD deposition temperatures of the ZnO thin films and $Al_2O_3$ sacrificial layer were modified and fixed at 220℃. Like previously diethylzinc and water vapor were used as the ALD precursors of ZnO thin films deposition, as shown in Figure 49 (b), (d), and (f). Meanwhile, trimethylaluminum and water were used as the precursors of the synthesis of $Al_2O_3$ sacrificial layer, as shown in Figure 49 (c) and (e). The purpose of the ZnO thin films shown in Figure 49 (b) is to build up the connection between each ZnO nanotube, because the porous template consists of Si. The procedures shown in Figure 49 (c) and (d) can be considered as one single super cycle for the synthesis of one layer

of ZnO nanotube. Therefore, to obtain more nested nanotube one simply has to repeat more ALD super cycles inside the individual pores of the porous template. The separation between each ZnO nanotube with same axis was determined by the thickness of the $Al_2O_3$ sacrificial layer.

For the case of AAO porous templates, the thickness of the ZnO thin films and $Al_2O_3$ sacrificial layer were controlled at 20 nm. Eventually, nested coaxial ZnO nanotubes with thickness of 20 nm were formed after the sacrificial layer was removed by NaOH wet-etch. For two layers of nested ZnO nanotubes, the separation between the two ZnO nanotubes with same axis was 20 nm which was determined by the thickness of $Al_2O_3$ sacrificial layer. The reason to limit the ALD layer thickness to 20 nm is the relatively small diameter of AAO pores. The average diameter of the AAO pore is around 250 nm. This small pore diameter requires to fix the thickness of ZnO nanotube to 20 nm in order to fit in two layers of coaxial nanotubes into one pore.

For the case of Si porous templates, the pore diameter was much larger and either 1 μm or 2 μm and thus allowed more ALD super cycles to be fitted into each pore. Because of the larger Si pore diameter, the thickness of the ALD ZnO thin films was controlled to 50 nm with the goal to obtain ZnO nested nanotubes with 50 nm thickness. However, the thickness of the $Al_2O_3$ sacrificial layer was selected at 100 nm. Therefore, the final distance between each coaxial ZnO nanotubes was 100 nm determined by the thickness of the sacrificial layer to guarantee sufficient space in the empty annular ring for the target gas molecules to also reach the bottom of ZnO nanotube. The larger sacrificial annular ring spacing also serves to leave extra space for the final ALD AZO coatings for the ultimate refinement of the nested sensor performance.

*PIPS Milling*

After the ALD thin film deposition, PIPS was required to remove the top cover layers piled up by the ALD deposition. However, the milling condition has to be based on the thickness of the

top layer cover, which turned out to be different for the case of the AAO porous templates versus the porous Si templates. The thickness of the top cover layers on the AAO template was 60 nm for one layer of ZnO nanotube and 100 nm for two layers of ZnO nanotubes. However, in the case of the porous Si templates, the thickness of the top cover was 200 nm for one layer of ZnO and 350 nm for two layers of nested ZnO nanotubes. For both AAO and porous Si templates, the milling current was controlled at 20 μA and the rotation speed was set to 3 rpm. The operating angles and the operating time were modified according to the different thicknesses of the top covers.

For the AAO templates, the operating angle was 3° and the operating time was 2 minutes for one layer of ZnO nanotube, while the operating time was 4 minutes for two layers.

For the porous Si templates, the operating angle was set to 6° due to the thicker top cover. The operating time was set to 4 mins for one layer of ZnO nanotube and 6 mins for two layers.

*ZnO Nanotube Formation inside Porous Templates*

After removing the top cover by PIPS milling, the $Al_2O_3$ sacrificial layer was exposed and ready for removal by NaOH wet-etching at a specific pH 11 value based on the solubility variety concept. After the sacrificial layer has been preferentially removed by a pH 11 NaOH alkali solution, the nested coaxial ZnO nanotube gas sensors were completed with either three reaction surfaces obtained for the case of one sacrificial layer or alternative with five reaction surfaces for the case of two sacrificial layers, as illustrated in Figure 49 (g).

*Final ALD AZO Coating to optimize the Performance of nested Tube-in-Tube ZnO Gas Sensors*

Keeping best practices for continually improving the sensing performance of our nested coaxial ZnO nanotube gas sensors to ethanol vapor concentration detection, the benefit of Objective 2 was also introduced into the synthesis of ZnO nanotube gas sensors by adding a final coating of ALD AZO thin films to all surfaces. Diethylzinc ($Zn(C_2H_5)_2$), trimethylaluminum

($Al_2(CH_3)_6$), and DI water were used as the ALD precursors for the deposition of AZO with 2% Al dopant and 20 nm thickness. The nested ZnO nanotube gas sensors samples were split into two equal parts, where only one part received the final AZO coating while the other part received instead the ALD ZnO conductive layer deposition with same thickness. This split experiment allows us to quantitatively evaluate the benefit in sensor performance of this last AZO coating.

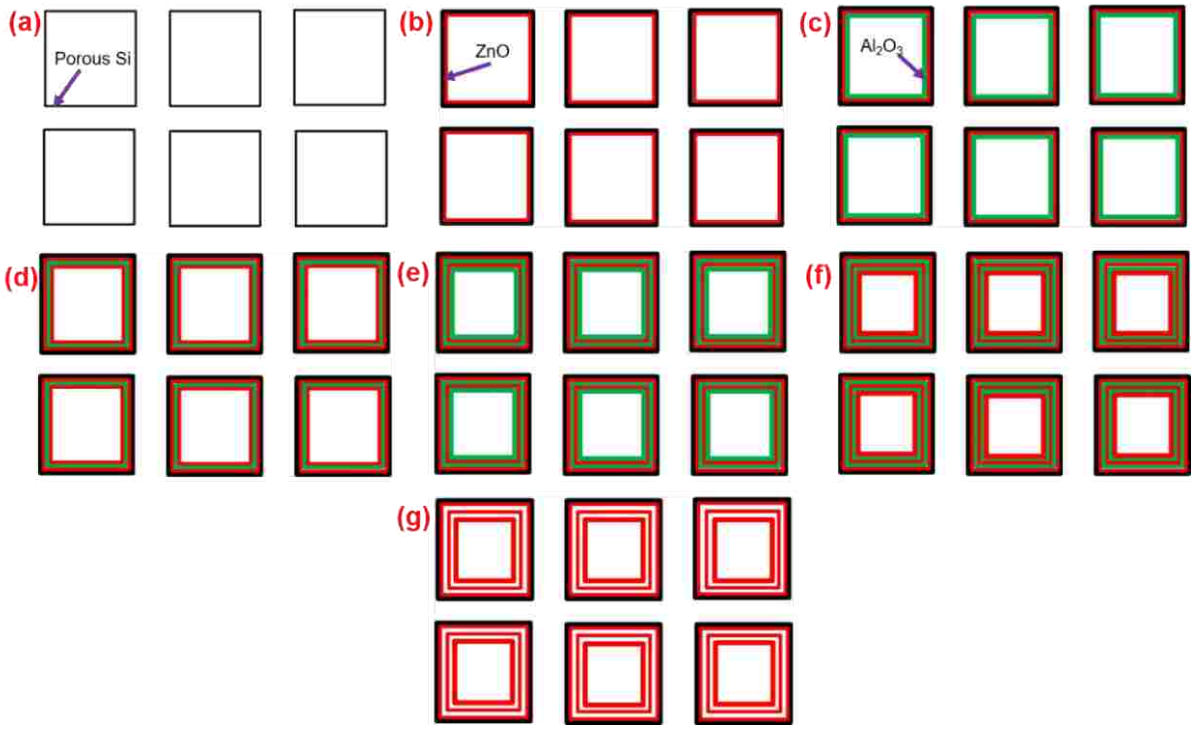


Figure 49. Top-down schematic view explaining graphically the layer-by-layer process sequence for the ALD nanotube synthesis inside the individual pores of porous templates, which is required for the fabrication of the nested ZnO gas sensor architecture.

Figure 50 shows the cross-sectional schematic diagram of multiple nested coaxial ZnO nanotubes synthesis process inside the pores of porous Si templates. In the first process step, the ZnO conductive layer was deposited on all pore walls of porous Si. Then next followed the ALD

deposition of the $Al_2O_3$ sacrificial layer and afterwards another ALD ZnO thin layer, as shown in Figure 50 (b) and (c). This completes a super cycle and the first outer layer of a nested ZnO nanotube ring. From here it is straightforward to add more tube-in-tube nested nanotube structures by repeating such an ALD super cycle. Figure 50 (d) and (e) show the second super cycle layer for a further nested ZnO nanotube synthesized inside the initial nanotube. After removing the top cover by PIPS milling, the sacrificial layer was preferentially completely etched away by Ph 11 alkali NaOH with enough time, as shown in Figure 50 (f).

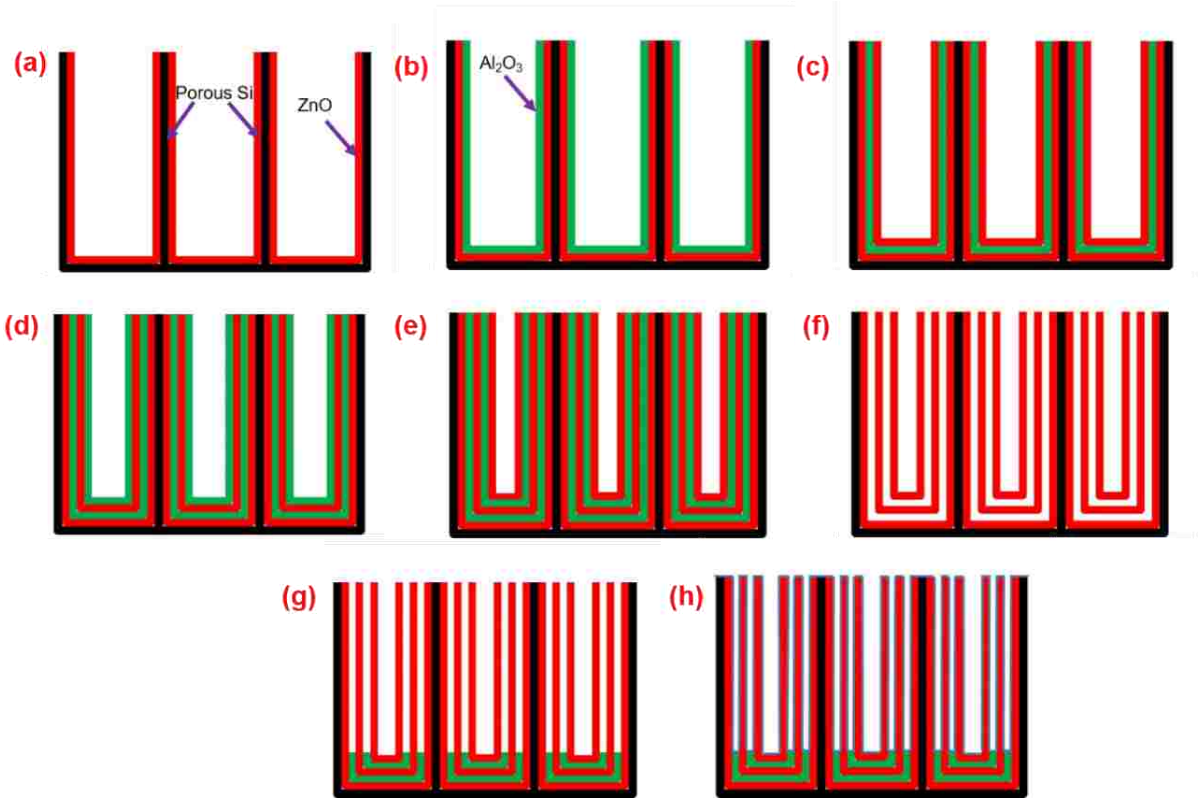


Figure 50. Cross-sectional view showing schematically the systematic ALD coatings sequence required for the ZnO nanotube synthesis procedure inside each pore of the porous Si template.

However, the complete etch removal of the sacrificial layer may cause a drop or collapse of the inner ZnO nanotubes, which may negatively impact the sensing performance of the nested ZnO nanotube gas sensors. For this reason, only partial wet etching has been performed in this research to retain the sacrificial layer in the bottom of the laminate structure inside each pore. The retained sacrificial layer helps to anchor nested nanotubes at the bottom of the pores. In case the entire sacrificial layers were removed accidentally, then the inner ZnO nanotubes might be falling out with nothing to attach them to the bottom part of the pores, as shown Figure 50 (g). Therefore, the NaOH wet etching time had to be optimized by a series of timed etch experiments to remain on the safe side this requirement. Following this process sequence finally, the multiple nested coaxial ZnO nanotube gas sensors were completed ad topped off with a ZnO thin film deposition for creating either the necessary conductive layer or the desired last ALD AZO coating for the ultimate performance refinement, as shown in Figure 50 (h).

### 5.1.2 Physical Characterization of the Multiple Nested Coaxial Sensor Fabrication by Template Replication

FE-SEM micrographs were used to characterize the surface morphology of the synthesized of the advanced multiple nested ZnO nanotube gas sensors inside porous templates, which include porous AAO and porous Si templates.

*ZnO Nanotubes Synthesized on AAO Substrate*

Figure 51 shows SEM micrographs of the ZnO nanotubes synthesized inside porous AAO templates. The pores exhibit random irregular shapes, because in this case no photolithography was used to generate the porous structure. Figure 51 (a) and (b) demonstrate one layer of ALD ZnO nanotube synthesized inside the porous AAO template with the ALD top cover already

removed by PIPS milling. In Figure 51 (c) and (d) FE-SEM micrograph results of two nested coaxial layers of ZnO nanotubes is shown. However, due to the smaller limited diameter of the AAO pores, two layers of coaxial ZnO nanotubes is the maximum number of nested nanolaminate layers that can be fitted into the AAO pore structure. As shown in the micrographs of Figure 51 (c) and (d), the pores of the AAO template were fully filled with $Al_2O_3$ sacrificial layers and ZnO thin films following merely two layers of ZnO nanotube synthesis. The micrograph in Figure 51 (e) reveals the granular polycrystalline top cover on the surface of the AAO template after two ALD cycles of ZnO nanorods synthesis procedure. These two ALD coatings completely covered the top entrance of the pores of the AAO template and closed off the surface completely.

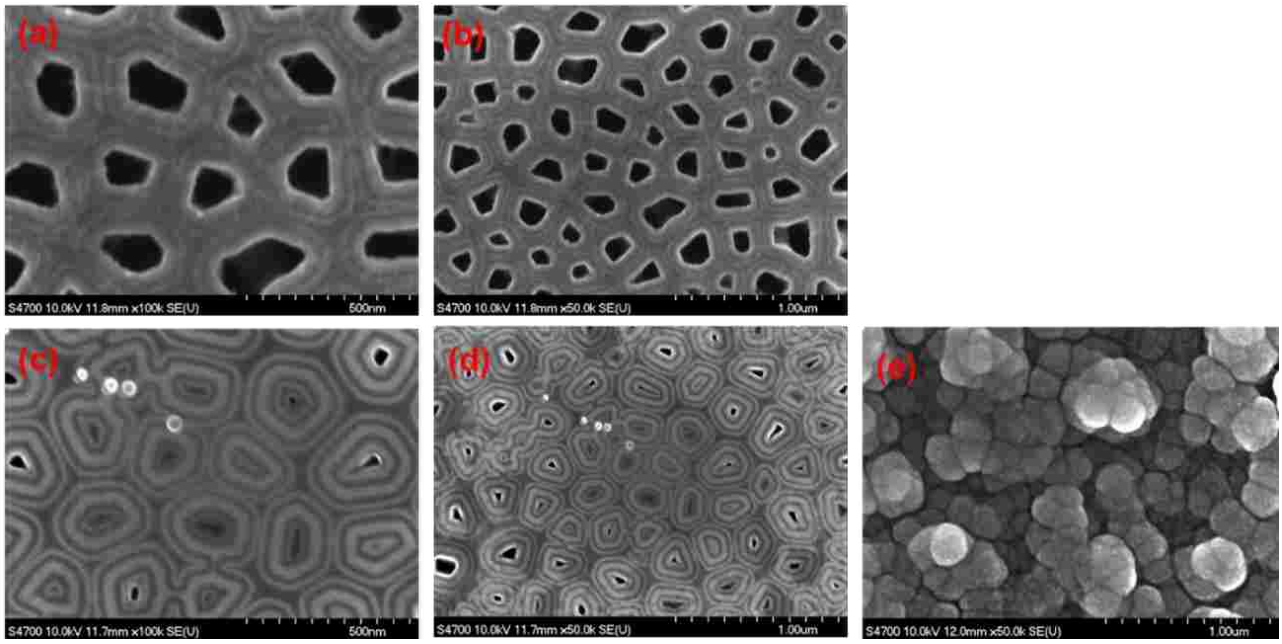


Figure 51. FE-SEM micrographs of the novel nested coaxial ZnO nanotube structures, which were ALD synthesized with one super cycle in porous AAO templates (a) and (b), with two super cycles (c) and (d), and last revealing the surface morphology with two super cycles before the PIPS milling process (e).

*Multiple Nested ZnO Nanotubes Synthesized inside Porous Si Substrate*

Because of the brittleness of the porous AAO template and the rather limited pore diameter, we investigated porous Silicon templates which allow the ALD synthesis of multiple nested tube-in-tube ZnO nanotube gas sensors because of the much larger pore diameter and better mechanical stability. Porous Si templates with 2 µm diameter pores enabled the synthesis of more than one layer of ZnO nanotube and provide sufficient space between each coaxial nanotube for a final ALD AZO coating.

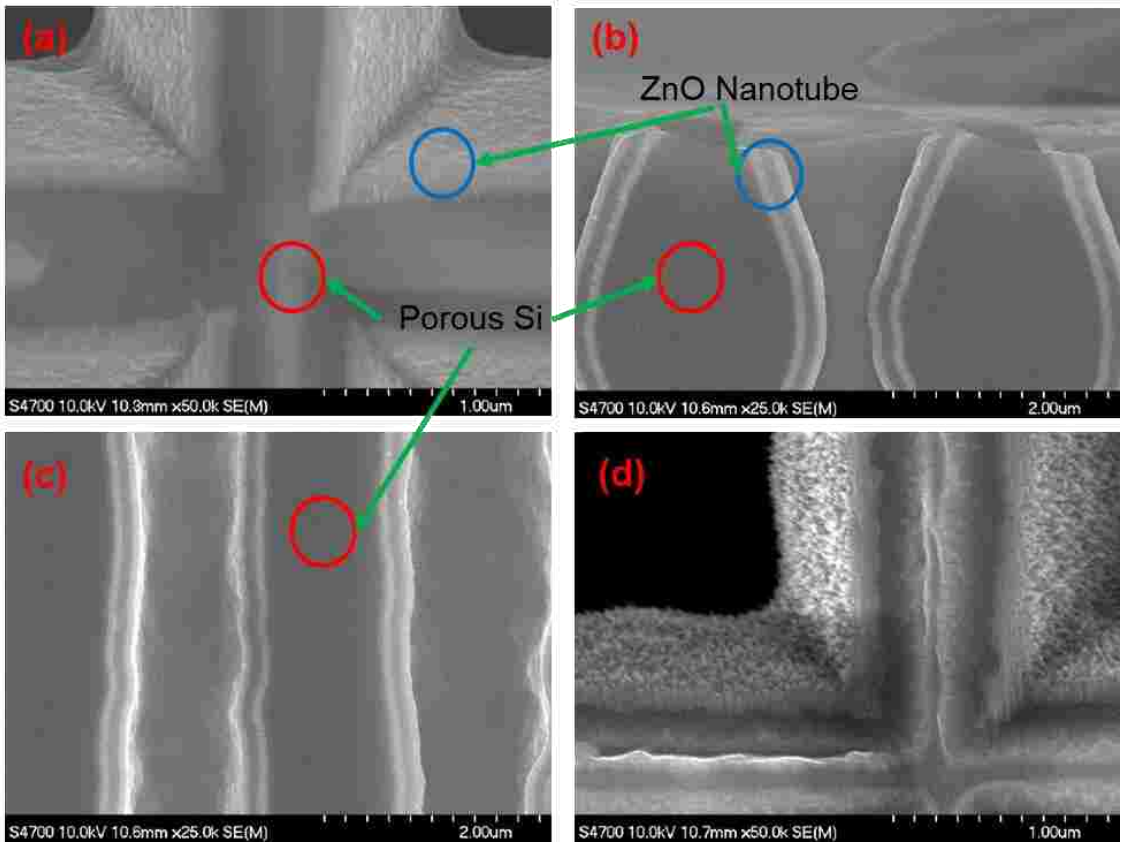


Figure 52. FE-SEM micrographs of nested ZnO nanotube structure with one cycle wet-etched by NaOH solution (a) top view with one layer of ZnO nanotube, (b) cross-sectional view of the top area of ZnO nanotube with top cover removed by PIPS ion milling, (c) cross-sectional view of the middle section of ZnO nanotube, and (d) top view of one layer of ZnO nanotube after introducing a final ALD AZO coating.

Figure 52 shows the FE-SEM micrographs of the result of ZnO nanotube gas sensors for the case of one cycle after removing the $Al_2O_3$ sacrificial layer by NaOH. The area in the red circles in Figure 52 (a), (b), and (c) shows the porous Si substrate and the area in the blue circles presents the synthesized ZnO nanotubes. The ZnO thin films sticking to the porous Si wall are used to create the conductive connection between the ZnO nanotube and the nanotube fabricated in all the neighboring pores beside it. Figure 52 (b) shows a cross-section of the top area of the porous Si with synthesized ZnO nanotube, which demonstrates the ALD top cover has been removed by PIPS milling to expose the sacrificial layer. Figure 52 (c) shows the middle section further down the cross-section, which presents the shape of the nested ZnO nanotube. As the very last process step polycrystalline ALD AZO coatings exhibiting granular structure were applied for a final improvement upgrade of the sensing performance of our most advanced multiple nested coaxial ZnO nanotube gas sensor device, as shown in Figure 52 (d).

Figure 53 shows the FE-SEM micrographs of a genuine multiple nested ZnO nanotube structure comprised of two super cycles after removing the $Al_2O_3$ sacrificial layer by NaOH solution. Figure 53 (a) shows the top view of the two layers of coaxial ZnO nanotubes synthesized on a porous Si template. Figure 53 (b) shows the cross-sectional view of the top area of synthesized multiple nested ZnO nanotubes with two super cycles, where the top cover was removed by PIPS milling. The granular structure in Figure 53 (d) presents the very last ALD AZO coating deposited on the surface of the two layers of coaxial ZnO nanotubes.

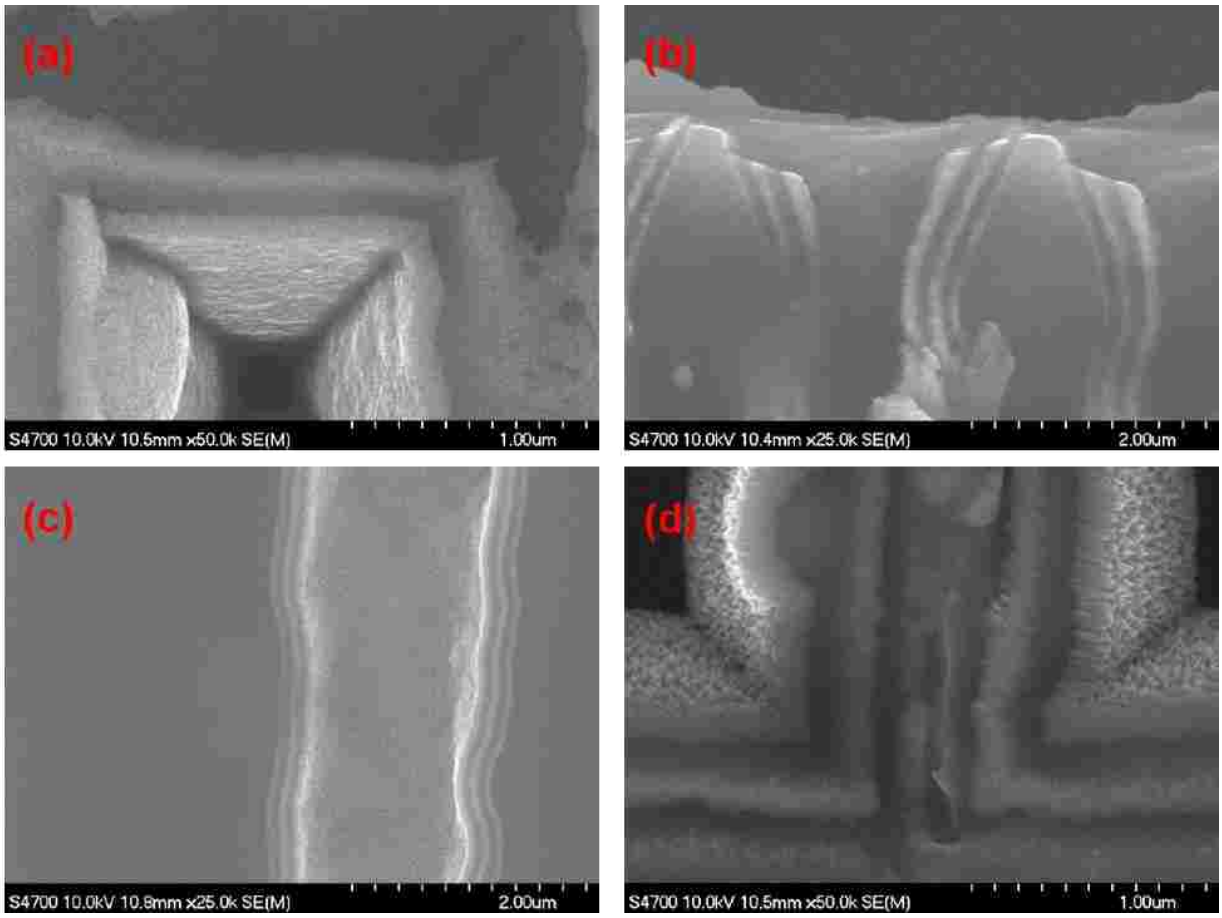


Figure 53. FE-SEM micrographs of nested ZnO nanotube structure with two cycles wet-etched by NaOH solution (a) top view with two layers of ZnO nanotubes, (b) cross-sectional view of the top area of ZnO nanotube with top cover removed by PIPS ion milling, (c) cross-sectional view of the middle section of ZnO nanotube, and (d) top view of two layers of ZnO nanotubes after introducing a final ALD AZO coating.

*NaOH Wet-Etching Time Optimization Investigation*

As illustrated in the synthesis procedure, the timing of the NaOH wet-etching procedure carries significant implications and consequences for the synthesis of multiple nested ZnO nanotube gas sensors. to the wet etch time needs to be precisely controlled to leave some remaining

sacrificial layer in the bottom part for anchoring the inner nanotubes thereby guaranteeing the optimum sensing performance of our multiple nested ZnO nanotube gas sensors.

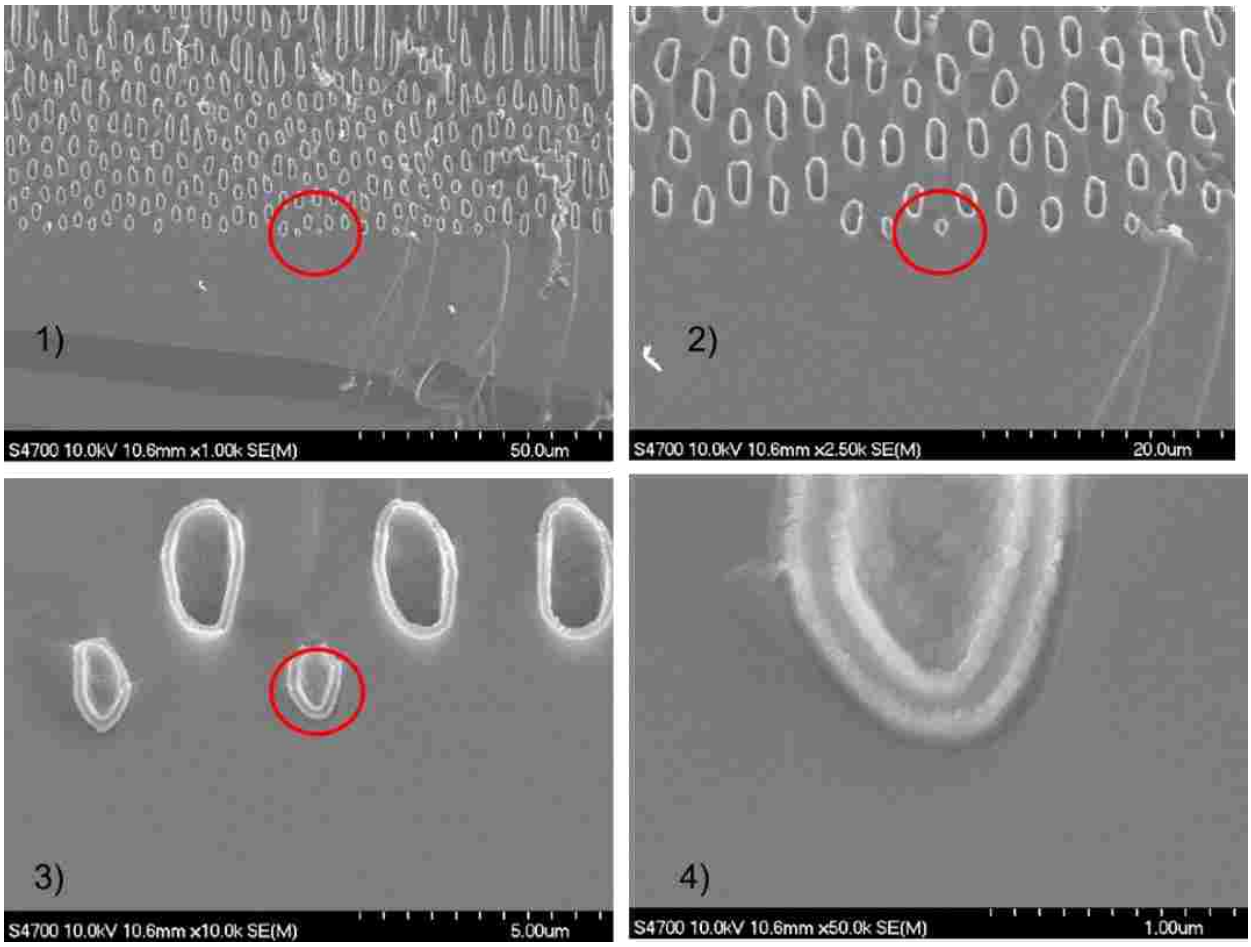


Figure 54. FE-SEM cross-sectional images of ZnO nanotube structure with one super cycle wet-etched by NaOH for 6 hours with spacing created between ZnO nanotube and ZnO layer as shown in 4).

Figure 54 shows the FE-SEM cross-section micrographs of a nested ZnO nanotube structure with one super cycle, which received wet-etching by NaOH for 6 hours. The investigated area was focused on the crucial bottom anchoring area of the pores in porous Si. The increasingly

higher magnification zoom-in micrographs from Figure 54 (1) ➔ (2) ➔ (3) ➔ (4) reveal the empty dummy spacing at the bottom of the pore structure resulting from the sacrificial layer removal. Based on the evidence of Figure 54 (4), the $Al_2O_3$ sacrificial layer has been completely etched away by NaOH even at the bottom of the pore. The SEM micrographs prove that the wet-etching effort has reached to the bottoms of the pore on porous Si and the synthesized ZnO nanotube.

Next the micrographs of Figure 55 show the FE-SEM cross-section images of the nested ZnO nanotube structure with one super cycle, which were this time wet-etched by NaOH for only 5 hours. The investigation procedure is same as the previous one with 6 hours etching time. However, after 5 hours NaOH preferentially etching, there were still parts of the $Al_2O_3$ sacrificial layer remaining at the bottom areas of porous Si and synthesized ZnO nanotubes, which can be observed from the green circled area in Figure 55 (4). The remaining sacrificial layer in the bottom part of the nested nanotube structure serves the important function to anchor the inner nested ZnO nanotubes and to create the conductive substrate.

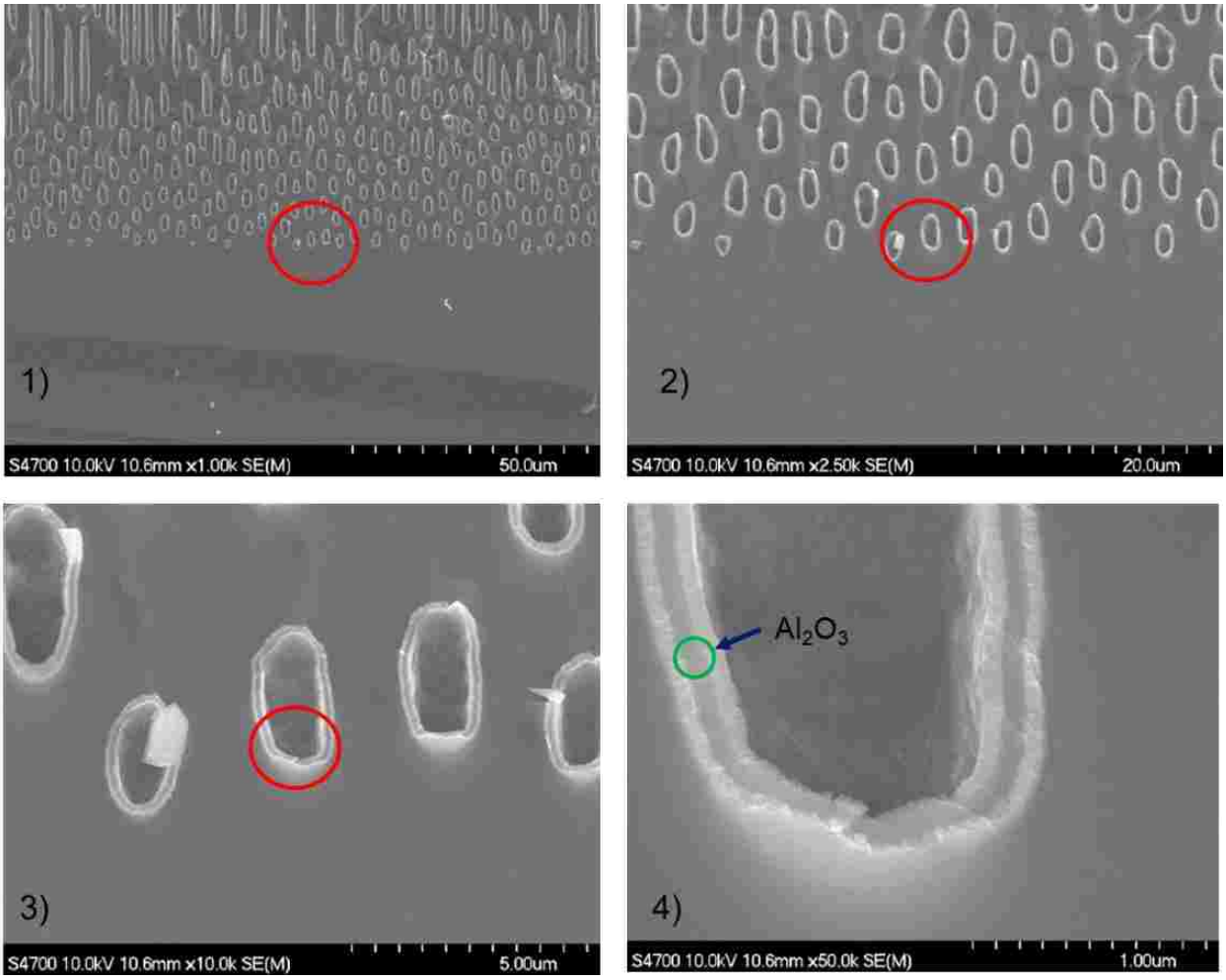


Figure 55. FE-SEM cross-section images of ZnO nanotube structure with one super cycle wet-etched by NaOH for 5 hours with partial $Al_2O_3$ layer remained at the bottom as shown in 4) green circled area.

## 5.2 Detection of the Ethanol Vapor Concentration

### 5.2.1 Sensing Response of our Advanced Multiple Nested ZnO Nanotube Gas Sensors from Template Replication as a Function of Temperature

In this section, the sensing response of one layer and two layers of nested ZnO nanotube gas sensors with and without ALD AZO coating were investigated during exposure to ethanol vapor at saturation concentration as a function of temperature (37℃, 100℃, 150℃, 200℃, 250℃,

320℃, 340℃) to determine the optimum working temperature. A comparative study was performed on the sensing performance of multiple nested ZnO nanotube gas sensors consisting of two varieties of ZnO nanotubes with eitherone or two nested nanotube structures and a final ALD coating of either ZnO or AZO. The measured results are plotted in Figure 56. The sensing response as a function of temperature of advanced nested ZnO nanotubes with one super cycle coated with only ZnO is indicated in the graph in light red color, while ZnO nanotubes with one super cycle coated with ALD AZO is shown in dark red color. The case of multiple nested ZnO nanotubes with two super cycles coated with only ZnO is plotted in green color, while the most advanced multiple nested ZnO nanotube structure with two super cycles and a final coating with ALD AZO is indicated with blue color. A review of the results reveals that the sensing response of all nested ZnO nanotube gas sensors increase with rising temperature until the maximum value is reached at 320℃. Afterwards beyond the peak the response decreases at higher temperature due to the faster oxidation reaction rate explained in the previous sections. This is the basic sensing response change phenomenon as a function of temperature, which is valid for all of our nested ZnO nanostructure gas sensors.

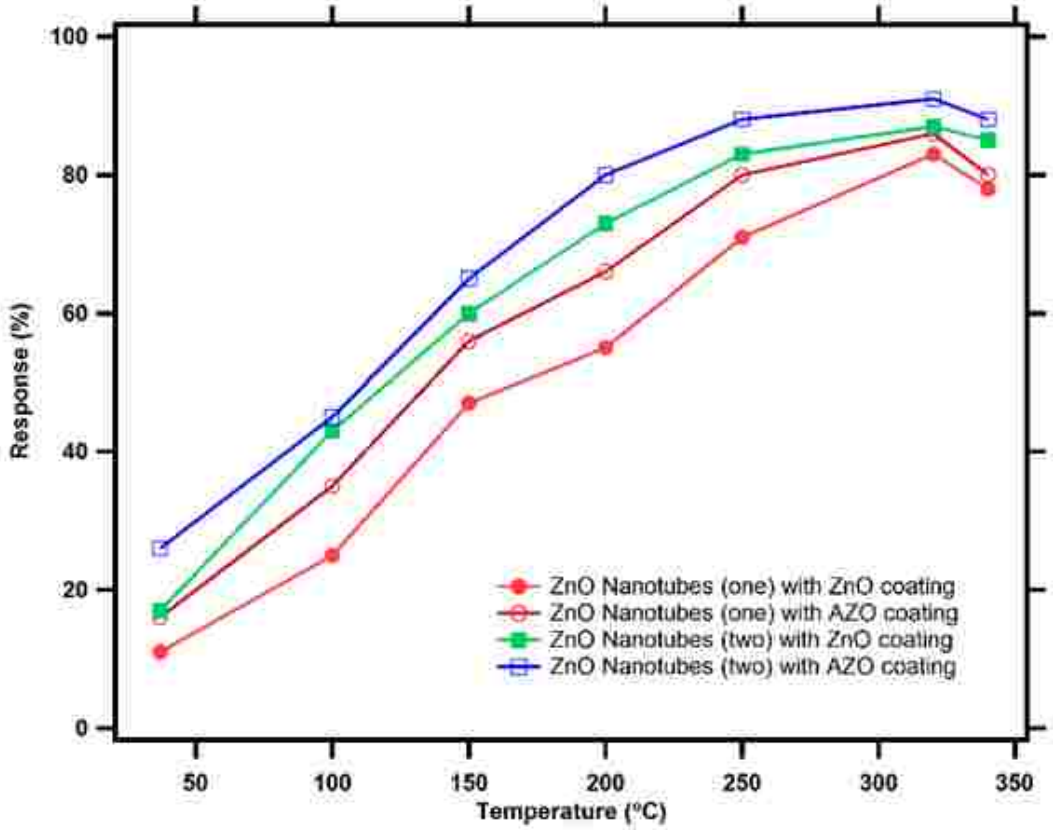


Figure 56. Measured sensing response trends as a function of temperature of our advanced multiple nested ZnO gas sensors consisting of one super cycle or two cycles and finally coated with either ALD ZnO or AZO thin films at saturation level ethanol vapor.

*Sensing Response Comparison between One Layer and Two Layers of Multiple Nested ZnO Nanotubes*

The data plotted in the graph of Figure 56 reveal very interesting trends and insights to guide the optimization of our most advanced multiple nested nanotube sensor device fabricated by template replication technology. The trends in our measurements provide a strong validation of the novel sensor device architecture and the advanced processing technology conceived during the work on this dissertation

First let us focus on the sensing response comparison was between the case of one layer super cycle and two layers super cycle of ZnO nanotubes with only ALD ZnO thin films as conduction layer, which correspond to the red and green color in Figure 56. According to the comparison, over the entire temperature range the green curve is higher than the red curve, but the gain is more pronounced for the lower temperatures. Basically, this means a sensor device with two nested nanotubes perform better than a sensor with only one. The upshot is that the sensing response of ZnO nanotube gas sensors to ethanol vapor concentration was significantly improved by adding one additional coaxial nested ZnO nanotube to the device structure. This is attributed to the two additional reaction surfaces introduced for each removed sacrificial layer in the coaxial nested ZnO nanotube design, which leads to a corresponding increase in the surface-to-volume ratio. The enhancement gain realized for adding one additional nanotube layer is shown in Figure 57. Based on the result in Figure 57, the maximum enhancement gain reached up to 72% at 100℃ and declines steadily towards the higher operating temperatures.

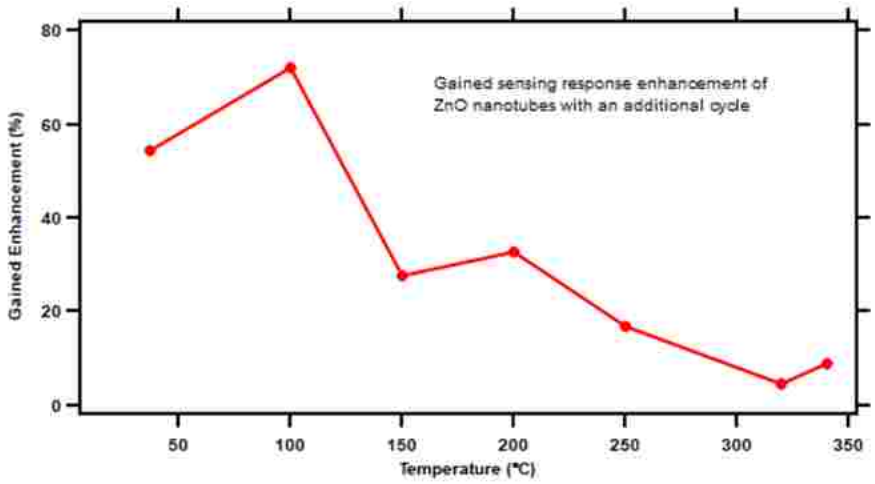


Figure 57. Enhancement Gain by adding one additional coaxial nested ZnO nanotube ring structure.

*Comparison of Sensing Response between One Layer of ZnO Nanotubes with ZnO Coatings and Two Layers of ZnO Nanotubes with AZO Coatings*

The second sensing response comparison can be drawn between one layer super cycle of ZnO nanotube with merely a ALD ZnO final coating and two layers super cycle for multiple nested ZnO nanotube gas sensors with the special intended ALD AZO coatings. The synthesis of two nested layers for a multiple nested tube-in-tube ZnO nanotube gas sensor with ALD AZO coatings has incorporated the learning of Objectives 1 and 2 in the previous chapters. Therefore, based on the AZO sensor enhancing mechanism confirmed in Objective 1 and the hypothesis of the benefits of increasing the surface-to-volume ratio in Objective 2, the analysis of these measurement data will provide information about the maximum improvement in sensor response by upgrading the device design with extra oxygen vacancies and electrons from AZO and by adding extra reaction surfaces. The enhancement gains obtained for our most advanced process at different temperatures were plotted as a function of temperature in Figure 58. The maximum gained enhancement that can be obtained for our most advanced sensor design is 136% at 37℃ (human body temperature).

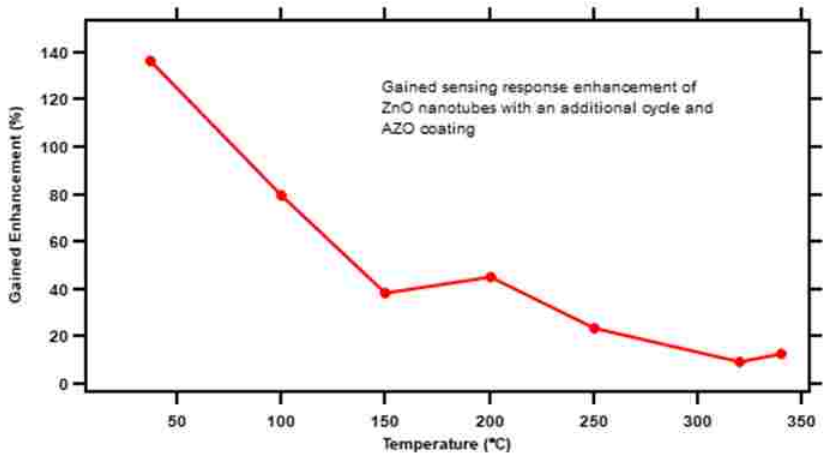


Figure 58. Enhancement Gain as a function of temperature for our most advanced multiple nested sensor design with additional reaction surface and AZO coatings.

5.2.2 Sensing Response of ZnO Nanotube Gas Sensors as a Function of Target Gas Concentration

In this section, the sensing responses of one layer and two layers of multiple nested ZnO nanotube gas sensors with and without ALD AZO coating were investigated as a function of ethanol vapor concentrations (200 ppm, 300 ppm, 400 ppm, 600 ppm, 800 ppm, 1000 ppm) at the confirmed optimum working temperature of 320℃. The graph of Figure 59 shows the sensing response as function of target gas concentration for one layer and two layers of multiple nested ZnO nanotube gas sensors with only ALD ZnO or with ALD AZO coatings. The data in the graph show that the sensing response of the multiple nested ZnO nanorod gas sensors rises steadily as a function of increasing ethanol vapor concentration until saturation level is reached.

Furthermore, a clear trend in saturation enhancement by increasing the surface-to-volume ratio is detected in the sensing performance of ZnO nanotube gas sensor by comparison of the data in Figure 59. As shown in the graph of Figure 59, the saturation level for a one-layer nested ZnO nanotube gas sensor was around 600 ppm, while the saturation level for a two-layer coaxial multiple nested ZnO nanotube gas sensor was increased to about 750 ppm. In the previous chapters ALD AZO coatings have been shown to significantly improve the sensing performance of ZnO nanostructure gas sensors for the detection of ethanol vapor concentration. But the graphs for AZO coating versus no AZO coating in Figure 59 improve only negligibly the saturation level. Therefore, the observed enhancement is attributed primarily to the one additional layer of nested ZnO nanotube, which serves to increase the surface-to-volume ratio with two extra reaction surfaces per added sacrificial layer.

However, the saturation levels of nested ZnO nanorod gas sensors introduced in the section for Objectives 1 and 2 are in the range of 800 ppm to 1000 ppm. The lowered saturation level in the present multiple nested ZnO nanotube gas sensors in Chapter 5 is caused by the porous Si

photolithographic process fabrication technique, which produces a much lower density of nested nanotubes due to larger pore diameter. This effect causes a decrease in the surface-to-volume ratio compared to the ZnO nanorods grown by hydrothermal method with much higher nanorod density. Table IX shows in column 1 the roughly counted density of ZnO nanorods grown by hydrothermal method in Objective 1, in column 2 the nested ZnO nanorod/nanotubes with ZnO nanorods grown by hydrothermal method in Objective 2, and in column 3 the multiple nested tube-in-tube ZnO nanotubes synthesized in porous Si template in Objective 3. In column 3 the density of the synthesized multiple nested ZnO nanotubes was limited by the porous Si fabrication technique, which in this case produced large 2 µm pore diameters. For this reason, the density of nested nanotubes resulting from template replication at $\sim 10^7/cm^2$ is three orders lower compared to the ZnO nanorod density of $\sim 10^{10}/cm^2$ in Objective 1 and the ZnO nanorod/nanotubes in Objective 2 obtained by hydrothermal growth. There is also another drawback on the overall available surface-to-volume reactive surface found between the nested ZnO nanorod/nanotubes synthesized inside porous templates versus ZnO nanorods grown by hydrothermal method in Objective 2. This is caused by the much lower heights of only 0.6 µm to 0.7 µm of ZnO nanorods grown by hydrothermal method versus a height of 135 µm nanotubes generated inside the porous templates.

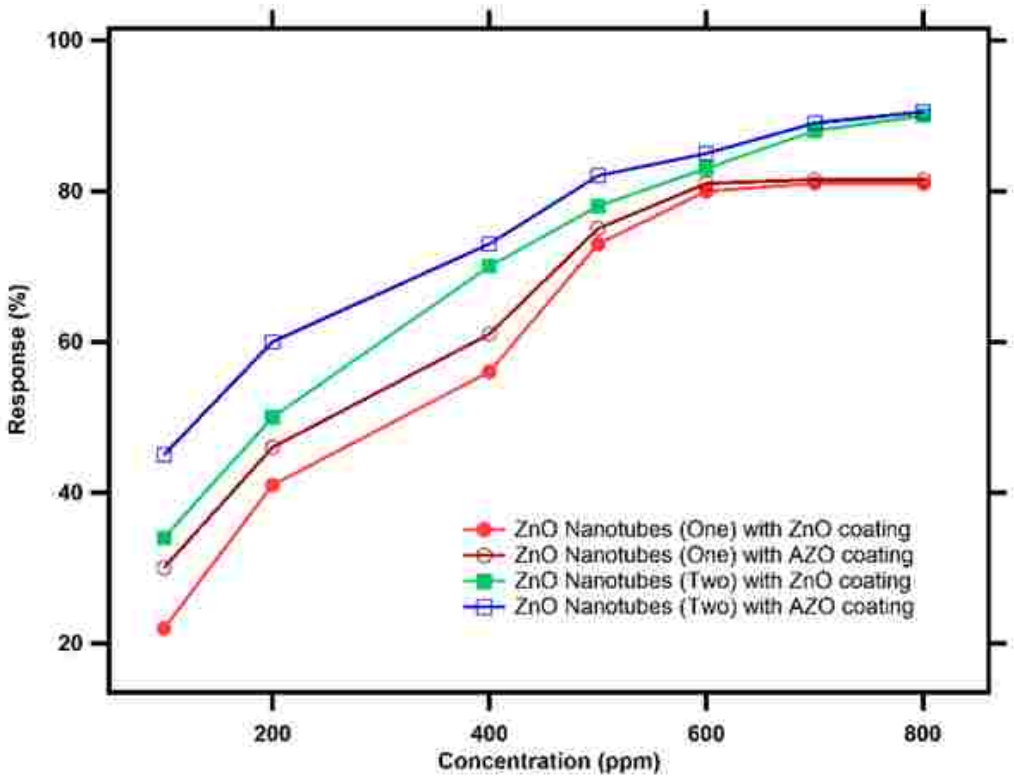


Figure 59. Sensing response of multiple nested ZnO gas sensors with one cycle and two cycles coated with ALD ZnO and with or without AZO thin films to ethanol vapor with different concentrations at 320℃

TABLE IX

Roughly counted density of ZnO nanorods grown by hydrothermal method, ZnO nanorod/nanotubes, and ZnO nanotubes synthesized in porous Si template.

| | ZnO nanorods (by hydrothermal growth) | ZnO nanorod/nanotubes (by hydrothermal growth) | ZnO nanotubes (by template replication) |
|---|---|---|---|
| Density ($number/cm^2$) | $\sim 1.4 \times 10^{10}$ | $\sim 1 \times 10^{10}$ | $\sim 1.25 \times 10^{7}$ (one layer)<br>$\sim 2.5 \times 10^{7}$ (two layers) |
| Height ($\mu m$) | ~0.6 | ~0.75 | 135 |

**5.3 Summary**

In this chapter, a different process fabrication approach was pursued for the synthesis of multiple nested tube-in-tube ZnO nanotube gas sensors inside the multitude of millions of pores in porous templates by combining Atomic Layer Deposition technology, Precision Ion Polishing System, and preferentially wet-etch treatments. The porous templates used in the synthesis of ZnO nanotube gas sensors includes porous Anodic Aluminum Oxide and porous Silicon. However, due to the very limited pore diameter of AAO porous templates, the sensing performance was analyzed only on ZnO nanotube gas sensors synthesized inside porous Si templates. to ethanol vapor concentration detection was investigated by the home-built gas sensor testing system. The objective of Chapter 5 was to combine the learning and best practices of Objective 1 (AZO coatings providing extra oxygen vacancies and additional electrons) and Objective 2 (nested coaxial ZnO nanotubes with two additional reaction surfaces providing additional reactive sensor surfaces). To eliminate unnecessary variance in device film thickness in and to enable meaningful data mining comparisons the necessary conductive ALD ZnO layer was deposited with the exactly the same thickness as the ALD AZO coating on the surface of ZnO nanotube gas sensors. The multiple nested ZnO nanotube gas sensors used in Chapter 5 for the sensing response investigations to ethanol vapor concentration detection include one layer with ZnO thin films, one layer with AZO coatings, two layers of coaxial ZnO nanotubes with ZnO thin films, and two layers of coaxial ZnO nanotubes with AZO coatings. Based on the sensing response comparison from the graphs of Fig. 51 & 54, the sensing response of multiple nested tube-in-tube ZnO nanotube gas sensors were improved by the introduction of one additional layer of coaxial ZnO nanotube which provided two additional sensor reaction surfaces per introduced sacrificial layer. With combining the learning of the two previous chapters, the sensing response of ZnO nanotube gas sensors has been

significantly enhanced with maximum gained enhancement reaching 136%. Furthermore, the measured increased saturation level provides an experimental corroboration of the hypothesis that increasing the surface-to-volume ratio of solid-state gas sensors provides a direct tangible improvement in gas sensor response. In conclusion, the observed trends of continuous improvements in sensor response in our plotted data provide a strong validation of the novel sensor device architecture and the advanced processing technology conceived during the work on this dissertation. Basically, the concept of using dummy sacrificial layers in nested nanolaminate gas sensor designs provides 2 new available reactive sensing surfaces after removal of the sacrificial layer. This concept can be readily extended to n sacrificial layers with each providing 2 new reactive surfaces. These experimentally validated design concepts and fabrication processes provide a pathway for further improvements in solid-state gas sensor response in the future and can be readily extended to other metal oxide sensor materials.

# CHAPTER 6

# CONCLUSIONS AND OUTLOOKS

## 6.1 Conclusions

In summary, semiconducting metal-oxide materials have attracted much attention for gas sensor applications in different areas due to their low cost, short response time and recovery time, wide detection range, and high tolerance for tough-working environments. ZnO gas sensors have been widely used in various gas detection applications for the indication of gas species and gas concentration due to the attractive materials characteristics of ZnO of good electrical conductivity, wide band gap (3.37eV), ~60 meV exciton binding energy, high mechanical stability, and low cost. Compared to other semiconducting metal oxide materials, the competitive advantages of ZnO in gas sensor applications include its high electrochemical stability, non-toxicity, low cost, and ease of doping. The application of ZnO material for ethanol vapor concentration detection is especially advantageous, because ZnO presents a good sensing performance to ethanol with high sensing response, short response time, and fast recovery time. Motivated by the shortcomings of present state-of-the-art ZnO thin film gas sensors, which are handicapped by insufficient sensitivity, long response time, and long recovery time to the ethanol vapor concentration detection with only one reaction surface, the objective of this dissertation was to improve the sensing performance of ZnO nanostructured gas sensors by introducing Aluminum doped ZnO (AZO) ALD coatings and by increasing the surface-to-volume ratio with a novel innovative sensor device architecture.

In Chapter 2, the experimental techniques used in this dissertation were introduced, which include the crystal growth technology used for the synthesis of ZnO nanorod/ nested nanotube gas

sensors and the subsequent analysis techniques for the evaluation of the sensing performance. The novel sensor device architecture conceived for this dissertation requires precisely controlled film deposition thickness and composition on a nanometer scale, which can only be realized by modern Atomic Layer Deposition (ALD) technology. The Hydrothermal growth method was applied for ZnO nanorod growth in this research due to its reasonable cost. In Objectives 2 and 3, Precision Ion Polish System (PIPS) milling was applied to remove the top cover caused by ALD thin films deposition and to expose the $Al_2O_3$ sacrificial layer with accurately controlled milling thickness on a nanometer scale. The purpose of this dissertation was to address the shortcomings of the present day ZnO gas sensors by providing innovative solutions with novel sensor device designs and new process technologies and to prove the superior sensing performance of the novel multiple nested coaxial ZnO nanotube gas sensors. As part of this dissertation work several versions of home-built gas sensor testing systems were custom designed and built for the investigation of the sensing performance improvement of ZnO nanotube gas sensors to the detection of ethanol vapor concentrations. A newly upgraded $2^{nd}$ generation gas sensor testing system was redesigned with introducing two Mass Flow Controllers (MFCs) to precisely control the concentration of the injected ethanol vapor.

Chapter 3 describes the deposition of ALD AZO coatings on the surface of hydrothermal ZnO nanorods to improve the sensing performance of ZnO nanorod gas sensors for the detection of ethanol vapor concentration. The Hydrothermal growth method was introduced to grow ZnO nanorods on fine grained ZnO seed layers deposited on Silicon substrates by ALD. A novel approach of ALD 3-D wrap-around nanolaminate coatings for delta doped AZO films was employed to enhance the sensing performance of ZnO nanorod gas sensors. The sensing response, response time, and recovery time of ZnO nanorod gas sensors without and with ALD AZO coatings

were investigated by the home-built 1st generation gas sensor testing system. The sensing response of ZnO nanorod gas sensors as a function of temperature was analyzed to determine the optimum working temperature at 320℃. From the results of the sensing response to ethanol vapor concentration as a function of temperature, the saturation concentration levels of ZnO nanorod gas sensors without and with ALD AZO thin film coating were realized at 800 ppm and 1000 ppm, respectively. As a tangible improvement the response time and recovery time of ZnO nanorod gas sensors for ethanol vapor concentration detection were shortened by introducing the ALD AZO coatings. The maximum enhancement gain was realized for approximately 100% at 37℃. The improved sensing performance is attributed to the extra oxygen vacancies and additional electrons generated by ALD AZO coatings.

Chapter 4 describes the fabrication of coaxial nested ZnO nanorod/nanotube gas sensors with a novel device design concept by an integrated process combining hydrothermal growth method with ALD technology. In this approach an amorphous $Al_2O_3$ sacrificial layer was introduced into the formation of coaxial ZnO nanotubes. Precision Ion Polishing System (PIPS) milling was employed to remove the top cover generated during ALD deposition process. After removing the ALD layer covers from the top of the ZnO nanorods with 3-D wrap-around coatings, the $Al_2O_3$ sacrificial layer was exposed for wet-etch removal by sodium hydroxide (NaOH). The NaOH solution with a pH value at 11 was chosen to preferentially remove the sacrificial layer according to the intrinsic solubility range of $Al_2O_3$ and ZnO. Following that final process stop the novel nested ZnO nanorod/nanotube architecture was formed. The sensing performance of innovative nested ZnO nanorod/nanotube gas sensors for ethanol vapor was investigated by the newly upgraded gas sensor testing system with two MFCs to precisely control the concentration of input ethanol vapor. The sensing response of the novel nested ZnO nanorod/nanotube gas

sensors increased with rising temperature until the maximum value was reached at 320℃. Beyond the peak at 320℃ the sensor response decreased at higher temperatures. Based on the sensing response comparison between conventional ZnO nanorod gas sensors and the novel innovative nested ZnO nanorod/nanotube gas sensors, the sensing response was significantly enhanced with a maximum value of 150% at 25℃. The saturation concentration level was also improved from 800 ppm to over 1000 ppm after synthesizing the coaxial nanotubes.

In Chapter 5, multiple nested tube-in-tube ZnO nanotube gas sensors were synthesized inside millions of pores in porous templates by ALD technology. Porous Anodic Aluminum Oxide (AAO) and porous Silicon were selected as the substrates for the fabrication of ZnO nanotube gas sensors. However, due to the limited diameter of AAO pores, only two layers of ZnO nanotubes with 20 nm thickness could be synthesized inside of individual pores of a porous AAO template. For this reason, all further nested nanotube work transitioned to porous Si templates with a pore diameter of 2 μm. All investigations of the sensing performance of ZnO nanotube gas sensor of ethanol vapors were performed on the ZnO nanotubes synthesized within the 2 μm diameter individual pores of porous Si templates. The objective of this innovative sensor device concept was to combine the proven enhancement features of Objective 1 (add extra oxygen vacancies and electrons with AZO coatings) and Objective 2 (achieving additional reaction surfaces). ZnO thin films with the same thickness of AZO coatings were deposited on the surface of ZnO nanotubes by ALD to retain standardized film thicknesses for this research study and to create a required conductive layer. The sensing response results exhibited a clear trend: the sensing response of the novel multiple nested ZnO nanotube gas sensors was significantly improved with the combined benefits from the two previous objectives. These very positive results prove the superior performance of our innovative novel sensor device design and validate success of these device

concepts. The increased saturation level was attributed to the two additional reaction surfaces provided by the coaxial ZnO nanotubes once the sacrificial layer was removed.

Objectives 1 and 2 established a bottom-up technology which is subject to high variability from batch to batch by hydrothermal growth of ZnO nanorods. However, Objective 3, utilizing template replication with porous Si templates, enables a true top-down technology by using mask and photolithography techniques from microelectronics to guarantee the reproducibility of pore density and geometrical pore shape, which would render it ready for commercialization and to be transferred for industrial applications.

### 6.2 Future Outlook

The standard investigations of the sensing performance of ZnO nanostructure gas sensors for the detection of ethanol vapor concentrations are based on the resistance change of the active ZnO material. However, as introduced in Section 1.2.1, various other physical changes occur in gas sensors during gas detection procedure, which can be utilized for sensing purposes. As a future outlook a brief review is provided for the case of using capacitance measurements for gas sensing purposes. The capacitance change of a gas sensor device is another physical parameter, which can be used to evaluate the sensing performance of ZnO gas sensors for the detection of ethanol vapor concentrations. Recently capacitance measurements have been employed for ZnO nanostructure gas sensor detection applications. In the context of future outlook, the potential benefits and the pros and cons of using capacitance measurements for MOS gas sensors are briefly discussed.

There are a number of Advantages for measuring capacitance changes for gas concentration detection:

1) High sensitivity (ppb)

2) Capable to operate at room temperature

3) Short response time and recovery time

Among the Disadvantages are:

1) Expensive with novel nanostructure synthesis procedure and method

2) Complicated device support circuit

The first two features in the list of advantages provide the motivation to synthesize ZnO nanostructure gas sensors and utilize capacitance change for sensing. Conventional MOS gas sensors are based on thin films, nanoparticles, nanorods, nanopores, nanowires, and microcantilevers, where the detection sensitivity levels are commonly parts per million (ppm) [56, 57, 58]. As demonstrated in the previous chapters of this dissertation, the sensing response of ZnO nanorod gas sensors has been successfully improved by implementing ALD AZO coatings and by increased surface-to-volume ratio using various process technologies. However, the sensitivity of these synthesized ZnO nested nanostructure gas sensors is still in the parts per million (ppm) range. To tap into new potential markets for more sensitive applications, the sensitivity needs to be dropped down into the parts per billion (ppb) range.

Another motivation is to enable the target gas detection with ZnO nanostructure gas sensors to be operated at room temperature. In most cases, a higher operating temperature (usually above 150℃) is required for the optimum gas detection by solid-state MOS gas sensors [59]. The optimum working temperature of MOS gas sensors is based on Equations 5 to 8 and determined by the strength of the Van Der Waals bond between the semiconducting metal oxide sensing material, oxygen molecules, and the target gas molecules [60]. Furthermore, MOS gas sensors based on nanostructure (like nanorods, nanowires) possesses small size and shape feature on the nanometer scale, which leads to a large surface-to-volume ratio [61]. However, at higher optimum

working temperature coalescence and structural changes occur in the sensor material, which are attributed to thermally induced grain growth [62]. These changes may cause a decrease in the sensitivity, lifetime, and stability of MOS gas sensors [63]. Furthermore, operating gas sensor detection at room temperature eliminates the consumption of the power for the sensor heater, protect the nanostructure of the active gas sensing material, and decrease the danger ratio with detecting flammable gases [63].

Figure 60 shows the schematic diagram of a coaxial capacitive detector for gas detection with parts per billion (ppb) level detection sensitivity and optimum working temperature finalized to room temperature. An array of vertically aligned carbon nanotubes (CNT) were grown by plasma-enhanced chemical vapor deposition with average height of 2 µm and density of ~$10^8$ units/$cm^2$ on polystyrene sphere-patterned substrates [64, 65, 66, 67]. One layer of alumina coatings, consisting of an amorphous nonporous atomic layer (a-$Al_2O_3$), with 10 nm thickness was deposited by ALD technology on the surface of CNT to form Electrode 1. Subsequently, a porous atomic layer (p-$Al_2O_3$) was deposited on the surface with a thickness of ~90 nm by reactive sputtering [64]. During Al sputter deposition, $O_2$ was introduced to gather with argon with a 1:4 ratio [64]. Finally, around 250 nm Al layer was deposited on the surface of the p-$Al_2O_3$ layer by sputtering to form Electrode 2. To support and stabilize the synthesized coaxial CNT and Al electrode, SU8-2002 photoresist polymer was employed by spin-coating followed by soft baking, UV light exposure, and hard baking [64]. After polishing the top cover, the coaxial capacitive detector was completed ready for exposure of the p-$Al_2O_3$ layer for target gas detection [64]. As shown in Figure 60, Electrode 1 (CNT, titanium film, a-$Al_2O_3$ coatings) and Electrode 2 (Al layer) are forming an equivalent circuit with a resistor and a capacitor connected in parallel [64]. After introducing the target gas, the exposed p-$Al_2O_3$ captures the target gas molecules based on

chemophysical adsorption, which causes a change in the sensor impedance [64]. The right two FE-SEM images in Figure 60 show a top view and a cross-sectional view of a single CNT with multiple coaxial alumina coatings.

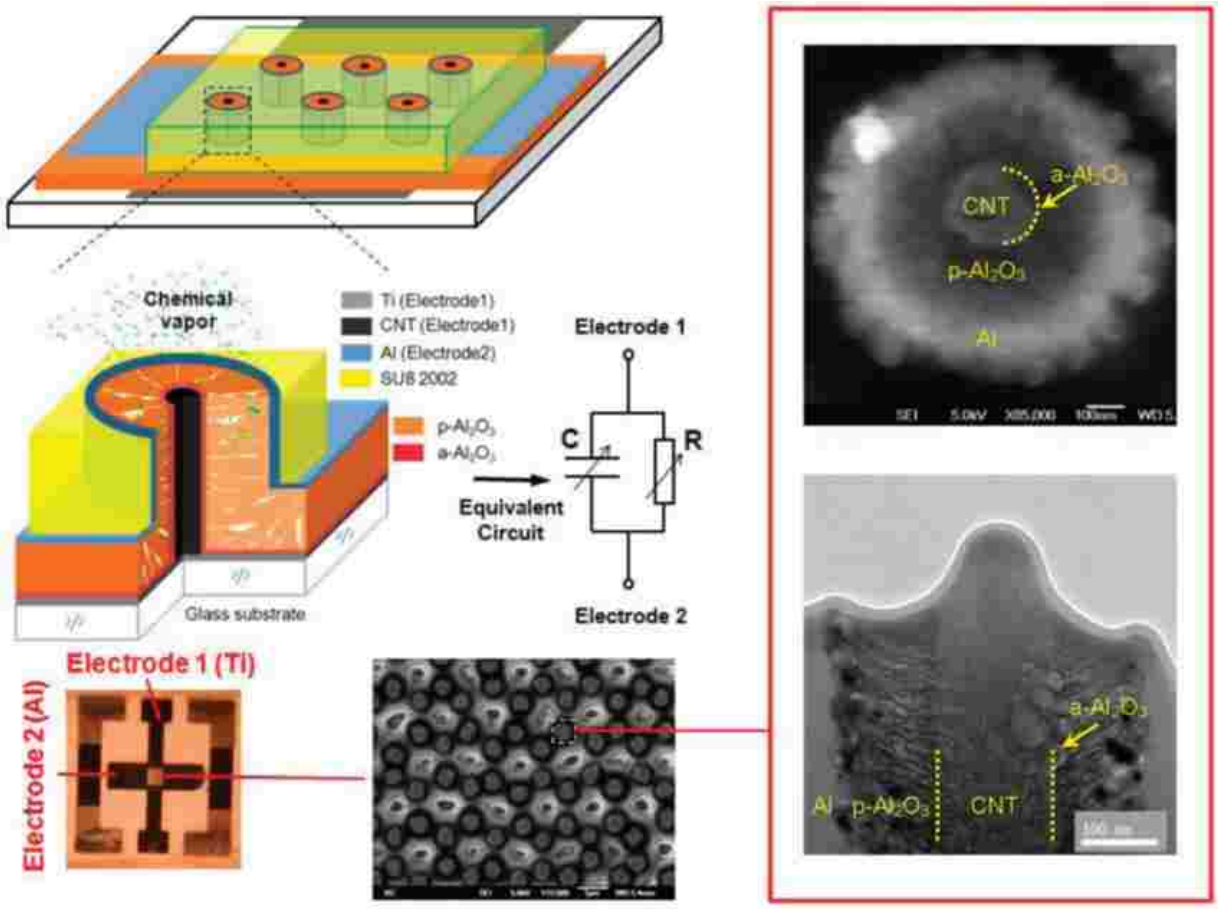


Figure 60. Nano-coaxial array-based chemical detection platform. The schematic diagram of the nano-coaxial capacitive detector and the equivalent circuit are shown on the left part. The structure consists of carbon nanotubes (CNT), nonporous atomic layer (a-$Al_2O_3$), porous atomic layer (p-$Al_2O_3$), Aluminum coating, and SU8 2002 polymer. The right two FE-SEM images show the top view and cross-sectional view of a single CNT with multiple coaxial Alumina coatings [64].

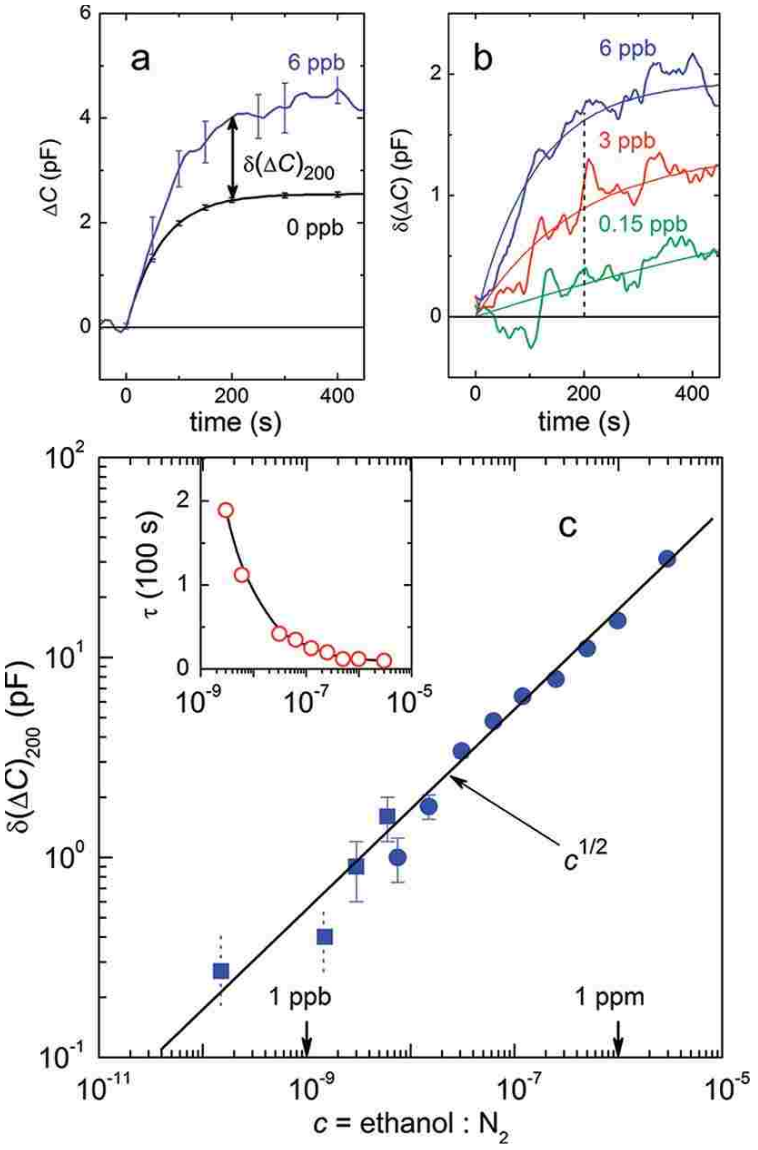


Figure 61. Nano-coaxial sensor array as high-performance ethanol sensor. a) capacitance changes of the nano-coaxial capacitive sensor after exposure to reference $N_2$ gas and $N_2$ gas with 6 ppb ethanol vapor, b) capacitance change after subtraction of the $N_2$ response ($\delta(\Delta C)$) to ethanol vapor with a concentration of 0.15 ppb, 3 ppb, and 6 ppb. c) summary of the sensing response $\delta(\Delta C)_{200}$ (capacitance difference at T=200 s) of coaxial capacitive gas sensors to ethanol vapor with different concentrations [64].

Figure 61 a) and b) show the sensing performance of nanocoaxial capacitive gas sensors as a function of time for the detection of ethanol vapor concentration in ppb range. Figure 61 a) shows the capacitance changes of the nanocoaxial gas sensors after exposure to $N_2$ gas with 0 ppb ethanol vapor (as reference) and $N_2$ gas with 6 ppb ethanol vapor. The capacitance difference ($\delta(\Delta C)_{200}$ ) between the two capacitance results, selected at response time of T=200 s, is determined as the sensing response of the nanocoaxial capacitive gas sensors to ethanol vapor with a concentration of 6 ppb [64]. Figure 61 b) shows the capacitance change after subtraction of the $N_2$ response ($\delta(\Delta C)$) of the nanocoaxial gas sensors to ethanol vapor with a concentration of 0.15 ppb, 3 ppb, and 6 ppb. Figure 61 c) shows the summary of the sensing response $\delta(\Delta C)_{200}$ (capacitance difference at T=200 s) of coaxial capacitive gas sensors to ethanol vapor with different concentrations (averages and standard deviations from the three responses in Figure 61 b)) [64].

### 6.3 Future work

*ZnO Nanorod on Porous Si*

To provide future research direction a new sensor design concept is suggested for further improvement of the sensing performance of ZnO gas sensors to ethanol vapor. A novel nanostructure is proposed by growing hydrothermal ZnO nanorods on ALD ZnO seed layers deposited on the pore walls of porous Si templates. The motivation of this innovative ZnO gas sensor concept is to harvest a much higher density of ZnO nanorods in the same area with the help of porous Si templates compared to the amount of ZnO nanorods that can be obtained with seed layers on a planar Si substrate. Figure 62 shows a schematic cross-sectional view of synthesis process sequence for growing hydrothermal ZnO nanorods inside the pores of porous Si templates. Atomic Layer Deposition technology is employed to deposit ZnO seed layers on porous Si

templates as shown in Figure 62(b) and (d). Then the hydrothermal growth method will be applied to synthesize ZnO nanorods from the seed layer inside the multitude of pores of porous Si templates, as shown in Figure 62 (c) and (e).

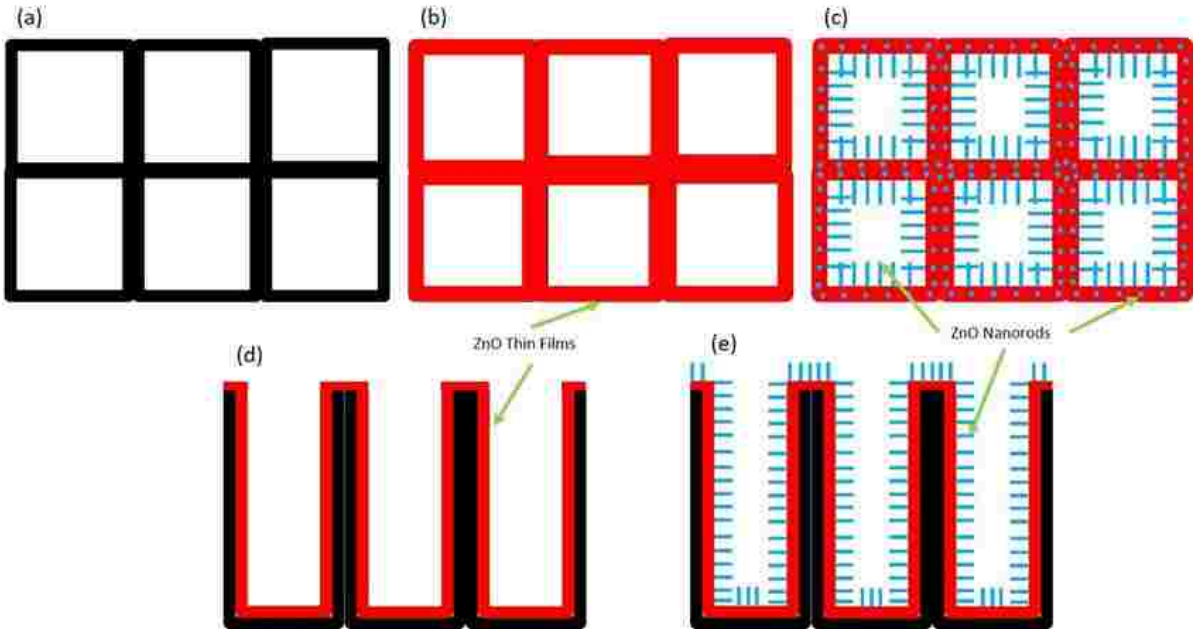


Figure 62. Schematic graphic presentation of ZnO nanorod on porous Si synthesis procedure. Top down view (a) porous Si, (b) ZnO seed layer deposited on porous Si by ALD, (c) ZnO nanorods grown on porous Si by hydrothermal method, cross-sectional view (d) and (e) cross-section of (b) and (c)

*ZnO Nanorod-on-Nanotube Gas Sensors*

In the quest to continuously improve the sensor surface-to-volume ratio a further refinement of the above sensor design concept is suggested in the following section. The proposed modified nanostructure is obtained by growing hydrothermal ZnO nanorods on the seed covered

surface of a center ZnO nanotube, that has been synthesized inside each pore of the porous Si template to form ZnO nanorod-on-nanotube structure.

The schematic process sequence for this modified innovative sensor design concept is explained in Figure 63 (top view) and Figure 64 (cross-section). This device concept starts with a first process step of depositing ZnO thin films on porous silicon templates by Atomic Layer Deposition with diethylzinc ($(C_2H_5)_2Zn$) and DI water as precursors, as shown in Figure 63 (b) and Figure 64 (a) (cross-section). Afterwards the amorphous $Al_2O_3$ sacrificial layer is deposited on the surface of ZnO thin films by ALD, as shown in Figure 63 (c) and Figure 64 (b) (cross-section). One additional ZnO thin films was deposited by ALD to form ZnO nanotube by sandwiching the sacrificial alumina layer in between the ZnO layers, as shown in Figure 63 (d) and Figure 64 (c) (cross-section). Before synthesizing ZnO nanorods by hydrothermal method, Precision Ion Polishing System (PIPS) milling is required to remove the top cover ALD layers to expose the $Al_2O_3$ sacrificial layer. Then the hydrothermal method is adopted for the grow of a high density of ZnO nanorods on the sidewalls of the ZnO nanotubes, as shown in Figure 63 (e) and Figure 64 (d) (cross-section). In the last process step, the $Al_2O_3$ sacrificial layer will be preferentially etched away by an alkali sodium hydroxide (NaOH) solution with controlled time, as indicated in Figure 63 (f) and Figure 64 (e) (cross-section). The schematic cross-section of Figure 64 (e) points out that the sacrificial $Al_2O_3$ layer has to remain at the bottom of the center nanotube to firmly anchor it on the bottom inside of each pore to prevent delamination and falling out of the ZnO nanotubes.

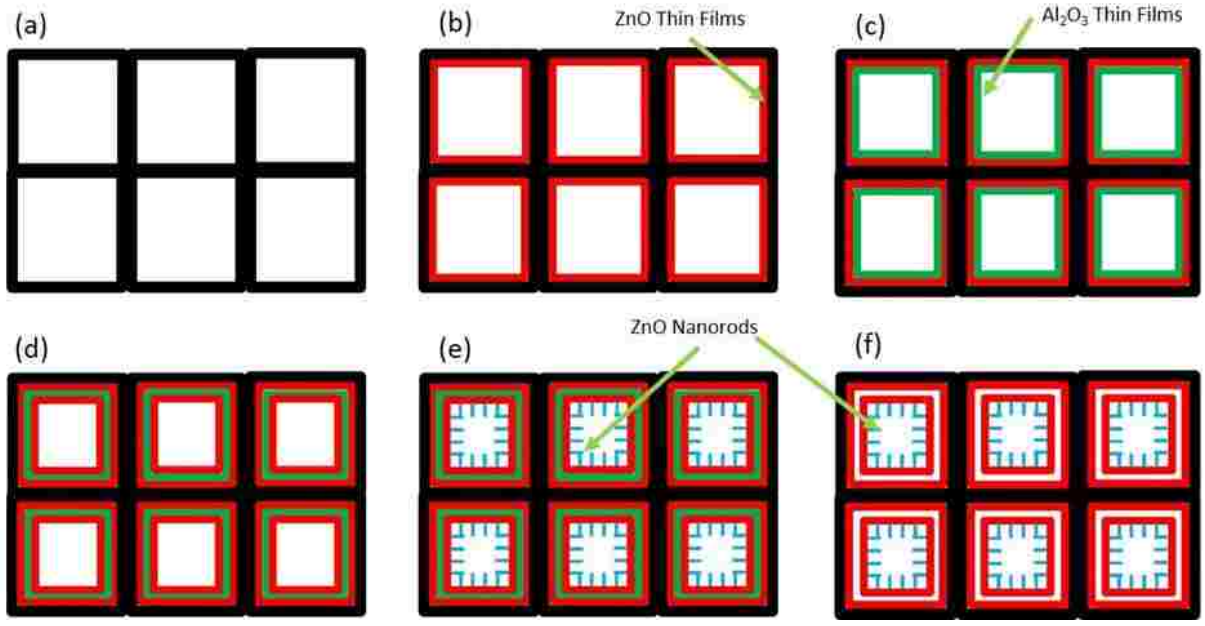


Figure 63. Schematic depiction of ZnO nanotubes synthesis procedure (Top View). (a) Porous Si, (b) ZnO seed layer deposited on porous Si, (c) $Al_2O_3$ sacrificial layer synthesized on the top of ZnO thin films, (d) additional ZnO thin films deposited by ALD, (e) ZnO nanorods synthesized on ZnO nanotube by hydrothermal method, (f) $Al_2O_3$ sacrificial layer preferentially etched away by NaOH.

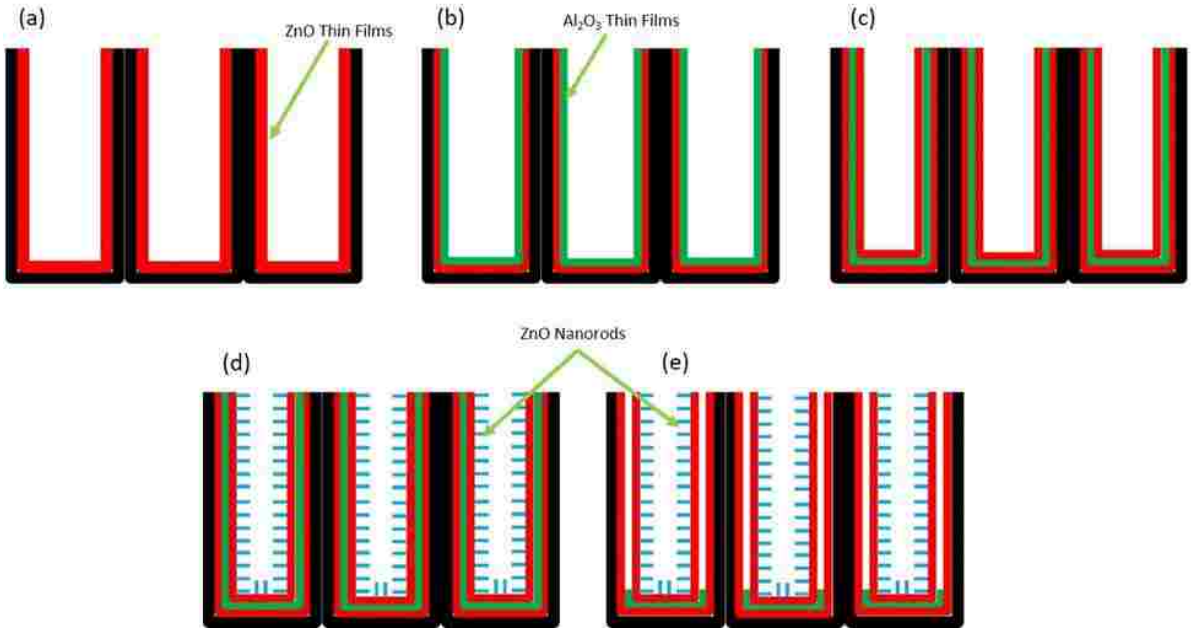


Figure 64. Schematic depiction of ZnO nanotubes synthesis procedure (Cross-Section). (a) ZnO seed layer deposited on porous Si, (b) $Al_2O_3$ sacrificial layer synthesized on the top of ZnO thin films, (c) additional ZnO thin films deposited by ALD, (d) ZnO nanorods synthesized on ZnO nanotube by hydrothermal method, (e) $Al_2O_3$ sacrificial layer preferentially etched away by NaOH.

**REFERENCES**

[1] A. Hayes, "Temperature Sensors: Make the Right Choice, RTD vs. TC", *Control Engineering*, **60**, ppP1-P3 (2013).

[2] B. Kleven, "A Summary of Gas Detection", Advanced Calibration Designs, Inc.

[3] S. Capone, A. Forleo, L. Francioso, R. Rella, P. Siciliano, J. Spadavecchia, D. S. Presicce, A. M. Taurino, "Solid State Gas Sensors: State of the Art and Future Activities", *Journal of Optoelectronics and Advanced Materials*, **5**, 5, p.1335-1348 (2003).

[4] X. Liu, S. Cheng, H. Liu, S. Hu, D. Zhang, H. Ning, "A Survey on Gas Sensing Technology", *Sensors 2012*, **12**, 9635-9665 (2012).

[5] V. Milosavljevic, "Electronic Gas Sensors and Detectors-Classification and Operating Principles", Electronic-Base (2012).

[6] R. L. Grob, "Modern Practice of Gas Chromatography", *John Wiley & Sons*, C1977, p. 228.

[7] R. Toniolo, N. Dossi, A. Pizzariello, A. Casagrande, G. Bontempelli, "Electrochemical Gas Sensors Based on Paper-supported Room-temperature Ionic Liquids for Improved Analysis of Acid Vapours", *Analytical & Bioanalytical Chemistry*, **405**, 11, p. 3571-3577 (2013).

[8] J. Chou, "Hazardous Gas Monitors-A Practical Guide to Selection, Operation and Applications", *Chapter 2 Electrochemical Sensors*, p.27-35 (1999).

[9] V. A. Smyntyna, "Semiconductor Materials for Gas Sensors", Hauppauge, New York: Nova Science Publishers, Inc. 2013.

[10] G. Neri, "First Fifty Years of Chemoresistive Gas Sensors", *Chemosensors*, **3**, 1-20, ISSN 2227-9040 (2015).

[11] P. Grundler, "Chemical Sensor: An Introduction for Scientists and Engineers", Springer, Berlin (2007).

[12] V. E. Bochenkov, G. B. Sergeev, "Sensitivity, Selectivity, and Stability of Gas-Sensitive Metal-Oxide Nanostructures", *Metal Oxide Nanostructures and Their Applications*, **3**, p. 31-52 (2010).

[13] J. Chou, "Hazardous Gas Monitors-A Practical Guide to Selection, Operation and Applications", Chapter 1 Introduction, p.1-24 (1999).

[14] C. Supab, H. Niyom, W. Ekasiddh, "Metal-Oxide Nanowires for Gas Sensor", *Nanowires-Recent Advances*, Chapter 1 (2012).

[15] L. W. Wang, Y. F. Kang, "ZnO Nanorods Gas Sensor for Ethanol Detection", *Sensors and Actuator B: Chemical*, 162: 237-243 (2012).

[16] C. Wang, L. Yin, L. Zhang, D. Xiang, R. Gao, "Metal Oxide Gas Sensor: Sensitivity and Influencing Factors", *Sensor 2010*, **10**, 2088-2106 (2010).

[17] B. Yuliarto, G. Gumilar, N. L. W. Septiani, "SnO2 Nanostructure as Pollutant Gas Sensors: Synthesis, Sensing Performances, and Mechanism", *Advances in Materials Science and Engineering*, Vol. **2015**, ID. 694823 (2015).

[18] S. M. Sze, M. K. Lee, "Semiconductor Devices: Physics and Technology", Chapter 3 p-n Junction, p. 85 (2012).

[19] D. Puzzovio, "Surface Interaction Mechanisms in Metal Oxide Semiconductors for Alkane Detection", Univerisita Degli Studi Di Ferrara (2008).

[20] F. F. George, M. C. Leon, A. Ayo, B. Russell, "Metal Oxide Semiconductor Gas Sensors in Environmental Monitoring", *Sensors 2010*, **10**, 5469-5502 (2010).

[21] D. Gu, H. Baumgart, T. M. Abdel-Fattah, G. Namkoong, "Synthesis of Nested Coaxial Multiple-Walled Nanotubes by Atomic Layer Deposition", *ACS Nano*, **4**, 2, 753-758 (2010).

[22] H. Kim, Y. Pak, Y. Jeong, W. Kim, J. Kim, and G. Y. Jung, "Amorphous Pd-assisted $H_2$ Detection of ZnO Nanorod Gas Sensor with Enhanced Sensitivity and Stability", *Sensors and Actuators B*, **262**, 460 (2018).

[23] N. Kakati, S. H. Jee, S. H. Kim, H. K. Lee, and Y. S. Yoon, "Sensitivity Enhancement of ZnO Nanorod Gas Sensors with Surface Modification by an InSb Thin Film", *Japanese Journal of Applied Physics*, **48**, 105002 (2009).

[24] M. Xu, Q. Li, Y. Ma, and H. Fan, "Ni-doped ZnO Nanorods Gas Sensor: Enhanced Gas-sensing Properties, AC and DC Electrical Behaviors", *Sensors and Actuators B*, **199**, 403 (2014).

[25] P. Nunes, D. Costa,E. Fortunato, R. Martins, "Performances presented by Zinc Oxide Thin Films Deposited by R. F. Magnetron Sputtering", *Vacuum*, **64**, 293-297 (2002).

[26] W. S. Choi, E. J. Kim, S. G. Seong, Y. S. Kim, C. Park, S. H. Hahan, "Optical and Structural Properties of ZnO/$TiO_2$/ ZnO Multi-layers Prepared via Electron Beam Evaporation", *Vacuum*, **83**, 878-882 (2009).

[27] A. R. Nimbalkar, M. G. Patil, "Synthesis of ZnO Thin Film by sol-gel Spin Coating Technique for $H_2S$ Gas Sensing Application", *Physical B: Condensed Matter*, **527**, 7-15 (2017).

[28] M. Caglar, S. Ilican, Y. Caglar, F. Yakuphanoglu, "Electrical Conductivity and Optical Properties of ZnO Nanostructured Thin Film", *Applied Surface Science*, **255**, 4491-4496 (2009).

[29] S. S. Zahirullah, P. Immanuel, S. Pravinraj, P. F. H. Inbaraj, J. J. Prince, "Synthesis and Characterization of Bi Doped ZnO Thin Films using SILAR Method for Ethanol Eensor", *Materias Letters*, **230**, 1-4 (2018).

[30] E. Muchuweni, T. S. Sathiaraj, H. Nyakotyo, "Synthesis and Characterization of Zinc Oxide Thin Films for Optoelectronic Applications", *Heliyon*, 3, 4 (2017).

[31] E. Guziewicz, M. Godlewski, L. Wachnicki, T. A. Krajewski, G. Luka, S. Gieraltowska, R. Jakiela, A. Stonert, W. Lisowski, M. Krawczyk, "ALD Grown Zinc Oxide with Controllable Electrical Properties", *Semiconductor Science and Technology*, **27**, 7 (2012).

[32] S. M. George, "Atomic Layer Deposition: An Overview", *Chemical Reviews*, **110**(1): p. 111-131 (2010).

[33] D. Turakhia, "Atomic Layer Deposition-1, Growth Rate and Uniformity of $Al_2O_3$", *Tool Data*, Page 5 (2015).

[34] B. D. Yao, Y. F. Chan, N. Wang, "Formation of ZnO Nanostructures by a Simple Way of Thermal Evaporation", *Applied Physics Letters*, **81**, 757 (2007).

[35] H. Cao, J. Y. Wu, H. C. Ong, J. Y. Dai, R. P. H. Chang, "Second Harmonic Generation in Laser Ablated Zinc Oxide Thin Films", *Applied Physics Letters*, **73**, 572 (1998).

[36] P. Chang, Z. Fan, D. Wang, W. Tseng, W. Chiou, J. Hong, J. G. Lu, "ZnO Nanowires Synthesized by Vapor Trapping CVD Method", *Chemistry of Materials*, **16**, 5133 (2004).

[37] L. F. Dong, Z. L. Cui, Z. K. Zhang, "Gas Sensing Properties of Nano-ZnO Prepared by ARC Plasma Method", *Nanostructured Materials*, **8**, 815 (1997).

[38] Y. Tak, D. Park, K. J. Yong, "Characterization of ZnO Nanorod Arrays Fabricated on Si Wafers using a Low-temperature Synthesis Method", *Journal of Vacuum Science & Technology B*, **24**, 2047 (2006).

[39] D. V. Tawde, "Structural and Optical Studies of Cerium Doped Lead Tungstate Nano Phosphor", Maharaja Sayajirao University of Baroda, 2013.

[40] V. Gaddam, R. R. Kumar, M. Parmar, M. M. Nayak, K. Rajanna, "Synthesis of ZnO Nanorods on a Flexible Phynox Alloy Substrate: Influence of Growth Temperature on Their Properties", *RSC Advances*, **5**, 89985-89992 (2015).

[41] A. Aitkaliyava, J. W. Madden, B. D. Miller, J. I. Cole, J. Gan, "Comparison of Preparation Techniques for Nuclear Materials for Transmission Electron Microscopy", *Journal of Nuclear Materials*, **459**, 241-246 (2015).

[42] P. Lin, X. Chen, K. Zhang, H. Baumgart, "Improved Gas Sensing Performance of ALD AZO 3-D Coated ZnO Nanorods", *ECS Journal of Solid State Science and Technology*, **7** (12), Q246-252 (2018).

[43] NI cRIO-9068 User Manual, National Instruments, (2016).

[44] C. S. Prajapati and P. P. Sahay, "Alcohol-sensing Characteristics of Spray Deposited ZnO Nano-particle Thin Films", *Sensors and Actuators B: Chemical*, **160**, 1043 (2011)

[45] Using MiCS Sensors for Alcohol Detection, A1A-MICS_AN4 Version 1, e2v technologies (2009).

[46] P. Genevee, F. Donsanti, G. Renou, and D. Lincot, "Study of the Aluminum doping of Zinc Oxide Films Prepared by Atomic Layer Deposition", *Applied Surface Science*, **264**, 464 (2013).

[47] G. Luka, T. A. Krajewski, B. S. Witkowski, G. Wisz, I. S. Virt, E. Guziewicz, and M. Godlewski, "Aluminum-doped Zinc Oxide Films Grown by Atomic Layer Deposition for Transparent Electrode Applications", *Journal of Materials Science: Materials in Electronics*, **22**, 12, 1810 (2011).

[48] J. W. Elam, D. Routkevitch, and S. M. George, "Properties of $ZnO/Al_2O_3$ Alloy Films Grown Using Atomic Layer Deposition Techniques", *Journal of the Electrochemical Society*, **150**, issue 6, G339 (2003).

[49] L. M. Li, Z. F. Du, T. H. Wang, "Enhanced Sensing Properties of Defect-controlled ZnO Nanotetrapods Arising from Aluminum Doping", *Sensors and Actuators B: Chemical*, **147**, 165-169 (2010).

[50] N. U. Saidin, T. F. Choo, K. Y. Kok, "Hydrothermal growth of ZnO: a substrate-dependent study on nanostructures formation", *IOP Conference Series: Material Science and Engineering*, **298**, 012016 (2018)

[51] B. Santoshkumar, A. Biswas, S. Kalyanaraman, R. Thangavel, G. Udayabhanu, G. Annadurai, S. Velumani, "Influence of Defect Luminescence and Structural Modification on the Electrical Properties of Magnesium Doped Zinc Oxide Nanorods", *Superlattices and Microstructures*, **106**, 58-66 (2017).

[52] J. Deenathayalan, M. Saroja, M. Venkatachalam, P. Gowthaman, T. S. Senthil, S. Shankar, "Fabrication of Natural Dye Sensitized Solar Cell using Hydrothermally grown Zinc Oxide Nanorods", *International Journal of Nano Science and Nanotechnology*, **3**, No. 2, 81-89, (2012).

[53] J. Deenathayalan, M. Saroja, M. Venkatachalam, P. Gowthaman, "ZnO Nanorod based Dye Sensitized Solar Cells with Natural Dyes Extracted from Amaranthus Caudatus and Morus Alba", *Journal of Nano Science and Nano Technology*, **2**, issue 4, 384-389 (2014).

[54] A. Momot, M. N. Amini, G. Reekmans, D. Lamoen, B. Partoens, D. R. Slocombe, K. Elen, P. Adriaenses, A. Hardy, M. K. Van Bael, "A novel Explanation for the increased Conductivity in Annealed Al-doped ZnO: an Insight into Migration of Aluminum and Displacement of Zinc", *Physical Chemistry Chemical Physics*, **19**, 27866 (2017)

[55] R. Yoo, S. Cho, M. J. Song, W. Lee, "Highly Sensitive Gas Sensor Based on Al-doped ZnO Nanoparticles for Detection of Dimethyl Methylphosphonate as A Chemical Warfare Agent Simulant", *Sensors and Actuators B: Chemical*, **221**, 217-223 (2015).

[56] F.R. Fan, A. J. Bard, "Electrochemical Detection of Single Molecules", *Science*, **267**, 871–874 (1995).

[57] P. Chen, J. Gu, E. Brandin, Y. R. Kim, Q. Wang, D. Branton, "Probing Single DNA Molecule Transport Using Fabricated Nanopores", *Nano Letters*, **4**, 2293–2298 (2004).

[58] G. Shekhawat, S.-H. Tark, V. P. Dravid, "MOSFET-Embedded Microcantilevers for Measuring Deflection in Biomolecular Sensors", *Science*, 311, 1592–1595 (2006).

[59] J. Zhang, X. Liu, G. Neri, and N. Pinna, "Nanostructured Materials for Room-Temperature Gas Sensors", Advanced Materials, **28**, 795 (2016).

[60] D. R. Miller, S. A. Akbar, and P. A. Morris, "Nanoscale Metal Oxide-based Heterojunctions for Gas Sensing: A Review", *Sensors and Actuators, B: Chemical*, **204**, 250 (2014).

[61] A. Gurlo, "Nanosensors: Towards Morphological Control of Gas Sensing Activity. $SnO_2$, $In_2O_3$, ZnO and $WO_3$", *Nanoscale*, **3**, 154 (2011).

[62] E. Comini, "Metal Oxide Nano-crystals for Gas Sensing", Analytica Chimica Acta, **568**, 28 (2006).

[63] A. P. Sharma, P. Dhakal, D. K. Pradhan, M. K. Behera, B. Xiao, M. Bahoura, "Fabrication and characterization of SnO2 nanorods for room temperature gas sensors", *AIP Advances*, **8**, 095219 (2018).

[64] H. Zhao, B. Rizal, G. McMahaon, H. Wang, P. Dhakal, T. Kirkpatrick, Z. Ren, T. C. Chiles, M. J. Naughton, D. Cai, "Ultrasensitive Chemical Detection using A Nnaocoax Sensor", *ACS Nano*, **6**, 4, 3171-3178 (2012).

[65] Z. F. Ren, Z. P. Huang, J. W. Xu, J. H. Wang, P. Bush, M. P. Siegal, P. N. Provencio, "Synthesis of Large Arrays of Well-Aligned Carbon Nanotubes on Glass", *Science*, **282**, 1105–1107 (1998).

[66] P. Ivanov, E. Llobet, X. Vilanova, J. Brezmes, J. Hubalek, X. Correig, "Development of High Sensitivity Ethanol Gas Sensors Based on Pt-Doped $SnO_2$ Surfaces", *Sensors and Actuators, B*, **99**, 201–206 (2004).

[67] D. Cai, L. Ren, H. Zhao, C. Xu, L. Zhang, Y. Yu, H. Wang, Y. Lan, M. F. Roberts, J. Chuang, "A Molecular-Imprint Nanosensor for Ultrasensitive Detection of Proteins", *Nature Nanotechnology*, **5**, 597–601 (2010).

# VITA

Pengtao Lin
Department of Electrical and Computer Engineering
Old Dominion University (ODU)
Norfolk, Virginia 23529

## CONTACT

pxlin002@odu.edu

## EDUCATION

Ph.D. Electrical Engineering, Old Dominion University, December 2019
M.S. Electrical Engineering, Gannon University, December 2013
B.S. Automation, University of Jinan, July 2009

## AWARDS

First Prize, Mid-Atlantic Chapter, AVS Research Poster Winner (2017)
First Prize, Mid-Atlantic Chapter, AVS Research Poster Winner (2019)

## PUBLICATIONS

7. Invention Disclosure: P. Lin, K. Zhang, H. Baumgart, Novel Design Architecture for ZnO Gas Sensors & Method to Fabricate These Gas Sensors with Enhanced Sensing Performance utilizing Novel AZO Coating multiple Nested Nanorod/Nanotube Structures, 2019 (Submitted & in Processing)
6. P. Lin, K. Zhang, H. Baumgart, "Enhanced Sensing Performance of ZnO Nanorod Gas Sensors with Novel Coaxial Nanorod-in-Nanotube Structure", (Review).
5. P. Lin, X. Chen, K. Zhang, H. Baumgart, "Improved Gas Sensing Performance of ALD AZO 3-D Coated ZnO Nanorods", Journal of Solid-State Science Technology, 7, 12, 246-252 (2018).
4. X. Chen, P. Lin, K. Zhang, H. Baumgart, B. Geist, V. Kochergin, "Seebeck Coefficient Enhancement of ALD PbTe/PbSe Nanolaminate Structures Deposited inside Porous Silicon Templates Electronic Materials and Processing", ECS Journal Solid State Science Technology, 2016, 5(9): P503-P508.
3. X. Chen, Z. Wang, P. Lin, K. Zhang, H. Baumgart, "Thermoelectric Properties of Highly Ordered Metal-Organic Framework Films", ECS Transactions 75(13):119-126. September 2016.
2. K. Zhang, C. McCleese, P. Lin, X. Chen, "Synthesis of ALD Tungsten Trioxide Thin Films from $W(CO)_6$ and $H_2O$ Precursors", ECS Transactions, 2015, 69(7): 199-209.
1. Q. Zheng, P. Lin, F. Mak, R. Sundaram, L. Zhao, "Curriculum Integration for the ECE Undergraduate Core Courses in Electronics", ASEE/IEEE Frontiers in Education Conference, 2013, 1115-1117.

## CONFERENCE PRESENTATIONS

33. "Sensing Enhancement on ZnO Nanorod Gas Sensors with Novel Nanorod/Nanotube Structures", Pengtao Lin, Xin Chen, Kai Zhang, Helmut Baumgart; 14$^{th}$ Intl. Symposium

on Chemical Sensors: Chemical and Biological Sensors and Analytical Systems, 234th Electrochemical Society Meeting, Cancun, Mexico, Sept. 30 – October 4 (2018)

32. "Optical Properties of Transition Metal Dichalcogenide MoS2 thin Films Synthesized by Atomic Layer Deposition", Min Zeng, Pengtao Lin, C. McCleese, C. Kolodziej, Kai Zhang, Clemens Burda, Qiliang Li, and Helmut Baumgart; 11th Intl. Symposium on Low-Dimensional Nanoscale Electronic and Photonic Devices, 234th Meeting of The Electrochemical Society, Cancun, Mexico, Sept. 30 – October 4 (2018)
31. "Nano scaled 1-D Nanorod and Nested Nanotube Device Structures in Gas Sensing Applications", Helmut Baumgart, P. Lin, K. Zhang, 11th Intl. Symposium on Low-Dimensional Nanoscale Electronic and Photonic Devices, 234th Meeting of The Electrochemical Society, Cancun, Mexico, Sept. 30 – October 4 (2018)
30. "Thermoelectric Characterization of Copper Hexacyanoferrate", P. Hosseini, G. Wittstock, M. Kumari, Engelbert Redel, Pengtao Lin, Kai Zhang, and Helmut Baumgart; 1st Intl. Symposium on Electronic, Thermal, and Electrochemical Properties of Metal-Organic Frameworks (MOFs): Technology, Applications, and Emerging Devices, 234th Electrochemical Society Meeting, Cancun, Mexico, Sept. 30 – October 4 (2018)
29. "Physical Characterization of Transition Metal Dichalcogenide MoS2Thin Films Synthesized by Atomic Layer Deposition", H. Zhang, M. Zeng, P. Lin, C. McCleese, C. Kolodziej, K. Zhang, C. Burda, Q. Li, H. Baumgart; 18th Intl. Conference on Atomic Layer Deposition and Atomic Layer Etching ALD-2018, American Vacuum Society, Incheon, South Korea, July 29 – August 1, (2018)
28. "Novel ZnO Nanorod Ethanol Sensor using ALD Delta Doping with $Al_2O_3$ for Nested AZO Wrap-around Coatings", Pengtao Lin, Xin Chen, Kai Zhang, Helmut Baumgart; 18th Intl. Conference on Atomic Layer Deposition and Atomic Layer Etching ALD-2018, American Vacuum Society, Incheon, South Korea, July 29 – August 1, (2018)
27. "ZnO Nanorod Gas Sensors with Nested Nanorod/Nanotube Structure", Pengtao Lin, Xin Chen, Kai Zhang, Helmut Baumgart, American Vacuum Society, Mid-Atlantic Meeting, Newport News, Virginia, April 25 (2018)
26. "In-Plane ZT Measurements of PbTe/PbSe Superlattice Layers Deposited by Atomic Layer Deposition", Xin Chen, Vincent Linseis, Pengtao Lin, Kai Zhang, Helmut Baumgart, Heiko Reith, 3rd Intl. Symposium on Thermoelectric and Thermal Interface Materials, at the 232nd Meeting of The Electrochemical Society, National Harbor, Maryland, USA, October 1-6, (2017).
25. "Enhanced ZnO Nanorod Gas Sensors", Pengtao Lin, Xin Chen, Kai Zhang, Helmut Baumgart, Intl. Symposium on Sensors, Actuators and Microsystems, 232nd Meeting of The Electrochemical Society, National Harbor, Maryland, USA, October 1-6, (2017).
24. "Reduced Thermal Conductivity of Thermoelectric Layers Grown on Stripe-patterned Silicon Substrates", Xin Chen, Pengtao Lin, Kai Zhang, Helmut Baumgart, 2017 International Conference on Thermoelectrics (ICT), Pasadena, California, 31 July – August 3 (2017)
23. "Thermoelectric Properties Investigation of Polycrystalline and Highly Ordered Metal-Organic Framework Thin Films", Xin Chen, Zhengbang Wang, Zeinab Mohammed Hassan, Pengtao Lin, Kai Zhang, Helmut Baumgart, Engelbert Redel, 2017 International Conference on Thermoelectrics (ICT), Pasadena, California, 31 July - 3 August (2017)
22. Femtosecond Transient Absorption Dynamics of MoS2 Films Synthesized by Atomic Layer Deposition", K. Zhang, M. Zeng, C. McCleese, C. Kolodziej, X. Chen, P. Lin, C.

Burda, Q. Li, H. Baumgart, 1st International Semiconductor Conference for Global Challenges (ISCGC-2017), Nanjing, China, July 16-19 (2017)

21. "Enhancement of ZnO Nanorod Gas Sensors with AZO Nanolaminate Coating by Atomic Layer Deposition", Pentao Lin, Xin Chen, Kai Zhang, Helmut Baumgart, American Vacuum Society 17th Intl. Conference on Atomic Layer Deposition ALD 2017, Denver, Colorado, July 15-18 (2017)
20. "Reduced Thermal Conductivity of ALD Synthesized PbTe/PbSe Nanolaminates Grown on Nanopatterned Substrates", Xin Chen, Mallory E. DeCoster, Pengtao Lin, Kai Zhang, Patrick Hopkins, Helmut Baumgart, American Vacuum Society 17th Intl. Conference on Atomic Layer Deposition ALD 2017, Denver, Colorado, July 15-18 (2017)
19. "Atomic Layer Deposition of Transition Metal Dichalcogenide MoS2 Thin Films", Min Zeng, Kai Zhang, Xin Chen, Pengtao Lin, Qiliang Li, Christopher McCleese, Charles Kolodziej, Clemens Burda, Helmut Baumgart, American Vacuum Society 17th Intl. Conference on Atomic Layer Deposition ALD 2017, Denver, Colorado, July 15-18 (2017)
18. "Thermoelectric Anisotropy Properties of Metal-Organic Framework Films", Xin Chen, Pengtao Lin, Kai Zhang, Zeinab Mohammed Hassan, Zhengbang Wang, Helmut Baumgart, Engelbert Redel, the American Vacuum Society Mid-Atlantic Meeting, Newport News, VA, April 19, 2017
17. "Sensing Enhancement of ZnO Nanorods to Ethanol Vapor with AZO Nanolaminate Coating by ALD", Pengtao Lin, Xin Chen, Kai Zhang, and Helmut Baumgart, the American Vacuum Society Mid-Atlantic Meeting, Newport News, VA, April 19, 2017
16. "Synthesis of Transition Metal Dichalcogenide MoS2 thin Films by Atomic LayerDeposition, M. Zeng, K. Zhang, X. Chen, P. Lin, Q. Li, and H. Baumgart, 8th International Conference on Advanced Materials and Nanotechnology AMN8, The MacDiarmid Institute for Advanced Materials and Nanotechnology, Queenstown, NZ, February 12 – 17 (2017)
15. "Advances in Phonon Engineering of Nanoscaled Thermoelectric Materials with Improved Figure of Merit ZT", Xin Chen, Pengtao Lin, Kai Zhang, H. Baumgart, 8th International Conference on Advanced Materials and Nanotechnology AMN8, The MacDiarmid Institute for Advanced Materials and Nanotechnology, Queenstown, NZ, February 12 – 17 (2017)
14. "Thermoelectric Properties of Highly Ordered Metal-Organic Framework Films", Xin Chen, Zhengbang Wang, Pengtao Lin, Kai Zhang, Helmut Baumgart, Engelbert Redel, and Christof Wöll, 2nd International Symposium on Emerging Nanomaterials and Devices, 230th Meeting of the Electrochemical Society, Pacific Rim Meeting PRIME 2016, Honolulu, Hawaii, October 2-7 (2016)
13. "Thermoelectric Properties Enhancement by ALD Synthesis of Lead Chalcogenide on Stripe Patterned Si Substrates", Xin Chen, Pengtao Lin, Kai Zhang, Helmut Baumgart, 12th International Symposium on Atomic Layer Deposition Applications, 230th Meeting of the Electrochemical Society, Pacific Rim Meeting PRIME 2016, Honolulu, Hawaii, October 2-7 (2016)
12. "Nested ZnO Nanorod Gas Sensors Grown on ALD Seed Layers Synthesized on Si Substrates and Glass Fibers", Pengtao Lin, Xin Chen, Kai Zhang, Helmut Baumgart, 12th International Symposium on Atomic Layer Deposition Applications, 230th Meeting of the Electrochemical Society, Pacific Rim Meeting PRIME 2016, Honolulu, Hawaii, October 2-7 (2016)

11. “Thermoelectrical Properties of PbTe1-x Sex/PbSe Quantum Dot Superlattice Synthesized by Atomic Layer Deposition”, Xin Chen, Pengtao Lin, Kai Zhang, Helmut Baumgart, Vladimir Kochergin, American Vacuum Society ALD 2017 Conference, Dublin, Ireland, July 24-27 (2016)
10. “Atomic Layer Deposition of Iridium Oxide Thin Films”, Kai Zhang, Pengtao Lin, Xin Chen, Helmut Baumgart, James Bradas, American Vacuum Society ALD 2017 Conference, Dublin, Ireland, July 24-27 (2016)
9. “Interface Issues during ALD Coatings of Selective Laser Melted 3-D Printer Stainless Steel”, Kai Zhang, Pengtao Lin, Xin Chen, Helmut Baumgart, James Bradas, American Vacuum Society ALD 2017 Conference, Dublin, Ireland, July 24-27 (2016)
8. “Seebeck Coefficient Measurement of PbSeTe / PbTe Nanolaminate Structures”, Xin Chen, Pengtao Lin, Kai Zhang, Helmut Baumgart, Vladimir Kochergin, 2nd Intl. Symposium on Thermoelectric and Thermal Interface Materials, 228th Electrochemical Society Fall Conference, Phoenix, Arizona, October (2015)
7. “Synthesis of ALD Tungsten Trioxide Thin Films from W(CO)6 and H2O Precursors”, Kai Zhang, Pengtao Lin, Xin Chen, Felix Seo, Helmut Baumgart, 11th Intl. Symposium on Atomic Layer Deposition Applications, 228th Electrochemical Society Fall Conference, Phoenix, Arizona, October (2015)
6. “Synthesis of Transition Metal Dichalcogenide $WSe_2$ thin Films by Atomic Layer Deposition”, Kai Zhang, Xin Chen, Pengtao Lin, Quinton Rice, Mahmoud Abdel-Fattah, Felix Seo, Qiliang Li, Helmut Baumgart, 11th Intl. Symposium on Atomic Layer Deposition Applications, 228th Electrochemical Society Fall Conference, Phoenix, Arizona, October (2015)
5. “Raman Spectroscopy of Aluminum-Doped Zinc Oxide Thin Films Synthesized by Atomic Layer Deposition”, Pengtao Lin, Xin Chen, Kai Zhang, Helmut Baumgart, 11th Intl. Symposium on Atomic Layer Deposition Applications, 228th Electrochemical Society Fall Conference, Phoenix, Arizona, October (2015)
4. “Synthesis of Transition Metal Dichalcogenide WSe2Thin Films by Atomic Layer Deposition”, Kai Zhang, Xin Chen, Pengtao Lin, Quinton Rice, Mahmoud Abdel-Fattah, Felix J. Seo, Qiliang Li, Helmut Baumgart, American Vacuum Society ALD 2016 Conference, Portland, Oregon, June 28 – July 1, (2015)
3. “Atomic Layer Deposition of Tungsten Trioxide Thin Films using $W(CO)_6$ and $H_2O$”, Kai Zhang, Pengtao Lin, Xin Chen, Felix J. Seo, Helmut Baumgart, American Vacuum Society ALD 2016 Conference, Portland, Oregon, June 28 – July 1, (2015)
2. “ALD Deposition of PbTeSe Quantum Dot Superlattice for High ZT Thermoelectric Materials”, Xin Chen, Pengtao Lin, Kai Zhang, Helmut Baumgart, Vladimir Kochergin, American Vacuum Society ALD 2016 Conference, Portland, Oregon, June 28 – July 1, (2015)
1. “Raman Spectroscopy Analysis of Al doped ZnO Thin Films Grown by Atomic Layer Deposition”, Pengtao Lin, Xin Chen, Kai Zhang, Anderson Hayes, Felix Jaetae Seo, Helmut Baumgart, American Vacuum Society ALD 2016 Conference, Portland, Oregon, June 28 – July 1, (2015)